PREPARATION AND CHARACTERIZATION OF SILVER AND COPPER VANADATES

by

ABBAS VALI

DISSERTATION

Submitted in partial fulfillment of the requirements for the degree of Doctor of Philosophy at

The University of Texas at Arlington, Chemistry and Biochemistry Department

August, 2021

Arlington, TX

Supervising committee:

Dr. Krishnan Rajeshwar, Supervising Professor

Dr. Purnendu Dasgupta

Dr. Kevin Schug

Dr. Peter Kroll

To the memories of my late mother

ACKNOWLEDGEMENTS

During my Ph.D. career, I was lucky enough to have many individuals who supported and encouraged me to remain motivated. These individuals advised and assisted me to keep working hard towards achieving my goals, and I have greatly enjoyed their guidance and assistance during my Ph.D. journey. I would like to thank and acknowledge each and every individual who was there for me through these years of hard work and dedication.

First of all, I would like to thank my family, whom without their constant support, I would not be where I am today. Their support gave me the strength and motivation I needed in order to get through graduate school. I would like to thank my father and my late mother, my siblings, and my wife who have always seen my potential and supported me to achieve my goals to the best of my ability. I am so thankful for having all of them in my life.

I would like to express my deepest appreciation to my great mentor, Professor Krishnan Rajeshwar, for his unwaving support during my Ph.D. career. I also wish to thank my committee members Professor Purnendu Dasgupta, Professor Kevin Schug, and Professor Peter Kroll for their comments and advices. I would like to acknowledge the useful contributions of my research collaborators, Professor Muhammad N. Huda, Professor Robin T. Macaluso, Professor Noseung Myung, Professor Csaba Janaky, Professor Gerko Oskam, and their research groups. Finally, I would like to thank my groupmates, Dr. Farinaz Firouzan and Dr. Mohammad K. Hossain, and all colleagues whom extended a great amount of assistance during my Ph.D. career.

TABLE OF CONTENTS

LIST OF ILLUSTRATIONS

LIST OF TABLES

LIST OF ABBREVIATIONS

Å	Angstrom
AP-UPS	Ambient-pressure UV photoelectron spectroscopy
Calc	Calculated
CB	Conduction band
CBM	Conduction band minimum
CZTS	Copper zinc tin sulfide
CPD	Contact potential difference
CV	Cyclic voltammetry
DFT	Density functional theory
DMSO	Dimethyl sulfoxide
DOS	Density of states
DRS	Diffuse reflectance spectroscopy
EDX	Energy-dispersive x-ray
Eg	Energy gap
EQCN	Electrochemical quartz crystal nanogravimetry
ETD	Electrothermodeposition
FFT	Fast Fourier transform (FFT
FL	Fermi-level energy
FTO	Fluorine-doped tin oxide
GGA	Generalized gradient approximation
HER	Hydrogen evolution reaction
IPCE	Incident photon-to-electron conversion efficiency
MP	Monkhorst-Pack
NHE	Normal hydrogen electrode
Obs	Observed
OCP	Open circuit potential
ORR	Oxygen reduction reaction
PAW	Projector augmented plane wave
PBE	Perdew-Burke-Ernzerhof
PDF	Powder diffraction file
PDOS	Partial density of states
PEC	Photoelectrochemical
RHE	Reversible hydrogen electrode
SAED	Selected area electron diffraction
SDOS	Surface density of states
SEM	Scanning electron microscopy
SILAR	Successive ionic layer adsorption and reaction
SPS	Surface photovoltage spectroscopy
TBAP	Tetrabutylammonium perchlorate
TEM	Transmission electron microscopy
UV-vis	Ultraviolet-visible
VASP	Vienna ab initio simulation package
VB	Valence band

VBM	Valence band maximum
XPS	X-ray photoelectron spectroscopy
XRD	X-ray diffraction

ABSTRACT

PREPARATION AND CHARACTERIZATION OF SILVER AND COPPER VANADATES

Abbas Vali, Ph.D.

The University of Texas at Arlington, 2019

Supervising Professor: Krishnan Rajeshwar

Combining two or more binary compounds to generate a multinary compound is a viable strategy to improve the performance and properties of the parent binary compounds. In this vein, multinary compound semiconductors have recently come under the spotlight for a variety of practical device applications. In particular, the low band gaps of the Ag-V-O ternary family (Ag_3VO_4, $Ag_4V_2O_7$, $AgVO_3$, $Ag_2V_4O_{11}$, and AgV_7O_{18}) and Cu(II)-V-O ternary family (CuV_2O_6, $Cu_2V_2O_7$, $Cu_3V_2O_8$, $Cu_{11}V_6O_{26}$, and $Cu_5V_2O_{10}$) have recently garnered interest. These visible light active semiconductors may be used for photovoltaic solar cells, solar water splitting, CO_2 photoreduction, and photocatalytic remediation applications. In particular, $AgVO_3$ and Ag_3VO_4 and $Cu_2V_2O_7$ have attracted considerable interest for use as semiconductors for heterogeneous photocatalysis and water splitting processes.

Solar energy conversion applications need large active area films. Therefore, preparation techniques that are compatible with direct synthesis of semiconductor ***thin films***, are attractive. In this vein, electrochemical deposition is a fast, low temperature, and scalable process candidate. Therefore, for the first time, I successfully developed a two-step electrosynthesis technique for synthesizing $AgVO_3$, Ag_3VO_4, and $CuVO_3$ thin films on a conducting substrate. Interestingly, the as-prepared silver vanadates ($AgVO_3$ and Ag_3VO_4) were crystalline. On the other hand, the electrodeposited $CuVO_3$ thin films were unstable and amorphous. Adding a thermolysis step to electrosynthesis process converted

$CuVO_3$ to β-$Cu_2V_2O_7$. Therefore, an electrothermodeposition (ETD) strategy was developed as a versatile route for synthesizing multinary oxide thin films. Subsequently, we evaluated the optoelectronic behavior, semiconductor electronic band structure, thermal/electrochemical stability, and electrochemical/photoelectrochemical attributes of these new-generation semiconductors.

CHAPTER 1

INTRODUCTION

Development of efficient and practical oxide semiconductors for solar energy conversion and photocatalytic environmental remediation of organic pollutants has been an area of interest in the past few decades.[1-3] The oxide semiconductor should efficiently absorb visible light and additionally generate, separate, and utilize the charge carriers. Desirable properties of semiconductors are optimum band gap (~2.0 eV), proper conduction and valence band edge positions, high quantum yield, good chemical and photoelectrochemical (PEC) stability, and non-toxicity and Earth abundance of the component elements. It is difficult for a binary oxide semiconductor to satisfy all these desirable properties simultaneously. For example, a widely-studied semiconductor is TiO_2, which has proper conduction and valence band edge positions (see Figure 1-1). In addition, it has good chemical and PEC stability but it only absorbs UV light because of its large band gap (3.2 eV).[4] Of the multitude of available binary oxide semiconductors, only Cu_2O (2.00 eV),[5] CuO (1.56 eV),[6] WO_3 (2.75 eV),[7] Fe_2O_3 (2.20 eV),[8] Bi_2O_3 (2.48 eV),[9] Ag_2O (1.50 eV),[10] and V_2O_5 (2.30 eV)[11,12] have desirable optical properties (i.e., are visible-light-active) and have non-toxic elements.

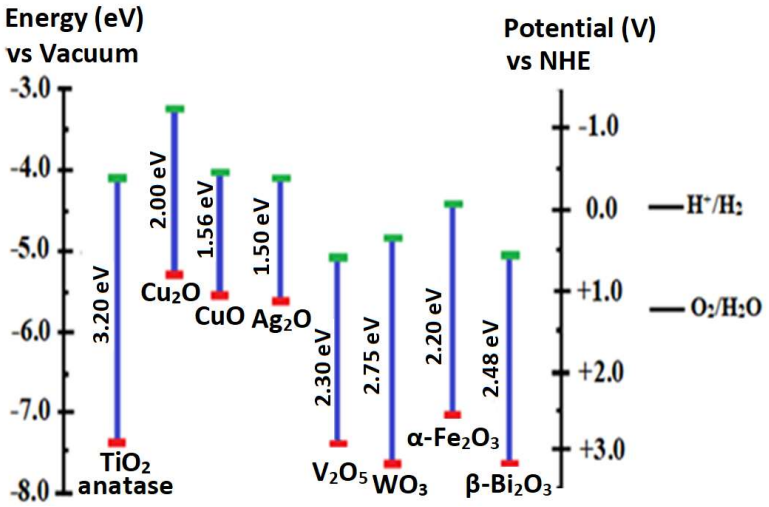

Figure 1-1. Band edge positions for non-toxic visible light active binary oxide semiconductors. Data for relevant redox potentials are also shown for comparison. These band diagrams are constructed using data from Refs. 5-12.

However, these binary oxide semiconductors have poor charge separation efficiency and/or chemical and PEC stability. To overcome these limitations, one solution is to generate ternary and quaternary oxide semiconductors from binary oxide combinations. Since combining two or more binary compounds to generate multinary compounds may thus noticeably improve the performance and properties, multinary (i.e., ternary, quaternary) compound semiconductors have recently come under the spotlight in solar fuel generation processes. For example, the band gap of V_2O_5, Nb_2O_5, and Ta_2O_5, binary oxides from the same group, decrease when they are converted to the corresponding silver-based ternary oxides, $AgVO_3$, $AgNbO_3$, and $AgTaO_3$, respectively (see Table 1-1). Hybridizing the Ag 4d with O 2p orbitals in the valence band decreases the band gap of these binary oxides.[13] Therefore, in the case of Nb_2O_5 (3.4 eV),[11] the conversion into the corresponding ternary oxide, $AgNbO_3$ (2.8 eV),[14] decreases the band gap enough so a non- visible light active semiconductor (Nb_2O_5) converts to the visible light active semiconductor ($AgNbO_3$).[14] This is not the case for the Ta_2O_5 (4.0 eV)[11] and $AgTaO_3$ (3.4 eV)[14] pair because the band gap of

$AgTaO_3$ is still too large so $AgTaO_3$ is not a visible light active semiconductor. Lastly, the V_2O_5 (2.3 eV) and its corresponding silver-based ternary oxide, $AgVO_3$ (2.04 eV),[15] are both visible light active. In addition, adding silver as a cationic element to these binary oxides may alter their valence and conduction band edge positions.

Table 1-1. Band gaps of M_2O_5 and $AgMO_3$ (M = V, Nb, and Ta). The band gap of Ag_2O is also shown for comparison.

A oxide	Band gap (eV)	B oxide	Band gap (eV)	Ternary oxide	Band gap (eV)	Band gap shrinking (eV)
Ag_2O	1.5	V_2O_5	2.30	$AgVO_3$	2.04	0.26
		Nb_2O_5	3.40	$AgNbO_3$	2.80	0.60
		Ta_2O_5	4.00	$AgTaO_3$	3.40	0.60

The band gaps of Ag-V-O ternary family (Ag_3VO_4, $Ag_4V_2O_7$, $AgVO_3$, $Ag_2V_4O_{11}$, and AgV_7O_{18} in Figure 1-2) lie in the range of 1.84 to 2.52 eV.[13, 16] Therefore, Ag-V-O ternary family can be the promising silver-based ternary oxide semiconductor to use for water splitting and photocatalytic remediation because of their small band gap. The different types of silver vanadates ($Ag_xV_yO_z$) have variant molar ratios of Ag_2O (A oxide) to V_2O_5 (B oxide) which are shown in Figure 1-2. In particular, $AgVO_3$ and Ag_3VO_4 with Ag_2O:V_2O_5 stoichiometry 1:1 and 3:1, respectively, are visible light active semiconductors and have attracted considerable interest to use as a semiconductor for photocatalysis and water splitting processes. In addition, these ternary compounds have shown significantly higher chemical stability in an aqueous medium relative to V_2O_5.[17,18] However, there is only limited information on optoelectronic behavior, semiconductor band structure, thermal and electrochemical stability, and electrochemical/photoelectrochemical

attributes of these two semiconductors. From this perspective, Chapters 2 and 3 of this dissertation focus on the study of such properties of $AgVO_3$ and Ag_3VO_4, respectively. Furthermore, a computational study on the band structure of two polymorphs of $AgVO_3$, namely α and β, has also been performed in Chapter 2.

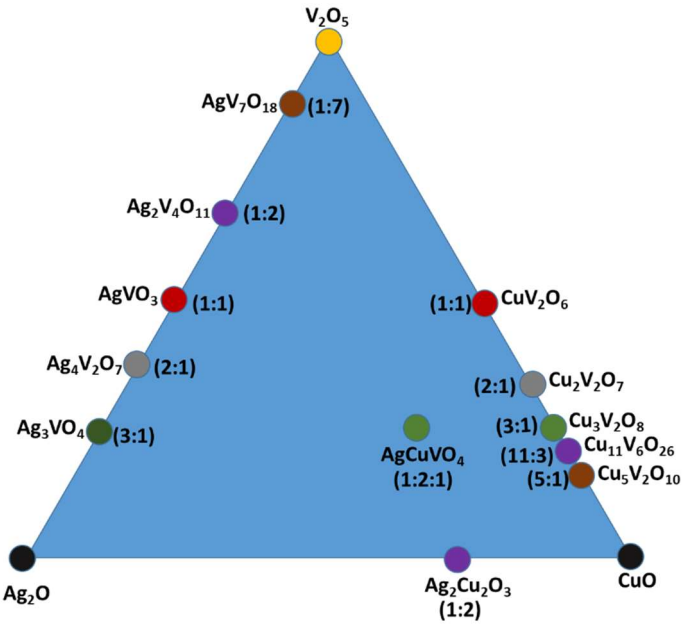

Figure 1-2. Graphical visualization of ternary and quaternary oxides in the Ag_2O–CuO–V_2O_5 system.

Adding Cu^{2+} as a cationic element to V_2O_5 is the other alternative to decrease the band gap of this binary oxide. Hybridizing the Cu 3d with O 2p orbitals in the valence band decreases the band gap of this binary oxide. Therefore, the Cu(II)-V-O family of ternary compounds (CuV_2O_6, $Cu_2V_2O_7$, $Cu_3V_2O_8$, $Cu_{11}V_6O_{26}$, and $Cu_5V_2O_{10}$ in Figure 1-2) have lower band gaps (1.86-2.05 eV) [19,20] relative to V_2O_5 (2.3 eV).[11] In addition, the Cu(II)-V-O family of ternary compounds have shown significantly higher stability in a photoelectrochemical (PEC) water splitting reaction relative to their binary oxide parents (CuO and V_2O_5). In particular, β-$Cu_2V_2O_7$ exhibited the

highest photocurrent for water oxidation at 1.23 V *vs.* RHE among the reported copper(II) vanadates.[21,22] Furthermore, β-$Cu_2V_2O_7$ showed promising photocurrent stability in a mild basic solution (pH: 9.2).[21] On the other hand, this semiconductor has low charge separation efficiency for oxygen evolution reaction (OER) due to bulk recombination and sluggish OER kinetics.[23]

One solution is to tune the thickness of the semiconductor thin film. Increasing the film thickness enhances the light absorbance (up to a point), and consequently the incident photon to current conversion efficiency (IPCE) of the given semiconductor.[17] On the other hand, when the film thickness exceeds the optimum value, the photogenerated electrons (for an n-type semiconductor) must travel a circuitous pathway to reach the conducting substrate/ semiconductor interfaces for a thick film. Thus, the recombination probability is increased. In this vein, Chapter 3 of this dissertation focuses on electrothermodeposition (ETD) of β-$Cu_2V_2O_7$, which is shown to be a versatile technique for direct deposition of a photoanode on a conducting substrate and optimization of the film thickness.

Synthetic aspects

The commonly used techniques for preparing the silver and copper vanadate powders are hydrothermal, solid state, sol-gel, and precipitation methods.[13,19] Since the product of these synthesis techniques is in powder form, an additional processing step is required to prepare a thin film of the synthesized powder to evaluate the optical parameters (e.g., photocurrent, flat band potential) of the given semiconductor. On the other hand, the popular methods for synthesizing the films of Ag-V-O and Cu(II)-V-O families are ultrahigh vacuum based methods (e.g., sputtering). Unfortunately, these methods are not applicable for preparing large effective area semiconductor devices needed for solar conversion systems. On the other hand, electrosynthetic processes are solution-based, inexpensive, and scalable. Therefore, multinary compound semiconductor thin films with large area can be synthesized using electrosynthetic

processes. From this perspective, Chapters 2 to 4 of this dissertation focus on developing a two-step electrosynthesis strategy for synthesizing $AgVO_3$, Ag_3VO_4, and $CuVO_3$ thin films on a conducting substrate, respectively. In addition, in Chapter 4, we explain in detail how adding a thermolysis process to an electrodeposition synthesis technique enhances the scope of electrochemical synthesis for preparing $Cu_2V_2O_7$ thin film.

A comment on relative contributions and outline

I was part of a team of international researchers led by Professor Krishnan Rajeshwar (Department of Chemistry and Biochemistry, the University of Texas at Arlington) and involving Professors Muhammad N. Huda (Department of Physics, the University of Texas at Arlington), Noseung Myung (Department of Energy & Materials at Konkuk University), Ki-Jung Paeng (Department of Chemistry at Yonsei University), and Csaba Janaky (Department of Physical Chemistry and Materials Science at the University of Szeged). As such and as elaborated below, the dissertation results originated from a composite of projects that were co-ordinated by myself.

However, the able assistance from other researchers in the above laboratories and a theory group (in Physics) must be acknowledged here. Specifically, Hyung-Woo Jee (Department of Chemistry at Yonsei University) did electrochemical quartz crystal nanogravimetry (EQCN) experiments detailed in Chapters 2 to 4. Hori P. Sarker (Department of Physics at the University of Texas at Arlington) conducted electronic band structure calculations presented in the computational analysis part of Chapter 2. Farinaz Firouzan (Department of Chemistry and Biochemistry, the University of Texas at Arlington) performed forward-bias current–potential polarization experiments described in Chapters 2 and 3. Attila Kormányos (University of Szeged, Hungary) performed Kelvin-probe microscopy (KPM) and ambient pressure UV photoelectron spectroscopy (AP-UPS) with the data presented in Chapter 2. Peter S. Toth (also at the University

of Szeged, Hungary) performed KPM, high-resolution transmission electron microscopy, surface photovoltage spectroscopy, and AP-UPS with the outcomes described in Chapter 3.

All other aspects of this collaborative dissertation work, namely sample preparation and treatment, data analyses, quantitative analyses of EQCN, and miscellaneous electrochemical and photoelectrochemical data were done by me. Accordingly, the resulting peer reviewed papers that accrued from this work represent the bulk of what follows in this document and all these articles feature me as the first author. However, a brief introductory chapter sets the stage for these papers that follow with a summary section also provided at the end, along with perspectives on future research avenues.

References

(1) Seabold, J. A.; Choi, K. S. Efficient and Stable Photo-Oxidation of Water by A Bismuth Vanadate Photoanode Coupled with An Iron Oxyhydroxide Oxygen Evolution Catalyst. *J. Am. Chem. Soc*., **2012**, *134*, 2186−2192.

(2) Kudo, A.; Miseki, Y. Heterogeneous Photocatalyst Materials for Water Splitting. *Chem. Soc. Rev.,* **2009**, *38*, 253-278.

(3) Osterloh, F. E. Inorganic Materials as Catalysts for Photochemical Splitting of Water. *Chem. Mater.,* **2008**, *20*, 35-54.

(4) Beranek, R. (Photo)electrochemical Methods for the Determination of the Band Edge Positions of TiO_2-Based Nanomaterials, *Adv. Phys. Chem.* **2012**, *2011*, 786759.

(5) Nagasubramanian, G.; Gioda, A. S.; Bard, A. J. Photoelectrochemical Behavior of p-Type CuO in Acetonitrile, *J. Electrochem. Soc.* **1981**, *128*, 2158-2164.

(6) Nakaoka, K.; Ueyama, J.; Ogura, K. Photoelectrochemical Behavior of Electrodeposited CuO and Cu_2O Thin Films on Conducting Substrates, *J. Electrochem. Soc.* **2004**, *151*, C661-C665.

(7) Li, W.; Zhan, F.; Li, J.; Liu, C.; Yang, Y.; Li, Y. Qiyuan Chen Enhancing Photoelectrochemical Water Splitting by Aluminum-Doped Plate-Like WO_3 Electrodes. *Electrochim. Acta.* **2015**, *160*, 57-63.

(8) Hankin, A.; Bedoya-Lora, F. E.; Alexander, J. C.; Regoutz, A.; Kelsall, G. H. Flat Band Potential Determination: Avoiding the Pitfalls. *J. Mater. Chem. A* **2019**, *7*, 26162-26176.

(9) Chitrada, K. C.; Gakhar, R.; Chidambaram, D.; Aston, E.; Raja, K. S. Enhanced Performance of β-Bi_2O_3 by In-Situ Photo-Conversion to Bi_2O_3-BiO_{2-x} Composite Photoanode for Solar Water Splitting. *J. Electrochem. Soc.* **2016**, 163, H546-H558.

(10) Jiang, Z.; Huang, S.; Qian, B. Semiconductor Properties of Ag_2O Film Formed on the Silver Electrode in 1M NaOH Solution. *Elecrochim. Acta.* **1994**, *39*, 246-2470.

(11) Wachs, I. E.; Chen, Y.; Jehng, J-M.; Briand, L. E.; Tanaka, T. Molecular Structure and Reactivity of the Group V Metal Oxides. *Catal. Today*, **2003**, *78*, 13–24.

(12) Teran-Escobar, G.; Pampel, J.; Caicedo, J. M.; Lira-Cant, M. Low-Temperature, Solution-Processed, Layered V_2O_5 Hydrate as the Hole-Transport Layer for Stable Organic Solar Cells. *Energy Environ. Sci.* **2013**, *6*, 3088–3098.

(13) Galante, M. T.; Sotelo, P.; Hossain, M. K.; Vali, A.; Raamann, A.; Longo, C.; Macaluso, R. T.; Rajeshwar, K. Silver Oxide-Based Semiconductors for Solar Fuels Production and Environmental Remediation: A Solid-State Chemistry Approach. *ChemElectroChem* **2019**, *6*, 87–96.

(14) Arney, D.; Hardy, C.; Greve, B.; Maggard, P. A. Flux synthesis of $AgNbO_3$: Effect of Particle Surfaces and Sizes on Photocatalytic Activity. *J. Photochem. Photobiol. A Chem.* **2010**, *214,* 54–60.

(15) de Oliveira, R. C.; Assis, M.; Teixera, M. M.; da Silva, M. D. P.; Li, M. S.; Andres, J.; Gracia, L.; Longo, E. An Experimental and Computational Study of β-$AgVO_3$: Optical Properties and Formation of Ag Nanoparticles. *J. Phys. Chem. C* **2016**, *120*, 12254-12264.

(16) Wang, J.; Yang, X.; Chen, J.; Xian, J.; Meng, S.; Zheng, Y.; Shao, Y.; Li, D. Photocatalytic Activity of Novel $Ag_4V_2O_7$ Photocatalyst Under Visible Light Irradiation. *J. Am. Ceram. Soc.* **2014**, *97*, 267−274.

(17) Hardee, K. L.; Bard, A. J. Semiconductor Electrodes: X. Photoelectrochemical Behavior of Several Polycrystalline Metal Oxide Electrodes in Aqueous Solutions. *J. Electrochem. Soc.* **1977**,*124*, 215−224.

(18) Briton, H. T. S.; Robinson, R. A. Physicochemical Studies of Complex Acids. Part IV. The Vanadates of Silver. *J. Chem. Soc.* **1930**, *0*, 2328–2343.

(19) Rajeshwar, K.; Hossain, M. K.; Macaluso, R. T.; Janáky, C.; Varga, A.; Kulesza, P. J. Copper Oxide-Based Ternary and Quaternary Oxides: Where Solid-State Chemistry Meets Solar Fuels. *J. Electrochem. Soc.* **2018**, *165*, H3192−H3206.

(20) Song, A.; Berglund, S. P.; Chemseddine, Friedrich, A.; D.; Abdi, F. F.; de Krol, R. V. Elucidating the Optical, Electronic, and Photoelectrochemical Properties of p-type Copper Vanadate (p-$Cu_5V_2O_{10}$) Photocathodes. *J. Mater. Chem. A*, **2020**, *8*, 12538–12547.

(21) Hossain, M. K.; Sotelo, P.; Sarker, H. P.; Galante, M. T.; Kormányos, A.; Longo, C.; Macaluso, R. T.; Huda, M. N.; Janáky, C.; Rajeshwar, K. Rapid One-Pot Synthesis and Photoelectrochemical Properties of Copper Vanadates. *ACS Appl. Energy Mater*, **2019**, *4*, 2837−2847.

(22) Newhouse, P. F.; Boyd, D. A.; Shinde, A.; Guevarra, D.; Zhou, L.; Soedarmadji, E.; Li, G.; Neaton, J. B.; Gregoire, J. M. Solar Fuel Photoanodes Prepared by Inkjet Printing of Copper Vanadates. *J. Mater. Chem. A* **2016**, *4*, 7483−7494.

(23) Song, A.; Chemseddine, A.; Ahmet, I. Y.; Bogdanoff, P.; Friedrich, D.; Abdi, F. F.; Berglund, S. P.; van de Krol, R. Evaluation of Copper Vanadate (β-$Cu_2V_2O_7$) as a Photoanode Material for Photoelectrochemical Water Oxidation.*Chem. Mater.* **2020**, *32*, 2408−2419.

(24) Lund, E.; Galeckas, A.; Monakhov, E. V.; Svensson, B. G. Basic Optical and Electronic Properties of $Ag_2Cu_2O_3$ Crystalline Films. *Thin Solid Films*, **2013**, *531*, 185–188

(25) Möller, A.; Schmitt, M.; Schnelle, W.; Förster, T.; Rosner, H. $AgCuVO_4$: A Quasi One-Dimensional S = 1/2 Chain Compound. *Phys. Rev. B*, **2009**, *80*, 125106.

CHAPTER 2

Electrodeposition of Silver Vanadate Films: A Tale of Two Polymorphs

Used with permission from A. Vali, H. P. Sarker, H-W. Jee, A. Kormányos, F. Firouzan, N. Myung, K-J. Paeng, M. N. Huda, C. Janáky, K. Rajeshwar, *ChemPhysChem.* **2019**, 20, 2635–2646.
 https://doi.org/10.1002/cphc.201900558

ABSTRACT:

Two polymorphs of $AgVO_3$, namely the α- and β- forms, were prepared and their physical, structural, optical, electrochemical, and photoelectrochemical characteristics were compared using a battery of experimental and theoretical tools. A two-step method, previously developed in the Rajeshwar laboratory for the electrodeposition of inorganic semiconductor films, was applied to the electrosynthesis of silver vanadate ($AgVO_3$) films on transparent, conducting oxide surfaces. In the first step, silver was cathodically-deposited from a non-aqueous bath containing silver nitrate. In the second step, the silver film was anodically-stripped in an aqueous medium containing ammonium metavanadate solution. The anodically-generated silver ions at the interface underwent a precipitation reaction with the vanadate species to generate the desired product in situ. Each of these steps were mechanistically corroborated via the use of electrochemical quartz crystal microgravimetry, used in conjunction with voltammetry and coulometry. As-deposited films were crystalline and showed p-type semiconductor behavior. Theoretical insights are provided for the electronic origin of the α → β phase transformation in $AgVO_3$. Finally, implications for the application of this material in solar cells are provided.

2.1. INTRODUCTION

Silver oxide-based semiconductors have recently come under the spotlight in the continued search for candidates for photovoltaic solar cells, solar water splitting, CO_2 photoreduction, and environmental remediation applications.[1] Of these, ternary compounds generated from the two binary components, namely, Ag_2O and V_2O_5, and exhibiting a range of Ag_2O: V_2O_5 stoichiometries (1:7, 1:2, 1:1, 2:1, 3:1; see Figure 2-1), have elicited both fundamental and practical interest (see review in Ref. 2) In particular, $AgVO_3$ has attracted considerable interest because of its wide-ranging practical applications including batteries, sensors, antibacterial formulations, and as photocatalysts for pollutant decomposition.[3-16]

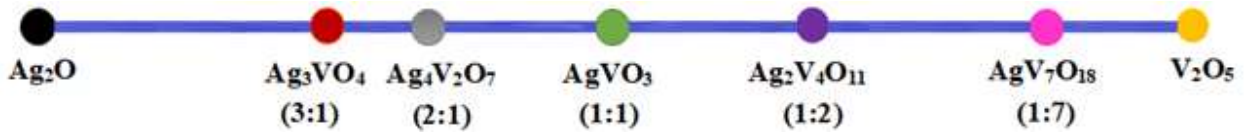

Figure 2-1. Composition line diagram showing the five stoichiometries in the Ag-V-O ternary system.

Polymorphism in $AgVO_3$ has provided a platform for many studies; this compound exhibits up to four different crystallographic forms, namely, α, β, γ and δ forms.[2] The most common are the metastable α and thermodynamically- stable β polymorphs with monoclinic space groups *Cm* and *C2/c*, respectively.[2,15] The structural aspects of the two polymorphs and the component AgO_x and VO_4 clusters in them along with their relative juxtapositions, are well described in the literature.[3,4,13,14,16] It is worth noting, that aside from an early study,[3] we are not aware of too many other instances where the two polymorphs have been directly compared. Hydrothermally-derived α-$AgVO_3$ microrods were transformed to β-$AgVO_3$ nanowires; the battery performance of the latter was observed to be superior in galvanostatic discharge-charge measurements.[4] Examining

another study on microwave-assisted hydrothermal synthesis,[7] the photocatalytic activity of β-$AgVO_3$ appears to be superior to α-$AgVO_3$ although this comparison is confounded by the higher surface area of the β- polymorph.

As reviewed by other authors,[2] this ternary compound has been synthesized in a range of nanostructures (nanorods, nanobelts, nanoribbons, and nanowires) using methods ranging from hydrothermal (most common) to biomineralization along with other hybrid and more esoteric approaches including the use of pulsed laser deposition, microwave assistance, ultrasonic agitation etc. Conspicuous in its absence is the use of electrodeposition[17-23] for $AgVO_3$ synthesis. Given the versatility of electrosynthetic procedures,[17-23] this omission is rather surprising. This paper therefore describes the application of the two-step approach (Figure 2-2), previously developed in the Rajeshwar laboratory,[24-28] for the electrodeposition of $AgVO_3$ films on transparent, conducting oxide glass (fluorine-doped tin oxide or FTO) substrates.

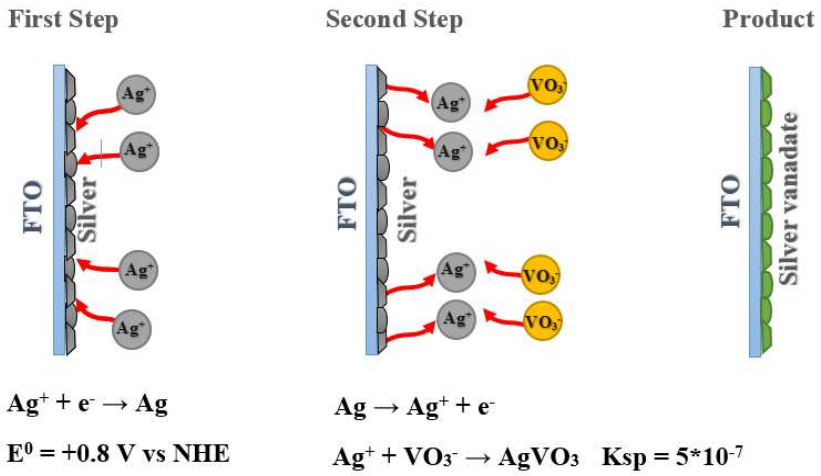

Figure 2-2. Schematic diagram for the two-step electrosynthesis of $AgVO_3$.

The two-step approach was previously used for the electrosynthesis of metal chalcogenides and bismuth vanadate ($BiVO_4$).[24-28] This method hinges on the tunability afforded by the tremendous

electric field strength that exists across an electrode/electrolyte interphase (nominally, several million V/cm) to tweak precursor ion fluxes. This feature, coupled with the usual variables in *homogeneous* aqueous reaction scenarios (e.g., solution pH), considerably enhances the synthetic scope as demonstrated in this study, for the $AgVO_3$ case.

In a more general sense, this study also serves to demonstrate the use of electrodeposition as a scalable preparation methodology for solar cell applications of complex metal oxides. Thus far, this methodology has been confined largely for such preparation of *binary* metal oxides or chalcogenides.[17-23] In the case of multinary chalcogenides (e.g., copper zinc tin sulfide or CZTS), a *hybrid* strategy, combining, for example, metal electrodeposition followed by sulfidation,[29] was employed unlike the strategy in this study. In the present case, both the component steps are electrochemical in origin with attendant advantages.[17, 20.21]

2.2. RESULTS AND DISCUSSION

2.2.1. Mechanistic Insights into the Two-Step Electrodeposition of $AgVO_3$

The choice of a non-aqueous electrolyte for silver deposition was prompted by the need to avoid hydrogen evolution and to secure metal films free from oxide contamination. To this end, the solutions were purged with nitrogen to prevent the oxygen reduction reaction (ORR). Figure A-S1 compares the cyclic voltammograms for silver ion reduction and silver stripping on Pt (solid line) and FTO (dashed line) electrode surfaces. The reduction wave is shifted more negative and the leading edge of the stripping wave is more drawn out for FTO relative to Pt. These trends are reflective of the higher series resistance for FTO and the more sluggish electron transfer kinetics relative to the Pt surface. Importantly, however, the overall voltammetry profiles are otherwise essentially similar in the two cases.

The cross-over of the forward (reduction) and reverse (oxidation) voltammetry traces indicates the nucleation/growth of silver on the FTO substrate.[30,31] The sharp current drop after the anodic wave (peaking at +0.75 V for FTO) indicates the complete anodic stripping of metallic silver (Figure A-S1). Similar behavior could be seen for Pt, albeit at a more negative potential (~0.56 V) for the stripping wave. Based on these data, the silver film was prepared by sweeping the potential from +0.15 to -0.80 V 10 times at a 25 mV/s scan rate.

Figure A-S2 contains the EQCM-voltammetry-coulometry data for the first step; Figure A-S2a contains the frequency change and the cathodic Ag deposition voltammetry regime. The frequency decrease along the reduction wave domain is diagnostic of mass gain and the electrodeposition of a film (presumably Ag) on the Pt-coated quartz surface.[27,28,32] Further insight into the deposition mechanism can be gleaned by combining the EQCM data with coulometric assay for the reduction:[32-34]

$$Q = -\left(\frac{nFk}{M}\right)\Delta f \qquad (2\text{-}1)$$

Q is the charge consumed, F is the Faraday constant, Δf is the frequency change, k is the Sauerbrey constant,[32-34] and M is the molar mass of the deposit. By constructing a Q versus $-\Delta f$ plot (Figure A-S2b), one can calculate the electron stoichiometry, n from the slope. The calculated n value from the least-squares fitted slope was 0.94, sensibly close to the value expected from the following reduction process:

$$Ag^+ + e^- \rightarrow Ag \qquad (2\text{-}2)$$

The XRD and EDS patterns of the as-synthesized silver film are shown in Figures A-S3 and A-S4, respectively. These results, along with the EQCM-voltammetry-coulometry data, unequivocally confirm that the synthesized film is composed of pure elemental silver. In the second step, the silver film was stripped anodically to generate Ag^+ in an aqueous solution of

ammonium metavanadate (pH: 7.0). Subsequent in situ precipitation of these ions with VO_3^-, driven by the low solubility product for $AgVO_3$ (K_{sp} = 5.0 x 10^{-7})[35] yielded a *green* $AgVO_3$ film on the substrate. The choice of the above medium pH for the anodic stripping stage reflects literature evidence[36] for the preponderance of VO_3^- species in the 6.0–9.0 range. At higher pH values, other species (VO_4^{3-}) become more stable.

A linear sweep voltammogram (solid line) and the corresponding EQCM frequency change (dotted line) during film deposition, are shown in Figure 2-3a. The frequency decrease during the positive-going scan is diagnostic of mass gain according to the following scheme:

$$Ag \rightarrow Ag^+ + e \qquad (2\text{-}3)$$

$$Ag^+ + VO_3^- \rightarrow AgVO_3 \qquad (2\text{-}4)$$

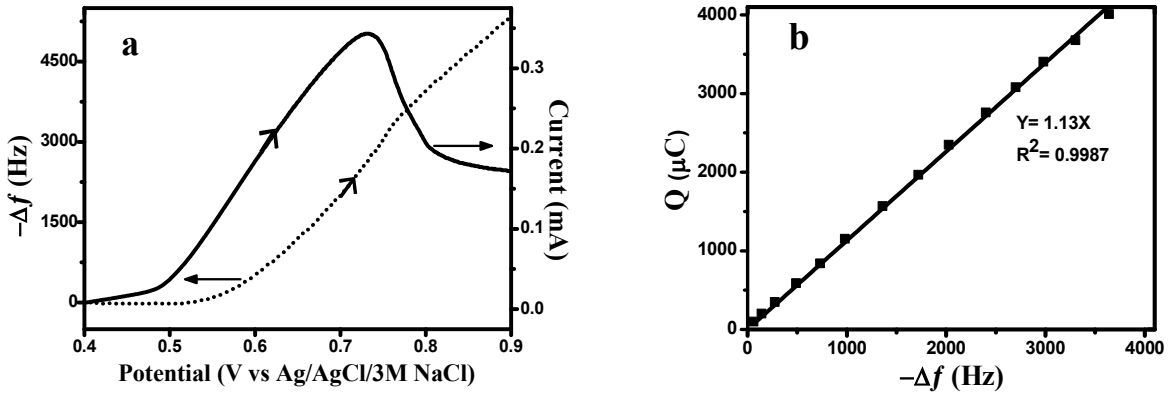

Figure 2-3. (a) Linear sweep voltammmogram (—) and the corresponding EQCM frequency change (....) for the electrodeposition of silver vanadate at 15 mV/s potential scan rate. (b) Charge-frequency change plot derived from the EQCM-voltammetry data.

The slight lag in the mass gain relative to the current flow onset in Figure 2-3a is worthy of note and signals the fact that precipitation intrinsically is a kinetically slow process. The associated charge (Q) versus frequency changing (−Δf) plot of electrodeposition of $AgVO_3$ is shown in

Figure 2-3b. The calculated *n* value from the slope of the least-squares fitted line was 1.06, close to the stoichiometry value expected from reaction 3.

The effect of scan rate on the potentiodynamic film growth in the second step deserves comment. A high scan rate (e.g., 25 mV/s) results in uneven film growth on the support surface. On the other hand, a low scan rate (e.g., 5 mV/s) is non-optimal from a synthesis time perspective, and importantly, also results in partial desorption of precipitated $AgVO_3$ from the support electrode surface. A potential scan rate in the range, 10-15 mV/s, was found to provide a reasonable compromise and yielded good film adhesion and product quality (see below).

2.2. Physical Characterization of the Silver Vanadate Film

Interestingly, XRD pattern of the as-prepared film (Figure A-S5) showed that the synthesized film was crystalline (even without thermal anneal) in α-$AgVO_3$ form. Significantly, this crystallinity was afforded despite the electrodeposition being conducted at ambient temperature. The as-prepared α-$AgVO_3$ film was annealed at two different temperatures, 150 ºC and 250 ºC, for 30 min to prepare β-$AgVO_3$. The XRD patterns of these samples (Figures A-S5, patterns d and e) showed that the samples annealed at 150 ºC and 250 ºC were in the α-$AgVO_3$ and β-$AgVO_3$ polymorphic forms, respectively. Thus, the green α-$AgVO_3$ polymorph thin film was transformed to a reddish β-$AgVO_3$ between 150 ºC to 250 ºC. This is in good agreement with the reported exothermic phase transformation temperature (249 ºC) from α-$AgVO_3$ to β-$AgVO_3$. [36] The transformation from α-phase to β-phase was accompanied by the formation of traces of silver (the peak at 38.3º in Figure A-S5, pattern e). This observation is consistent with the thermolysis of β-$AgVO_3$ to Ag_2O and $Ag_2V_4O_{11}$,[37] and subsequently to Ag.[38] The presence of metallic silver in β-$AgVO_3$ was observed by TEM in previous studies.[6] Silver is of interest because of its plasmonic possibilities for solar cell applications.

Morphological examination of the *as-prepared* samples by SEM and EDS revealed excellent crystallinity and one-dimensional film growth in the form of nanorods, see Fig. 2-4 as an example. Elemental EDS maps (not shown) indicated uniform film deposition across the entire support electrode surface. Specifically, no regions rich in silver could be found, for example. Compositional EDS assays averaged from different spots (see Experimental Section) were consistent with the film composition: $Ag_{0.94\pm0.02}V_{1.02\pm0.01}O_{2.90\pm0.07}$; a representative EDS trace is shown in Figure A-S6 in the Supplemental Information.

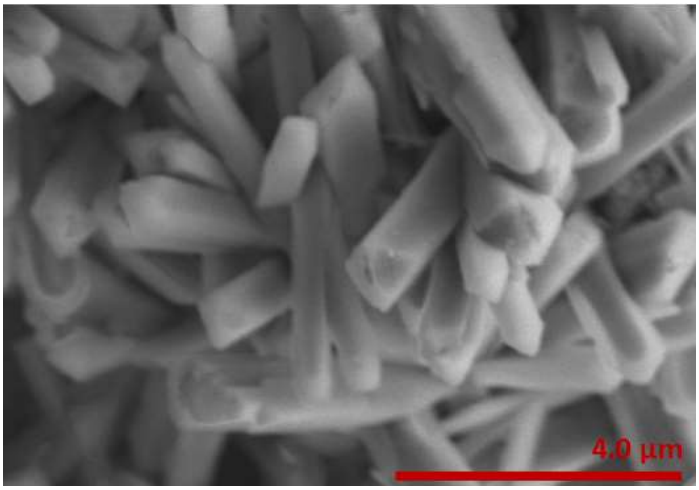

Figure 2-4. Representative scanning electron micrograph of an as-prepared silver vanadate film on FTO.

X-ray photoelectron spectra in the survey mode (not shown) showed no elements other than the expected Ag, V, and O along with the ubiquitous signal from (adventious) carbon. High resolution spectra for the Ag 3d, V 2p, and O is binding energy regimes for the electrodeposited samples (not shown) were in broad agreement with those reported in the literature for samples derived from other synthesis methods.[12,13,39] Film compositional purity is critical for solar cell applications and these data demonstrate that electrodeposition does meet this requirement.

2.2.3. Optical Behavior

Tauc plots[40] were constructed from the UV/visible diffuse reflectance spectral data. Figures A-S7 and 2-5 contain these plots for the as-deposited α-$AgVO_3$ samples and the β-$AgVO_3$ counterparts obtained after thermal anneal, respectively. Both direct and indirect optical transitions are indicated with corresponding energy band gaps of 2.72 eV and 2.45 eV for α-$AgVO_3$ and 2.47 eV and 2.12 eV for β-$AgVO_3$, respectively. Table 2-1 presents a comparison of these values with those reported in the literature for samples prepared using other techniques. There is some scatter in the reported experimental values for the energy band gaps of the two polymorphs, and the values quoted also have varying precision (Table 2-1). This issue has been discussed by us elsewhere[42] and is a problem associated with many confounding factors, some of which have to do with the method of extraction of the band gap values from the spectral information.[40] Nonetheless, a safe conclusion can be made that the β- polymorph has a narrower gap than the α- counterpart. The underlying factors in this trend are discussed in the next section on electronic band structure calculations.

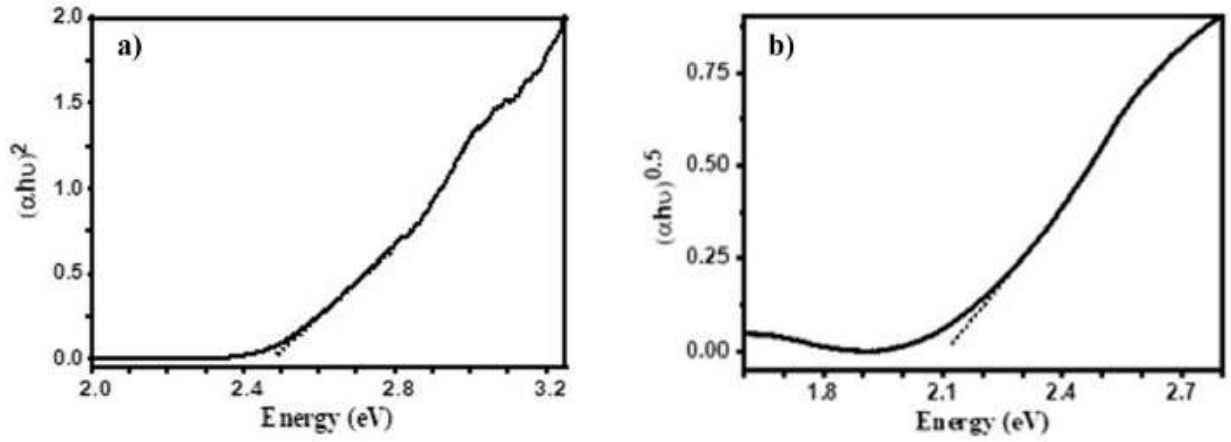

Figure 2-5. Tauc plots for β-$AgVO_3$ film on FTO. Frames (a) and (b) contain the plots analyzed for direct and indirect optical transitions respectively.

Table 2-1. Experimental and calculated energy bandgap values along with literature data.

Oxide	E_{VB} / eV[a]	Theoretical band gap (eV)		Experimental band gap (eV)[b]		Literature Values (eV)	Ref.
		Direct	Indirect	Direct	Indirect		
α-$AgVO_3$	-5.62	2.42	2.33[c]	2.72	2.45	2.50 2.50 2.22	3 7 41
β-$AgVO_3$	-5.38	2.00	1.94[d]	2.47	2.12	2.01 2.04 2.43 ~2.2 2.3	5 14 39 12 7

[a]See Fig. 2-10a below.
[b]See Figs. A-S7 and 2-5.
[c]See Fig. 2-7 below.
[d]See Fig. 2-8 below.

2.2.4. Electronic Band Structure Calculations

The lattice parameters and the atomic positions in the crystal structures of the two polymorphs were optimized prior to the band structure calculations. Figures 2-6a and b depict the unit cells containing 8 Ag atoms, 8 V atoms and 24 O atoms within the unit cell for both polymorphs. The calculated and experimental lattice parameter values along with other reported results[15,36,37] are presented in Table A-S1. The calculated values are in good agreement with the experimental values for both polymorphs of $AgVO_3$ except for the β angle in α-$AgVO_3$. The calculated β angle of α-$AgVO_3$ is overestimated compared to the experimental value by 11.0 % but it is close to the reported theoretical results in a previous study.[15]

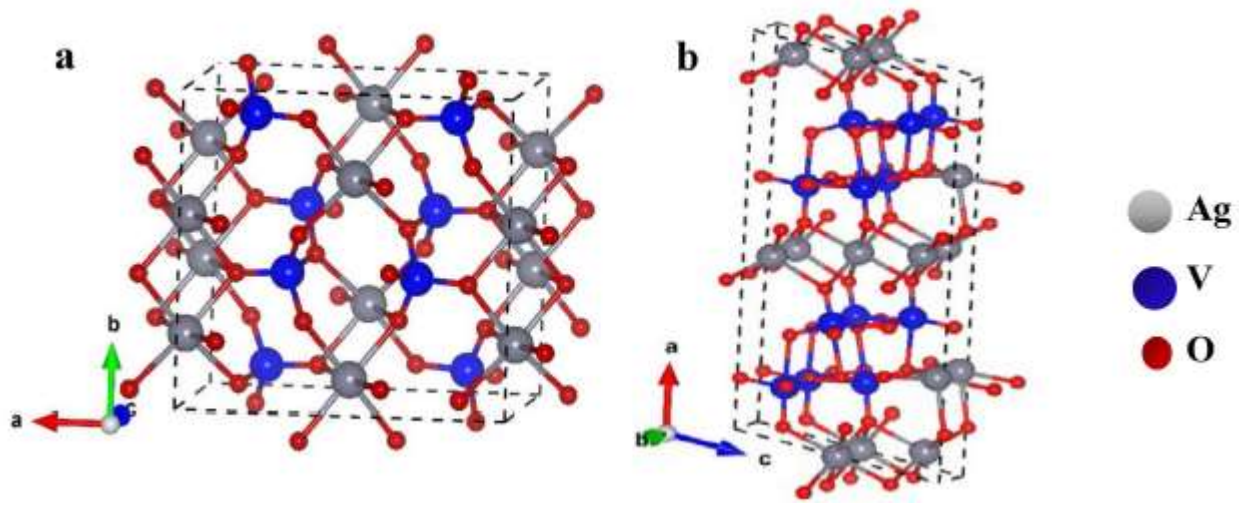

Figure 2-6. DFT + U relaxed unit cells for a) α-$AgVO_3$ and b) β-$AgVO_3$.

Figures 2-7a and b show the DFT + U-derived electronic band structure and partial density of states (pDOS) for α-$AgVO_3$. The Fermi energy level is defined as the highest occupied electronic state and is indicated by 0 eV. The valence band is mainly composed of Ag 4d and O 2p states, as seen in the partial density of states plot (Figure 2-7b) and in the band decomposed charge density plot (Figure 2-7c, bottom panel). The Ag 4d and O 2p and states are strongly hybridized in the valence band. The dispersion of valence band along all the high symmetry directions in the Brillouin zone indicates that the photoexcited holes have low effective mass.

The conduction band of α-$AgVO_3$ is mainly composed of anti-bonding V 3d and O 2p states, as seen in the partial density of states plot (Figure 2-7b, right panel) and the band decomposed charge density plot of (Figure 2-7c, top panel). The strongly hybridized bonding part of V 3d and O 2p appears at the bottom of the valence band, as can be seen in Figure A-S6(a). The total width of the valence band is 4.5 eV, which is bounded by strongly hybridized Ag *d* and V *d* bands from the upper and at the bottom side, respectively. The fundamental band gap of α-$AgVO_3$ is indirect in nature, because the conduction band minima (CBM) is located between the Γ and Z points and the valence band maxima (VBM) is placed at point Γ. The calculated indirect bandgap is 2.33 eV

which is close to the band gap value (2.45 eV) obtained via DRS and the calculated direct gap is 2.42 eV (Table 2-1). The calculated electronic band structure and density of states plot have similar features with another reported result,[15] but the calculated indirect band gap by the B3LYP and HSE06 methods overestimate the reported experimental band gap value by 52% and 38%, respectively. On the other hand, the PBE calculation underestimates the reported experimental indirect band gap by 28%.

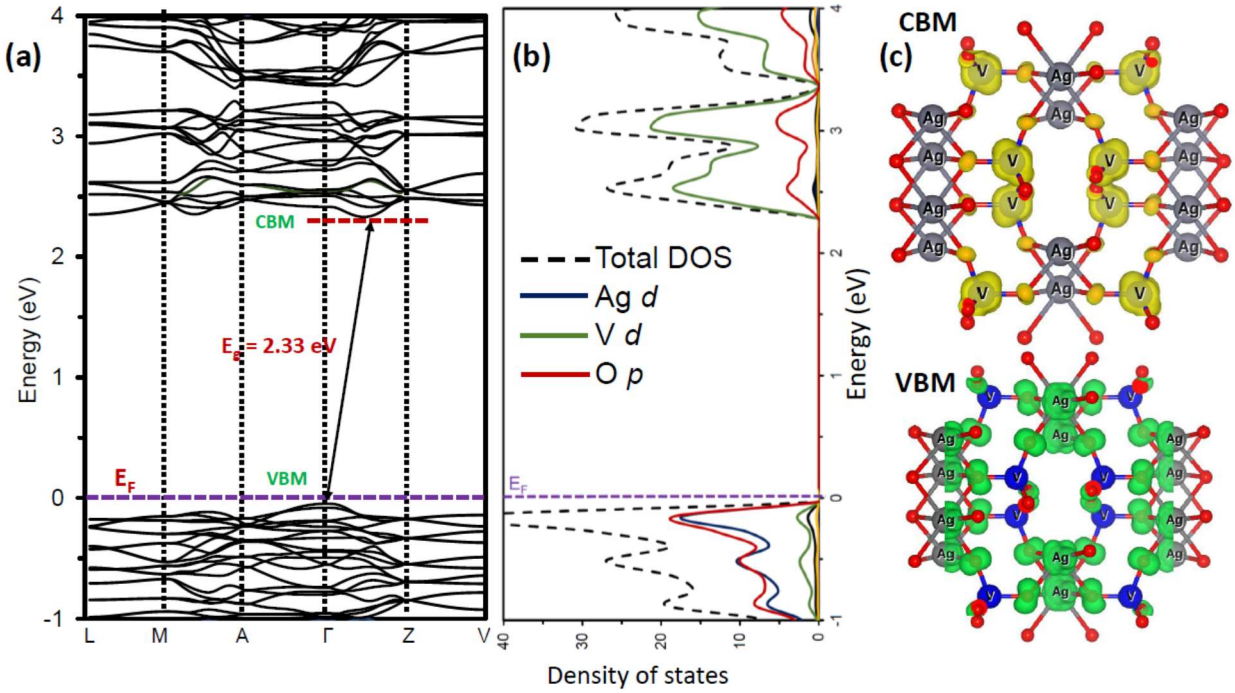

Figure 2-7. a) Band structure and b) partial density of states of α-$AgVO_3$ and c) Band decomposed charge density of valence band maxima (VBM) (bottom panel) and conduction band minima (CBM) (upper panel) for α-$AgVO_3$.

Figures 2-8a and b show the electronic band structure and partial density of states (pDOS) for β-$AgVO_3$. From the density of states plot and band-decomposed charge density plot of VBM (in Figures 2-8b and c (bottom panel), respectively) we see that, here again, the valence band is mainly composed of Ag 4d and O 2p states. However, for β-$AgVO_3$, Ag 4d and O 2p are not as strongly

hybridized near the Fermi level as they are for α-$AgVO_3$. The calculated pDOS (Figure 2-8b) and band-decomposed charge density of CBM plot (Figure 2-8c, upper panel) confirm that the conduction band of β-$AgVO_3$ is composed of V 3d and O 2p states with predominent contribution of V 3d orbitals. Note that near the CBM of β-$AgVO_3$, the contribution from V 3d is not as prominent as in α-$AgVO_3$. Similarly, at the bottom of the valence band, the bonding part of V 3d and O 2p hybridization is not as strong as in α-$AgVO_3$.

The valence band with is about 5.5 eV, which is 1 eV wider than in that of α-$AgVO_3$. This implies that electron correlation strength in α-phase is higher than in the β-$AgVO_3$ phase. The theoretical fundamental bandgap of β-$AgVO_3$ is indirect in nature because the CBM is located at point V and VBM is located between the Γ and Z points. The calculated indirect gap of β-$AgVO_3$ is 1.94 eV which is close to the obtained indirect band gap (2.12 eV) obtained via DRS and the calculated direct gap is 2.00 eV (Table 2-1). The calculated electronic band structure and density of states in this study have broad similarity with the other reported results in the literature.[12,15]

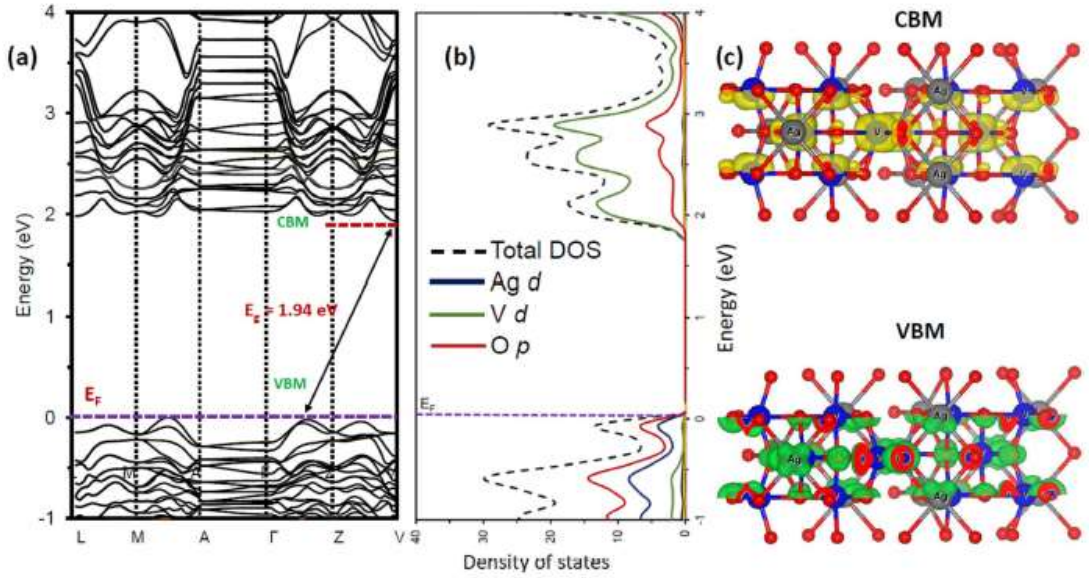

Figure 2-8. a) Band structure and b) partial density of states (pDOS) of β-$AgVO_3$ and c) Band decomposed charge density of valence band maxima (VBM) (bottom panel) and conduction band minima (CBM) (top panel) for β-$AgVO_3$.

2.2.5. Electronic Origin of the α to β Phase Transformation in $AgVO_3$

From the electronic structures discussed above, we now reiterate several observations: (i) Anti-bonding O 2p and Ag 4d hybridization near the top of the valence band is stronger in the α-phase than in β-phase, whereas the bonding hybridizations are at about - 17 eV below the Fermi level (not shown in the figure) for both the phases. (ii) Similarly, O 2p and V 3d hybridization at the bottom of valence band is stronger in the α-phase than in β-phase. (iii) The valence band width in the α-phase is 1 eV narrower than that of the β-phase. These all imply that electron correlation is stronger in the α-$AgVO_3$ polymorph. Note that, strongly hybridized V 3d with O 2p band in α-$AgVO_3$ at the bottom of the valence band implies some electronic occupation of V 3d band. Hence, the oxidation state of V in α-$AgVO_3$ is not exactly +5, rather $V^{+(5-\delta)}$. Figure 2-9a shows very symmetric V- O tetragonal bonding features in α-$AgVO_3$.

As seen in Figure 2-9a, the strongly hybridized O 2p and Ag 4d anti-bonding features create layers of Ag−O polyhedra in α-$AgVO_3$. These polyhedra line-up as a linear structure within the crystal along the z-direction, separated by about 7 Å in the y direction. The nearest Ag−Ag distance is along the z-direction, 3.326 Å, which is shown in the figure. The other structural nuances in the two polymorphs were noted earlier.

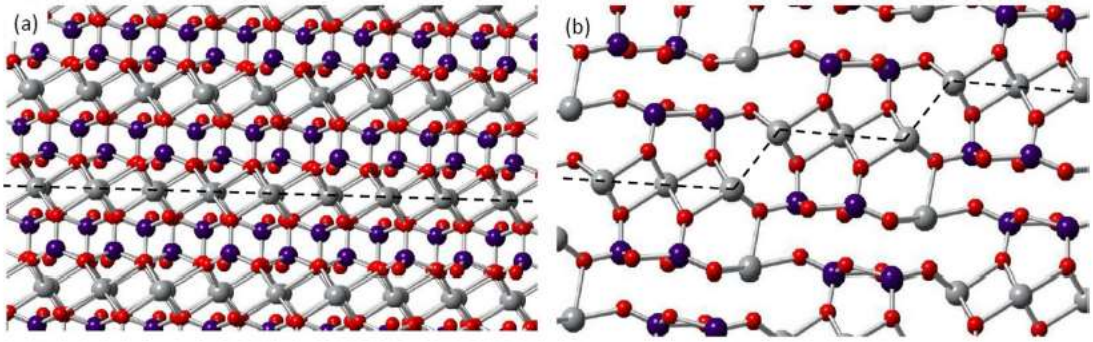

Figure 2-9. (a) α-$AgVO_3$ and (b) β-$AgVO_3$ crystal structures to compare the structural relaxation during the α-to-β phase transformation. The α→β transition is exothermic. The dashed line in frame (a) shows the 1D linear chain in α-$AgVO_3$. Along the y-direction, the layers are 6.919 Å apart. Gray, red and purple balls represent Ag, O and V atoms, respectively.

In addition, the strongly hybridized O 2p and Ag 4d anti-bonding features create layers of Ag-O polyhedra in α-$AgVO_3$ as shown in Figure 2-9a. The nearest Ag-Ag distance along the figure is 3.326 Å. In β-$AgVO_3$ these symmetric Ag-O polyhedra go through drastic transformations with step-wise broken polyhedron layers, as seen in Figure 2-9b. In β-$AgVO_3$, two adjacent polyhedra occur at a time, with two Ag-Ag distances, 3.384 Å and 3.452 Å. In fact, α-$AgVO_3$ has alternate layers of Ag-O polyhedra and V-O bonding framework.

Two points are noted in the α to β phase transformation: (i) The periodic arrangements of Ag atoms in α-$AgVO_3$ transform into irregular doublet units with a longer periodic range in β-$AgVO_3$, which is a signature of Peierls type distortion. (ii) A given horizontal layer in β-$AgVO_3$ has both V-O and Ag-O bonds, whereas before the α to β phase transformation the V-O layers did not contain any Ag atoms. This results in some vertical V-O bonds breaking in β-$AgVO_3$ as evident from Figure 2-9b. This second event enables V atoms to get rid of some 3d electrons, and hence, to reach a more ideal favorable V^{+5} state. The two phenomena in unison help lower the energy barrier for the α– to β– $AgVO_3$ phase transformation, and the β-$AgVO_3$ phase becomes energetically more favorable.

2.2.6. Conduction and Valence Band Locations in α- and β-$AgVO_3$

Ambient-pressure UV photoelectron spectroscopy (AP-UPS) was used to map the valence band maxima (VBM) in α-$AgVO_3$ and β-$AgVO_3$. Figure 2-10a contain the data; from the intercepts of the plots, the VBM were located. These values on the vacuum energy scale are given in Table 2-1 above. Using these values and the energy band gaps for the two polymorphs, the conduction and valence band positions for the two compounds can be estimated. These are given in Figure 2-10b. The valence band offset is 0.24 eV and these two phases have Type-I bandgap offset. The theoretically-obtained valence band offset (0.19 eV), which was calculated by taking highly

localized O-s band as the reference bands, agrees reasonably well with the measured value above. Clearly, the band positions are not favorable for water photooxidation. Such a conclusion is entirely consistent with the experimental findings from an earlier study[3] which noted that both α-$AgVO_3$ and β-$AgVO_3$ had zero activity for photo generating O_2 from water.

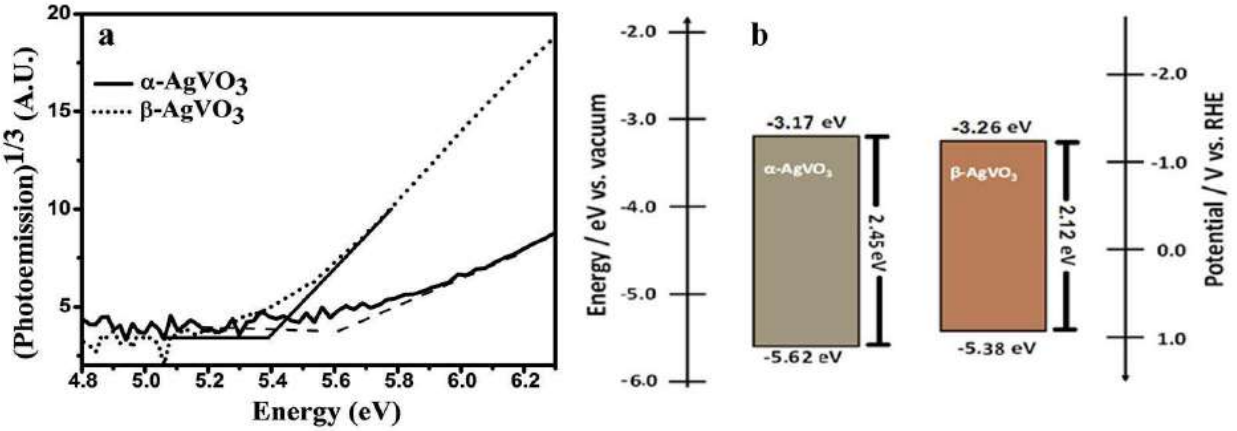

Figure 2-10. a) Ambient-pressure UV photoelectron spectroscopy (AP-UPS) data-derived plots for α-$AgVO_3$ and β-$AgVO_3$ and b) Surface energy band positions for the two polymorphs constructed from the AP-UPS and DRS data.

2.2.7. Electrochemical and Photoelectrochemical Behavior of α- and β-$AgVO_3$

Surface states are often exceedingly important in mediating charge transfer at the semiconductor-electrolyte interface.[42] The surface density of states (SDOS) can be accessed via the use of AP-UPS; these data for the two polymorphs (Figure 2-11) indicate that β-$AgVO_3$ has a higher SDOS relative to the α- polymorph. To explore the implications of this trend on the electrochemical charge transfer kinetics for the two samples, polarization experiments were conducted using a quasi-reversible redox couple, $Fe(CN)_6^{3-/4-}$. Figure 2-12 contains the data; for comparison, Pt and FTO electrodes were also included for these experiments. The insert in Figure 2-12 shows the data in Tafel plot (log *i* vs. *E*) format.[43]

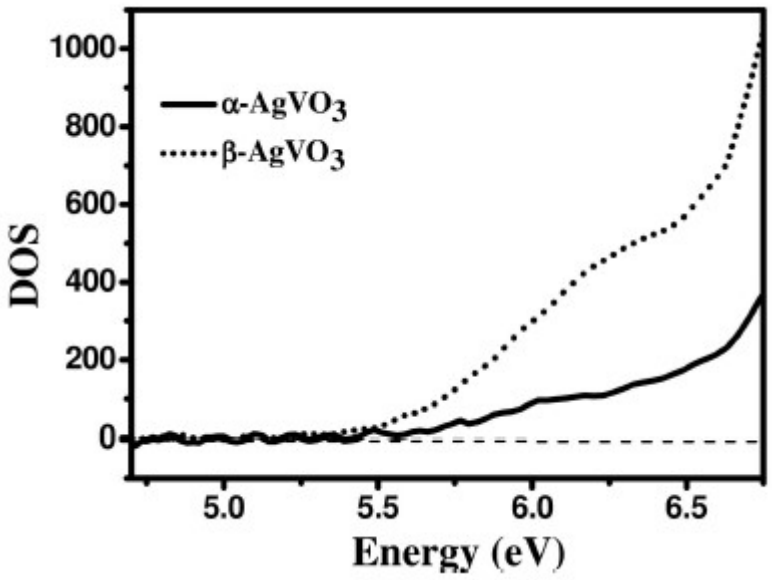

Figure 2-11. Ambient-pressure UV photoelectron spectroscopy (APUPS) data-derived plots for α- and β-$AgVO_3$.

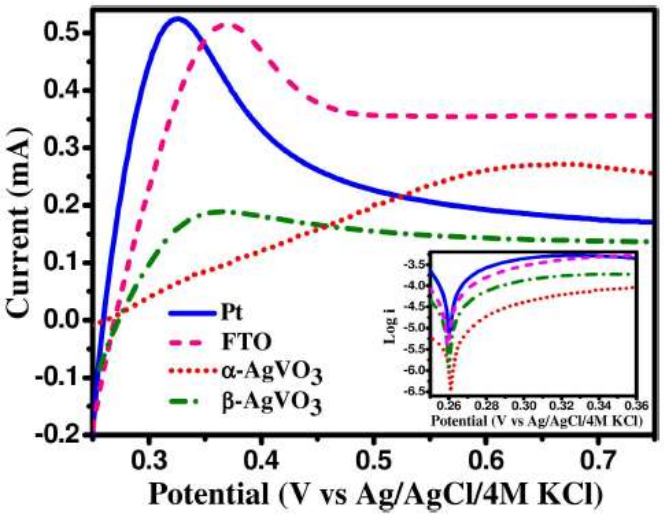

Figure 2-12. Forward-bias current-potential polarization curves in the dark for the oxidation of $Fe(CN)_6^{4-}$ redox species in 0.5 M KNO_3 supporting electrolyte. The insert contains these data in Tafel plot format. The standard redox potential, E^0, for the couple: $Fe(CN)_6^{3-} + e^- \rightarrow Fe(CN)_6^{4-}$ is +0.361 V vs. NHE (+0.164 V vs. Ag/AgCl).

The SDOS is a crucial factor in dictating the kinetics of charge transfer, both for metal and semiconductor electrodes.[43] In general, the SDOS follows the trend: metal > degenerately-doped

semiconductor > nominally-doped semiconductor. Consistent with this, the charge transfer kinetics, inferred from Figure 2-12 for the oxidation of $Fe(CN)_6^{4-}$ redox species are ordered thus: Pt > FTO > β-$AgVO_3$ > α-$AgVO_3$. Further, the trend for the two polymorphs is entirely in accordance with the SDOS data in Figure 2-11. It is worth noting in the experiments in Figure 2-12 that anodic polarization translates to the forward-bias regime for a *p*-type semiconductor such as $AgVO_3$. Note also, in this regard, that the DFT calculations presented earlier, placed the Fermi level close to the VBM in line with *p*-type conductivity behavior for the two polymorphs.

Electrochemical and photoelectrochemical stability plays a crucial role in dictating the practical applicability of a given semiconductor.[42] To probe the stability of the material in the dark, cyclic voltammetry experiments were performed. Figure 2-13 contains the data. In aqueous 0.2 M sodium

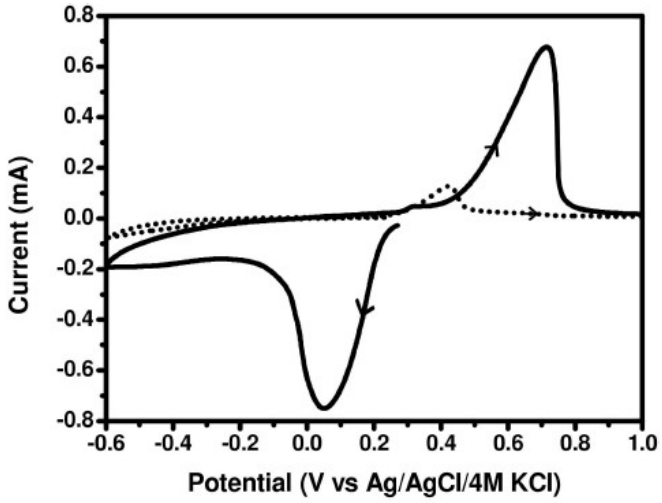

Figure 2-13. Cyclic voltammograms of as-prepared $AgVO_3$ film in 0.2 M sodium sulfate in water (—) and 0.2 M tetrabutylammonium perchlorate in acetonitrile (---), 5 mV/s potential scan rate.

sulfate, the as-prepared $AgVO_3$ shows a cathodic wave on scanning from the rest potential. An anodic wave is seen on the return scan. Comparison with the cyclic voltammetry data in Figure 2-3 immediately establishes these features to arise from the anodic generation of Ag^+ species leaching out of the film and their subsequent reduction on the return scan. On the other hand, these features

are greatly attenuated in the non-aqueous medium. The faint reduction wave on the return scan in the non-aqueous case can be attributed to residual traces of water in acetonitrile. The data in Figure 2-13 are consistent with the anodic corrosion reaction:

$$2AgVO_3 + H_2O + 2e^- \rightarrow 2Ag + V_2O_5 + 2OH^- \qquad E^0 = +0.07 \text{ V vs NHE} \qquad (2\text{-}5)$$

The standard potential for the above reaction was calculated from thermodynamic data in the literature on standard heats of formation.[35,44,45]

Having established that $AgVO_3$ has reasonable electrochemical stability in a non-aqueous electrolyte, photoelectrochemical experiments were conducted using dioxygen as an electron acceptor. Figure 2-14 contains the corresponding photovoltammetry[46] data for the two polymorphs.

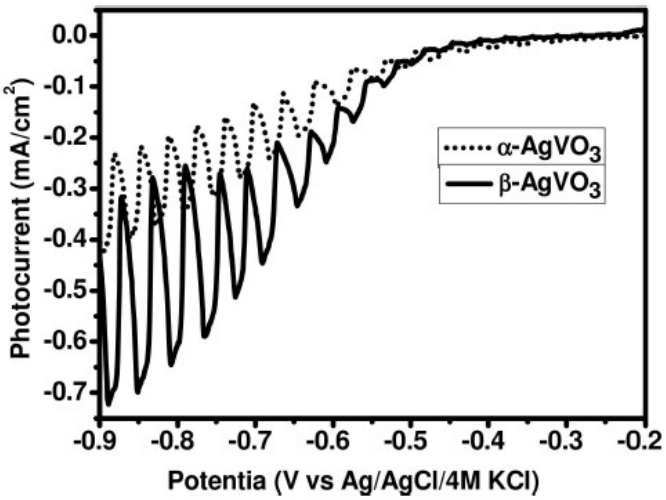

Figure 2-14. Linear sweep photovoltammograms for α-$AgVO_3$ (---) and β-$AgVO_3$ (—) in dioxygen- purged 0.2 M tetrabutylammonium perchlorate in acetonitrile, 1 mV/s potential scan rate.

In a photovoltammetry experiment, both the dark (electrochemical features) and the photocurrents are brought out in a single scan.[46] Note that the experiments are conducted in the *reverse-bias* regime unlike in the (forward-bias) experiments in Figure 2-13. Thus, the

photocurrents are induced by the minority carriers which are electrons for a *p*-type semiconductor.[42] Consistent with this notion, the photocurrent polarity is cathodic in the traces in Figure 2-14 in line with the *p*-type semiconductor behavior of $AgVO_3$ (see above). Note that there is significant dark current flow on increasing negative polarization for both the samples in Figure 2-14, suggesting that the semiconductor-electrolyte junctions in both the cases are "leaky". These currents are attributed to the reduction of (adventitious) dioxygen in the electrolyte.

The additional possibility that the dark currents arise from reduction of the oxide itself to silver (c.f., eq. 2-4) can be discounted based on the stability trends established in Figure 2-13. Clearly, the photoactivity of β-$AgVO_3$ is superior to that of α-$AgVO_3$; the photocurrents in the two cases are also reasonably high in the mA/cm^2 range. However, considerable improvement in the quality of the $AgVO_3$/electrolyte junctions is warranted before these candidates can be further considered for solar device applications.

2.3. CONCLUSIONS

In this study, motivated by the applicability of new-generation oxide semiconductors for solar cell applications, the synthesis and characterization of electrodeposited films of $AgVO_3$ in both aqueous and non-aqueous media, were described. Thermal anneal of the as-deposited α-$AgVO_3$ converted it to β-$AgVO_3$ and afforded comparison of the structural, optical, electronic, electrochemical, and photoelectrochemical attributes of the two polymorphs. From a theoretical perspective, it has been shown here, to the best of our knowledge for the first time, that the driver of the exothermic α → β $AgVO_3$ phase transformation is the structural relaxations due to a Peierls-like distortion and the tendency of V atoms to gain the stable +5 oxidation state via a Jahn-Teller like effect. Taken in whole, it is intriguing that a ternary oxide in two polymorphic forms that only differ in the relative juxtaposition of component AgO_x and VO_4 clusters,[16] can display such

diversity in optical, electronic, electrochemical, and photoelectrochemical properties. This aspect, of potential relevance to solar cell applications, deserves further scrutiny beyond the scope of the present study.

2.4. EXPERIMENTAL SECTION

2.4.1. Materials

Silver nitrate [$AgNO_3$ (Alfa Aesar)] and ammonium vanadate [NH_4VO_3 (Alfa Aesar)] were used as Ag and V source, respectively. Acetonitrile [CH_3CN (Sigma-Aldrich)] and double-distilled water (H_2O) were used as solvent. Tetrabutylammonium perchlorate [$(CH_3CH_2CH_3CH_2)_4N(ClO)_4$ (Alfa Aesar)] and potassium nitrate [KNO_3 (Alfa Aesar)] were used to prepare electrolyte solutions. Sodium dodecyl sulfate [$CH_3(CH_2)_{11}SO_4Na$ (Sigma-Aldrich)] was used as binder. Potassium ferricyanide [$K_3[Fe(CN)_6]$ (Sigma-Aldrich)] and Potassium ferrocyanide [$K_4[Fe(CN)_6]$ (Sigma-Aldrich)] were used as redox couple sources. All the chemicals were used as received without further purification.

2.4.2. Electrosynthesis of $AgVO_3$ Film

In the first step, a single compartment, three-electrode cell setup was used for the electrodeposition of silver thin film. An FTO substrate (Sigma-Aldrich, sheet resistance: ~7 Ω/sq) with 0.785 cm^2 area served as a working electrode. A platinum foil and Ag/AgCl/4M KCl electrode were used as the counterelectrode and quasi-reference electrode, respectively. The electrodeposition solution contained 20 mM $AgNO_3$, 0.2 mM sodium dodecyl sulfate (as a binder), and 200 mM tetrabutylammonium perchlorate (TBAP) as a supporting electrolyte in acetonitrile. Potentiodynamic film growth was used to control the thickness (nominally, 500 nm) of the silver thin film. The potential was swept 10 times from +0.15 to -0.80 V at 25 mV/s scan rate.

In the second step, the prepared silver thin film on FTO substrate served as the working electrode. A platinum foil and Ag/AgCl/4M KCl were again used as the counterelectrode and

reference electrode, respectively. The silver thin film was stripped anodically in ammonium metavanadate solution (40 mM) to generate Ag^+ and subsequent in situ precipitation with VO_3^- to yield $AgVO_3$ thin film on the substrate (Figure 2-2). The silver metavanadate thin film was prepared by sweeping the potential from 1.0 V to 1.20 V at 15 mV/s scan rate. The potentiodynamic sweeps were continued till no anodic current was observed from the residual oxidation of silver.

2.4.3. Electrochemical Quartz Crystal Microgravimetry (EQCM)

An EG&G Princeton Applied Research 263A instrument equipped with Power Suite electrochemistry software, a Seiko EG&G model QCA 922 instrument, and an oscillator module (QCA 922-10), was used. A single compartment, three-electrode cell setup was used for electrochemical experiments at room temperature and comprised of a 9 MHz AT-cut, Pt-coated quartz crystal (geometric area, 0.2 cm^2) working electrode, a Pt wire counterelectrode, and a Ag/AgCl/3M NaCl reference electrode.

2.4.4. Physical Characterization

A Siemens D-500 instrument with a Cu Kα radiation source (λ = 1.5406 Å) was used for X-ray diffraction (XRD) analysis of the prepared films. Scanning electron microscopy (SEM) and energy dispersive spectroscopy (EDS) were performed with a Hitachi S-3000N FE scanning electron microscope. The electron beam energy was 10 kV. The EDS data were collected from different spots of the prepared films and averaged. X-ray photoelectron spectroscopy (XPS) was performed on a Kratos Ultra DLD instrument. The source was Al K_α radiation at 1486.6 eV with 10.0 eV pass energy and 0.10 eV resolution. The reported binding energies were referenced against the C 1s photoelectron value of 284.6 eV.

Diffuse reflectance UV-Vis spectra were collected with an Avantes AvaSpec2048 instrument. An Avasphere-50 type integrating sphere was used with $BaSO_4$ as the reference. The reflectance data were converted to absorbance values via the Kubelka-Munk function: $\alpha/S = (1-R)^2/2R$, where α is the absorption coefficient, S is the scattering coefficient, and R is the reflectance.[39]

Measurements were recorded on a KP Technology APS04 Kelvin-probe instrument equipped with a 2 mm diameter gold alloy-coated tip.[47] The Fermi level (E_F) of the tip was determined by relative to a silver reference target ($E_{F,\ Au\ tip} = -4.61$ eV). The reference target was thoroughly polished with a 30 μm diamond paper. Ambient pressure UV photoelectron spectroscopy (APUPS) was carried out using a stationary Kelvin probe tip. The sample surface was illuminated with a 4–5 mm spot size, while the UV light source was swept in the range, λ = 180 – 340 nm using a monochromator.

2.4.5. Photoelectrochemistry

A single compartment, three-electrode cell setup and a CH Instruments potentiostat (Model CHI720C) were used for electrochemical measurements. The prepared films were supported on FTO substrate and the counterelectrode and reference electrode were the same as those described above. The electrochemical solution contained 0.2 M tetrabutylammonium perchlorate (TBAP) in acetonitrile and was purged by dioxygen (as an electron acceptor) during the photovoltammetry measurement. The potential was swept at 1 mV/s scan rate. Both the dark and illuminated periods were 15 s. A 400 W Xe lamp was used as a radiation source at a fixed distance (15 cm) from cell. The light intensity was measured by a Newport Model 70260 radiant power meter combined with a Model 70268 probe and was 300 mW/cm^2.

2.4.6. COMPUTATIONAL METHODOLOGY

The calculations were performed within the framework of spin polarized density functional theory (DFT)[48,49] as implemented in the Vienna ab initio simulation package (VASP).[50,51] The Perdew-Burke-Ernzerhof (PBE)[52] generalized gradient approximation (GGA) functional was used for exchange and correlation. The projector augmented plane wave (PAW) method[53] was used to describe the interactions between the core and valence electrons. VASP-supplied standard PAW potentials of Ag, V, and O were used for geometric optimization as well as for electronic structure calculations. The electronic basis set was expanded in terms of plane wave and kinetic energy cutoff of 600 eV throughout the calculation. For K point sampling within the first Brillouin zone, the Monkhorst-Pack (MP) scheme was deployed. The 4×4×7 and 2×9×4 k-point meshes were used for α and β-$AgVO_3$, respectively for geometric optimization which gave well-converged results.

During the geometrical optimization, the atoms in the unit cell were fully relaxed until the residual forces among the constituent atoms became less than 0.01 eV $Å^{-1}$. The Methfessel-Paxton smearing method with a width of 0.002 eV was used for geometric optimization. The tetrahedron method with Blöchl corrections were applied for density of states (DOS) calculations. Self-interactions of *d* electrons were corrected by providing an onsite Coulombic potential via the Hubbard U parameter. The rotationally invariant DFT+ U method[54] was used for calculations. The on-site Coulombic interaction term (U) and exchange interaction term (J) are the main determining factors to control the magnitude of the self-interaction correction within the DFT+U calculation framework.

It is very important to choose an appropriate value of U to correct the self-interaction error in DFT calculations. One way to choose the U value is to examine how it affects certain properties of interest, i.e., lattice constants, band gap, formation energy etc., and to use these results as a

guideline for further parameterization. In this study, we chose lattice constants and band gap as our properties of interest and select U value accordingly. The selected effective U (U_{eff} = U -J) values were 4.0 eV and 3.1 eV for Ag and V d-electrons, respectively. The J value was 1.0 eV throughout the calculation. The calculated lattice constants as well as band gap using these chosen values of U have proximity with the reported experimental values (See Table A-S1 and Table 2-1). Finally, the VESTA[55] software was used to visualize and analyze the crystal structure and band-decomposed charge density.

2.5. REFERENCES

(1) M. T. Galante, P. Sotelo, M. K. Hossain, A. Vali, A. Raamann, C. Longo, R. T. Macaluso, K. Rajeshwar, *ChemElectroChem.* **2018**, *5*, 1-11.

(2) A. P. de Melo Monteiro, R. D. Holtz, L. C. Fonseca, C. H. Z. Martins, M. de Souza, L. A. V. de Luna, D. L. de Sousa Maia, O. L. Alves, *Chem. Rec.* **2018**, *18*, 1-14.

(3) R. Konta, H. Kato, H. Kobayashi, A. Kudo, *Phys. Chem. Chem. Phys*. **2003**, *5*, 3061–3065.

(4) S. Zhang, W. Li, C. Li, J. Chen, *J. Phys. Chem. B.* **2006**, *110*, 24855-24863.

(5) S-J. Bao, Q-L. Bao, C-M. Li, T. P. Chen, C-Q. Sun, Z-L. Dong, Y. Gan, J. Zhang, *Small,* **2007**, *3*, 1174-1177.

(6) J-M. Song, Y-Z. Lin, H-B. Yao, F-J. Fan, X-G. Li, S-H. Yu, *ACS Nano,* **2009**, *3*, 653-660.

(7) G-T. Pan, M-H. Lai, R-C. Juang, T-W. Chung, T.C.-K. Yang, *I & EC Res*. **2011**, *50*, 2807-2814.

(8) P. Ju, H. Fan, B. Zhang, K. Shang, T. Liu, S. Ai, D. Zhang, *Sep. Purif. Technol.* 2013, *109*, 107-110.

(9) C. Belver, C. Adán, S. G. Rodríguez, M. F. García, *Chem. Eng. J.* 2013, *224*, 24-31.

(10) A. Singh, D. P. Dutta, A. Ballal, A. K. Tyagi, M. H. Fulekar, *Mater. Res. Bull*. **2014**, *51*, 447-454.

(11) W. Zhao, F. Liang, Z-M. Jin, X-B. Shi, P-H. Yin, X-R. Wang, C. Sun, Z-Q. Gao, L-S. Liao, *J. Mater. Chem*, **2014**, *2*, 13226-13231.

(12) H. Shi, C. Zhou, C. Zhang, *Res. Chem. Intermed*, **2015**, *41*, 7725–7737.

(13) W. Zhao, Y. Guo, Y. Faiz, W-T. Yuan, C. Sun, S-M. Wang, Y-H. Deng, Y. Zhuang, Y. Li, X-M. Wang, H. He, S-G. Yang, *Appl. Catal. B: Environ*. **2015**, *163*, 288-297.

(14) R. C. de Oliveira, M. Assis, M. M. Teixera, M. D. P. da Silva, M. S. Li, J. Andres, L. Gracia, E. Longo, *J. Phys. Chem. C* **2016**, *120*, 12254-12264.

(15) A. Beltran, L. Gracia, J. Andres, E. Longo, *J. Phys. Chem*, **2017**, *121*, 27624−27642.

(16) R. C. Oliveira, M. M. Teixera, J. P. C. Costa, M. Penha, E. M. Francisco, J. S. da Silva, M. S. Li, E. Longo, L. Gracia, J. Andres, *Ceram. Int*. **2018**, *44*, 5939-5944.

(17) K. Rajeshwar, *Adv. Mater*. **1992**, *4*, 23-29.

(18) T. E. Schlesinger, K. Rajeshwar, N. R. de Tacconi, in *Modern Electroplating* (Edited by M. Schlesinger), Chapter 14, pp. 383-411, Springer, New York, 2010.

(19) K. Rajeshwar, N. R. de Tacconi, C. R. Chenthamarakshan, *Chem. Mater*. **2001**, *13*, 2765-2782.

(20) C. Janaky, K. Rajeshwar, *Prog. Poly. Sci.* **2015**, *43*, 96-135.

(21) C. Janaky, E. Kescenovity, K. Rajeshwar, *ChemElectroChem* **2016**, *3*, 181-192.

(22) D. Kang, T.W. Kim, S. R. Kubota, A. C. Cardiel, H. G. Cha, K-S. Choi, *Chem. Rev*. **2015**, *115*, 12839-12887.

(23) G. V. Govindaraju, G. P. Wheeler, D. Lee, K-S. Choi, *Chem. Mater*. **2017**, *29*, 355-370.

(24) N. Myung, S. Ham, B. Choi, N. R. de Tacconi, K. Rajeshwar, *J. Electroanal. Chem.* **2005**, *574*, 367-373.

(25) S. Ham, B. Choi, N. Myung, N. R. de Tacconi, C. R. Chenthamarakshan, K. Rajeshwar, Y. Son, *J. Electroanal. Chem*. **2007**, *601*, 77-82.

(26) L. H. Dall 'Antonia, N. R. de Tacconi, W. Chanmanee, H. Timmaji, N. Myung, K. Rajeshwar, *Solid-State Lett.* **2010**, *13*, D29-D32.

(27) N. Myung, S. Ham, S. Choi, Y. Chae, W-G. Kim, Y. J. Jeon, K. J. Paeng, W. Chanmanee, N. R. de Tacconi, K. Rajeshwar, *J. Phys. Chem. C.* **2011**, *115*, 7793-7800.

(28) H-W. Jee, K-J. Paeng, N. Myung, K. Rajeshwar, *J. Electrochem. Soc.* **2017**, *165*, D1-D5.

(29) J. Scragg, P. Dale, L. Peter, G. Zoppi, L. Forbes, *Phys. Staus Solidi B* **2013**, *245*, 1772-1778.

(30) L. H. Mendoza-Huizar, J. Robles, M. Palomar-Pardave, *J. Electroanal. Chem*, **2002**, *521,* 95–106.

(31) R. Greef, R. Peat, L. M. Peter, D. Pletcher, J. Robinson, *Instrumental Methods in Electrochemistry*, Chapter 6, pp. 210-211, Ellis Horwood, Chichester, 2001.

(32) S. Ham, S. Jeon, M. Park, S. Choi, K-J. Paeng, N. Myung, K. Rajeshwar, *J. Electroanal. Chem.* **2010**, *638*, 195-203.

(33) M. R. Deakin, D. A. Buttry, *Anal. Chem*. **1989,** *61*, 1147A-1154A.

(34) D. A. Buttry in Electroanalyitcal Chemistry (Edited by A. J. Bard), Vol. 17, Marcel Dekker, New York, 1991.

(35) H. T. S. Briton, R. A. Robinson, *J. Chem. Soc. London*, **1930**, 2328–2343.

(36) S. Kittaka, Y. Yata, K. Matsuno, *J. Solid-State Chem*. **1999**, *142*, 360 – 367.

(37) P. Rozier, J-M. Savariault, J. Galy, *J. Solid-State Chem.* **1996**, *122*, 303 – 308.

(38) G. B. Hoflund, Z. F. Hazos, G. N. Salaita, *Phys. Rev. B*, **2000**, *62*, 11126-1133.

(39) A. Y. S. Malkhasian, *J. Alloys Compds,* **2015**, *649*, 394-399.

(40) A. B. Murphy, *Sol. Energy Mater Sol. Cells.* **2007**, *91*, 1326-1337.

(41) M. Sun, R. A. Senthil, J. Pan, S. Osman, A. Khan, *Catalysts,* **2018**, *8*, 392, 1-17.

(42) K. Rajeshwar, in *Encyclopedia of Electrochemistry* (Edited by S. Licht), Chapter 1, pp. 3-53, Wiley-VCH, Weinheim, 2001.

(43) A. J. Bard, L. R. Faulkner, *Electrochemical Methods. Fundamentals and Applications.* 2th ed., Chapter 3, pp. 103 and 125, Second Edition, John Wiley & Sons, 2001.

(44) *Lange's Handbook of Chemistry*, 11th ed. Chapter 9, pp. 4-128, McGraw-Hill, New York, 1978.

(45) *CRC Handbook*, 84th ed. Chapter 3, pp. 85-86, CRC Press, Boca Ratón, Florida, 2003.

(46) K. K. Mishra, K. Rajeshwar, *J. Electroanal. Chem*. **1989**, *273*, 169-182.

(47) I. D. Baikie, A. C. Grain, J. Sutherland, J. Law, *Appl. Surf. Sci.* **2014**, *323*, 45–53.

(48) P. Hohenberg, W. Kohn, *Phys. Rev.,* **1964**, *136*, B864-871.

(49) W. Kohn, L. J. Sham, *Phys. Rev.* **1965**, *140*, A1133-1138.

(50) G. Kresse, J. Furthmüller, *Comput. Mater. Sci.* **1996**, *6*, 15-50.

(51) G. Kresse, J. Furthmüller, *Phys. Rev. B.* **1996**, *54*, 11169-11186.

(52) J. P. Perdew, K. Burke, M. Ernzerhof, *Phys. Rev. Lett.* **1996**, *77*, 3865-3868.

(53) P. E. Blöchl, *Phys. Rev. B.* **1994**, *50*, 17953-17979.

(54) S. L. Dudarev, G. A. Botton, S. Y. Savrasov, C. J. Humphreys, A. P. Sutton, *Phys. Rev,* **1998**, *B 57*, 1505-1509.

(55) K. Momma, F. J. Izumi, *Appl. Crystallogr,* **2008**, *41*, 653-658.

CHAPTER 3

ELECTROCHEMICAL DEPOSITION OF CRYSTALLINE AND PHASE PURE SILVER ORTHOVANADATE

Used with permission from A. Vali, H-W Jee, P. Toth, F. Firouzan, C. Janáky, N. Myung, K. Rajeshwar, *J. Phys. Chem. C* **2020**, *124*, 19980−19989.

 https://doi.org/10.1021/acs.jpcc.0c05421

ABSTRACT:

Interest in silver-based semiconductors dates to the early years of analog photography. On the other hand, the recent discovery of new silver oxide-based ternary semiconductors has caused a resurgence of interest in these compounds for new technologies. In this vein, the present study provides a counter example to the two perennial issues confronting the electrosynthesis of compound semiconductor films, namely, those of crystallinity and phase purity. It is shown here, for the first time, that a two-step electrosynthesis strategy yields crystalline and phase pure α-Ag_3VO_4 films on transparent, conductive oxide substrates under very mild process (ambient temperature and pressure) and time-efficient (minutes synthesis duration) conditions. A complementary suite of experimental methods and thermodynamics/kinetics analyses facilitated a deep understanding of the electrosynthesis mechanism, optoelectronic behavior, semiconductor band structure, thermal and electrochemical stability, and electrochemical/photoelectrochemical attributes.

3.1. INTRODUCTION

Silver oxide-based semiconductors are attractive for a variety of important technological applications.[1] Therefore, much recent fundamental and practical interest has focused on ternary silver vanadates generated from the two binary oxide components, namely, Ag_2O and V_2O_5. These vanadates exhibit a fascinating range of Ag_2O:V_2O_5 stoichiometries (1:7, 1:2, 1:1, 2:1, 3:1; see Figure 1 in Ref. 2). In particular, Ag_3VO_4 with the highest ratio of Ag_2O: V_2O_5 (3:1) has attracted considerable interest.[3-8] Further, attesting to the practical importance of this material, a variety of heterojunctions and composites derived from Ag_3VO_4 have been deployed for solar energy conversion and photocatalytic remediation of environmental pollutants.[9-27] Other potential applications in the sensor and bactericidal/virucidal areas portend a bright future for this material.

Silver orthovanadate (Ag_3VO_4) exhibits up to three different polymorphs, namely, α, β, and γ phases.[28,29] The α-phase (α-Ag_3VO_4) is the stable form at room temperature.[28,29] α-Ag_3VO_4 is converted to *β*-Ag_3VO_4 reversibly at 110 ºC.[29] The famatinite-phase (*β*-Ag_3VO_4) was stable in the temperature range, 110-414 °C, while γ-Ag_3VO_4 was stable in the temperature range, 414-530 °C.[29] α-Ag_3VO_4 has a monoclinic structure with space group C2/c, while β-Ag_3VO_4 has a tetragonal famatinite (Cu_3SbS_4-type) structure with $I\bar{4}2m$ space group.[29] The γ-form adopts a cubic structure with space group $F\bar{4}3m$ and has been rarely studied.[29] However, the crystal structure aspects of the α- and β-polymorphs are well described in the literature.[28,29]

Semiconductor type (whether *n*- or *p*-type), optical band gap, band edge positions, quantum efficiency, or chemical/electrochemical/photoelectrochemical stability are all crucial factors in many technological applications such as those identified above. Barring a theoretical study[28] on the semiconductor behavior of *α*-Ag_3VO_4, based on first-principles electronic structure

calculations, that predicted *p*-type behavior for α-Ag_3VO_4, very little exists on the above factors in the relevant literature. This gap prompted the present study.

Silver orthvanadate has been synthesized using a variety of methods including hydrothermal (most common), solid state (ceramic), precipitation, successive ionic layer adsorption and reaction (SILAR), combinatorial sputtering, anodic oxidation, or pulsed laser deposition.[1-8,30] Conspicuous by its absence is the use of electrodeposition[31-35] for Ag_3VO_4 film synthesis. Given the versatility and recent popularity of electrosynthetic procedures in general,[31-35] this omission is rather surprising.

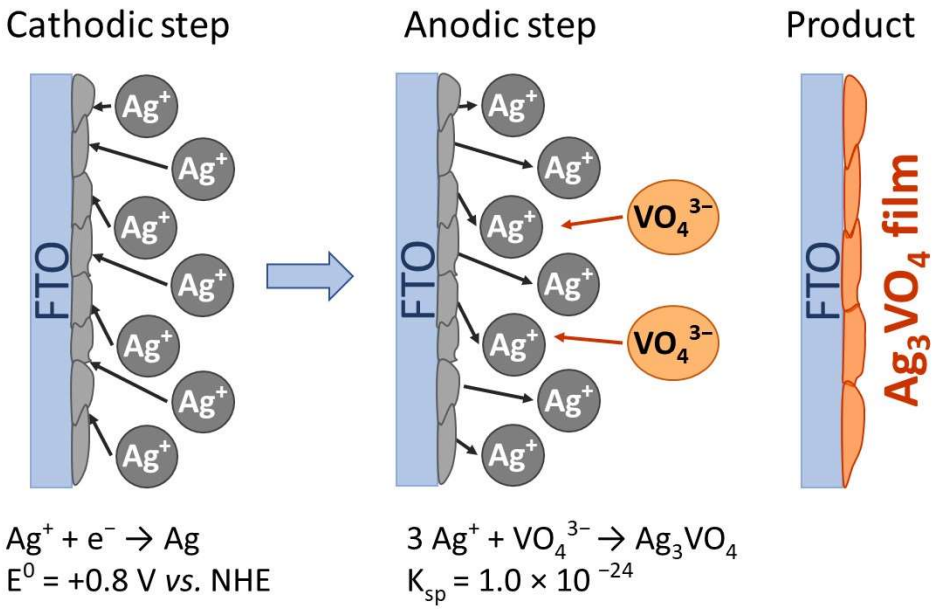

Scheme 1. Two-step electrosynthesis of Ag_3VO_4.

This paper therefore describes the application of a two-step, hybrid cathodic-anodic approach (Scheme 1) for the electrodeposition of α-Ag_3VO_4 films on transparent, conducting oxide glass (fluorine-doped tin oxide or FTO) substrates. A companion study from our group[2] on the 1:1 Ag_2O-V_2O_5 ternary compound, namely $AgVO_3$, recently appeared and overlapping aspects are

identified below. By judicious variation of the electrodeposition medium pH in the second step and considering Pourbaix-type[36] speciation of the vanadium species, the product could be routed to the targeted α- Ag_3VO_4 phase instead of the $AgVO_3$ composition studied earlier. We believe this to be one of the many innovative aspects of this study, which is the first report on Ag_3VO_4 electrosynthesis.

3.2. EXPERIMENTAL SECTION

3.2.1. Materials.

Silver nitrate [$AgNO_3$ (Alfa Aesar)] and sodium orthovanadate [Na_3VO_4 (Alfa Aesar)] were used as Ag and V source, respectively, for the electrodeposition bath. Acetonitrile [CH_3CN (Sigma-Aldrich)] and double-distilled water (H_2O) were used as the solvent to make up the various electrolytes used in this study. Other chemicals were as detailed in Ref. 2. All the chemicals were used as received without further purification.

3.2.2. Electrosynthesis of α-Ag_3VO_4 Film.

The substrate supporting the film was FTO (c.f., Scheme 1) (details of FTO in Ref. 2) in all the experiments discussed below. Potentiodynamic film growth was used in the first step and the potential was swept 10 times from +0.15 to -0.80 V at 25 mV/s scan rate and 20 s resting time between cycles. Other procedural details associated with the first step were given in Ref. 2. In the second step, the prepared silver thin film on the FTO substrate served as the working electrode. The silver thin film was stripped anodically in sodium orthovanadate solution (40 mM) to generate Ag^+ and instigate subsequent in situ deposition (Scheme 1). An alkaline medium (pH: 12.2) enabled speciation of V as VO_4^{3-}, this step is further elaborated below.

3.2.3. Physical and Electrochemical/Photoelectrochemical Characterization.

Instrumentation for voltammetry, photoelectrochemistry experiments, electrochemical quartz crystal microgravimetry (EQCM), X-ray diffraction (XRD), energy-dispersive X-ray analysis (EDX), diffuse reflectance spectroscopy (DRS), surface photovoltage spectroscopy (SPS) and ambient pressure UV photoelectron spectroscopy (APUPS) is detailed elsewhere.[2, 37-41]

The morphology of the electrodeposited Ag_3VO_4 samples was investigated by using scanning electron microscopy (SEM) with an APREO C SEM microscope (ThermoFisher Scientific), operating at 10 kV. Particle size histogram analyses were performed on a pool of 300 particles from the SEM images using ImageJ software. Transmission electron microscopy (TEM) was performed on a FEI Tecnai G^2 20 X-Twin microscope, operating at an acceleration voltage of 200 kV. Samples for TEM were prepared by scratching the as-deposited Ag_3VO_4 layer from the FTO substrate and subsequently dispersing the nanoparticles in ethanol. This suspension was drop cast onto a carbon coated copper grid (Electron Microscopy Sciences). Fast Fourier transform (FFT) images from different area of the TEM images were obtained using ImageJ software. Laser Raman spectra of samples were acquired on a Senterra II Compact Raman microscope (Bruker), using an excitation line of 532 nm (2.33 eV) with a 50× objective and an incident power, ≤ 2.5 mW. Peaks were fitted with Lorentzian shape functions.

3.3. RESULTS AND DISCUSSION

3.3.1. Mechanistic Insights into the Two-Step Electrodeposition of *α*-Ag_3VO_4.

Mechanistic details of cathodic Ag thin film growth on the FTO substrate (Scheme 1) were given elsewhere[2] and need not be repeated here. In the second anodic step (Scheme 1), this silver film was stripped anodically to generate Ag^+ (Reaction 3-1) in an aqueous solution of sodium orthovanadate (pH: 12.2 via base hydrolysis). Subsequent in situ precipitation of these ions with

VO_4^{3-}, driven by the low solubility product for Ag_3VO_4 (K_{sp} = 1.0 x 10^{-24})[42] yielded a brownish yellow Ag_3VO_4 film on the substrate (Reaction 3-2).

$$Ag_{(s)} \rightarrow Ag^{+}_{(aq)} + e^{-} \qquad E^0 = +0.800V \text{ vs NHE} \qquad (3\text{-}1)$$

$$3Ag^{+}_{(aq)} + VO_4^{3-}{}_{(aq)} \rightarrow Ag_3VO_{4(s)} \qquad K_{sp} = 1.0 \times 10^{-24} \qquad (3\text{-}2)$$

Figure 3-1a contains a linear sweep voltammogram (solid line) and the corresponding EQCM frequency change (dotted line) during anodic stripping. The frequency decrease along the oxidation wave domain is diagnostic of mass gain and the electrodeposition of a film (presumably Ag_3VO_4) on the Pt-coated quartz surface. Further insight into the deposition mechanism can be gleaned by combining the EQCM and coulometric data for the oxidation:[43-45]

$$Q = -\left(\frac{nFk}{M}\right)\Delta f \qquad (3\text{-}3)$$

Q is the charge consumed, F is the Faraday constant, Δf is the frequency change, k is the Sauerbrey constant,[43-45] and M is the molar mass of the deposit. By constructing a Q versus $-\Delta f$ "Sauerbrey plot" (Figure 3-1b), one can calculate the electron stoichiometry, n from the slope. The calculated n value from the least-squares fitted slope was 3.05, very close to the value expected from the following reaction:

$$3Ag_{(s)} + VO_4^{3-}{}_{(aq)} \rightarrow Ag_3VO_{4(s)} + 3e^{-} \qquad E^0 = -0.326V \text{ vs NHE} \qquad (3\text{-}4)$$

The slight lag in the mass gain or frequency change onset relative to the current flow onset in Figure 3-1a is reminiscent of the trend seen earlier for $AgVO_3$ and signals the fact that deposition and nucleation/ of Ag_3VO_4 is also a slow process. Figure B-S1 shows a photograph of the color change associated with the silver → silver orthovanadate conversion.

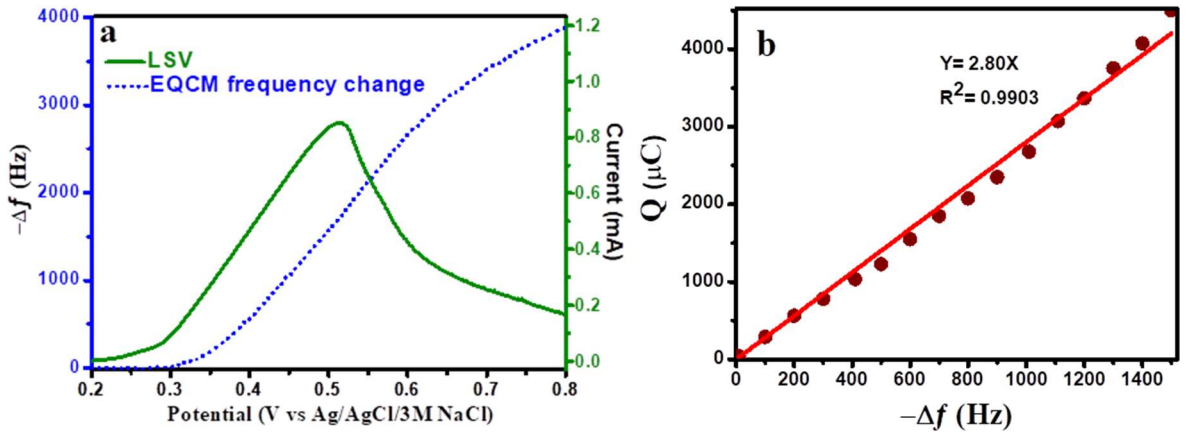

Figure 3-1. (a) Linear sweep voltammmogram (—) and the corresponding EQCM frequency change (....) for the electrodeposition of silver orthovanadate at 20 mV/s potential scan rate. (b) A Sauerbrey plot derived from the EQCM-voltammetry data.

A high pH aqueous medium (pH: 12.2) is needed for the anodic stripping step to provide the dominant VO_4^{3-} species needed for subsequent Ag_3VO_4 film growth. For example, in the pH range, 9-12, $V_2O_7^{4-}$ species and in the pH range from 6 to 9, VO_3^- species will be dominant.[46] However, meriting scrutiny is the possible formation of silver hydroxide (AgOH) as a side-product because of the preponderance of OH^- in high pH media (15.9 mM OH^- at pH: 12.2) by in situ precipitation of Ag^+ with OH^- (Reaction 3-5). Nonetheless, the EQCM results presented above and the physical characterizations (discussed in the next section) are consistent with a phase pure Ag_3VO_4 film from electrodeposition.

Thermodynamics and kinetics provide the answer to the dichotomy of possible AgOH formation. When Ag^+ is produced during anodic stripping, in situ precipitation of Ag^+ with OH^- (Reaction 3-5) and subsequent reaction (Reaction 3-6) can produce Ag_2O.:

$$Ag^+_{(aq)} + OH^-_{(aq)} \rightarrow AgOH_{(s)} \qquad K_{sp} = 2.0 \times 10^{-8} \qquad (3\text{-}5)$$

$$2AgOH_{(s)} \rightarrow Ag_2O_{(s)} + H_2O_{(l)} \qquad \Delta G^0 = -21.98 \text{ kJ/mol} \qquad (3\text{-}6)$$

The sum of Reactions, 3-1, 3-5, and 3-6 produces the Ag_2O formation reaction as:

$$2Ag_{(s)} + 2OH^-_{(aq)} \rightarrow Ag_2O_{(s)} + H_2O_{(l)} + 2e^- \quad E^0 = -0.343V \text{ vs NHE} \qquad (3\text{-}7)$$

When Ag^+ is produced during anodic stripping, both VO_4^{3-} and OH^- compete to capture the silver cation (Reaction 3-2 vs. Reaction 3-5). Because the solubility product constant (K_{sp}) of Ag_3VO_4 (1.0×10^{-24})[42] is significantly lower than AgOH (2.0×10^{-8})[47] and the concentration of VO_4^{3-} (40 mM) is higher than OH^- (15.9 mM, see above), the possibility of formation of Ag_3VO_4 will be significantly higher than that of Ag_2O. Our experimental results bear out these expectations.

3.3. 2.Physical Characterization of the Silver Orthovanadate Film.

Morphological examination of the as-prepared sample by SEM revealed film nucleation/growth in the form of roughly spherical nanoparticles, see Figure 3-2. The electrodeposited films had a mesoporous structure (Figure 3-2A), reflecting the formation of the semiconductor particles through precipitation in the second electrochemical step. The high-resolution image (Figure 3-2B) suggested a relatively broad size distribution of the as-prepared particles. Upon statistical analysis, the mean diameter of the particles was in the range, 90 to 110 nm, as deduced from the histogram presented in Figure B-S2.

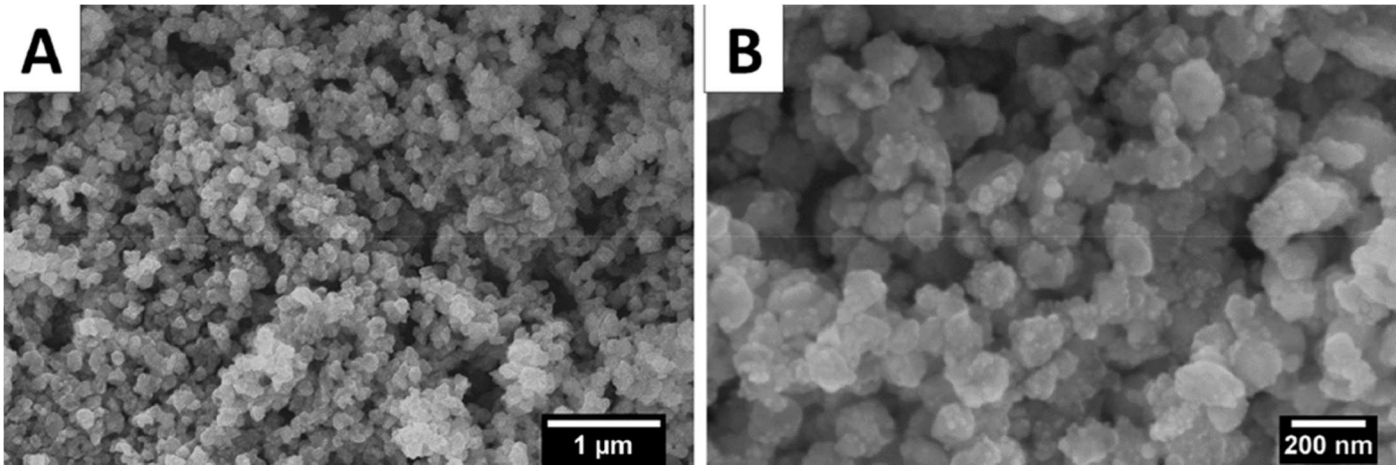

Figure 3-2. Representative scanning electron micrographs of an as-prepared silver orthovanadate film on FTO substrate at different magnifications. Representative top-view (A) and high resolution (B) images.

Elemental EDX maps (not shown) indicated uniform film composition across the entire FTO surface. Specifically, no regions rich in silver could be found, for example. Compositional EDX assays averaged from different spots of sample were consistent with the Ag/V ratio: 2.92 ± 0.02; a representative EDX trace is shown in Figure B-S3 in the Supporting Information.

Transmission electron microscopy (TEM) images (Figure B-S4A) complemented the SEM data in Figure 3-2 on the morphology of the as-deposited Ag_3VO_4 nanoparticles in the film being composed of raspberry-like structural domains. Selected area electron diffraction (SAED) pattern revealed the crystalline features (Figure B-S4B) to be poly- rather than single crystalline. A lattice resolved high-resolution TEM image (Figure 3-3A) and the corresponding fast Fourier transform

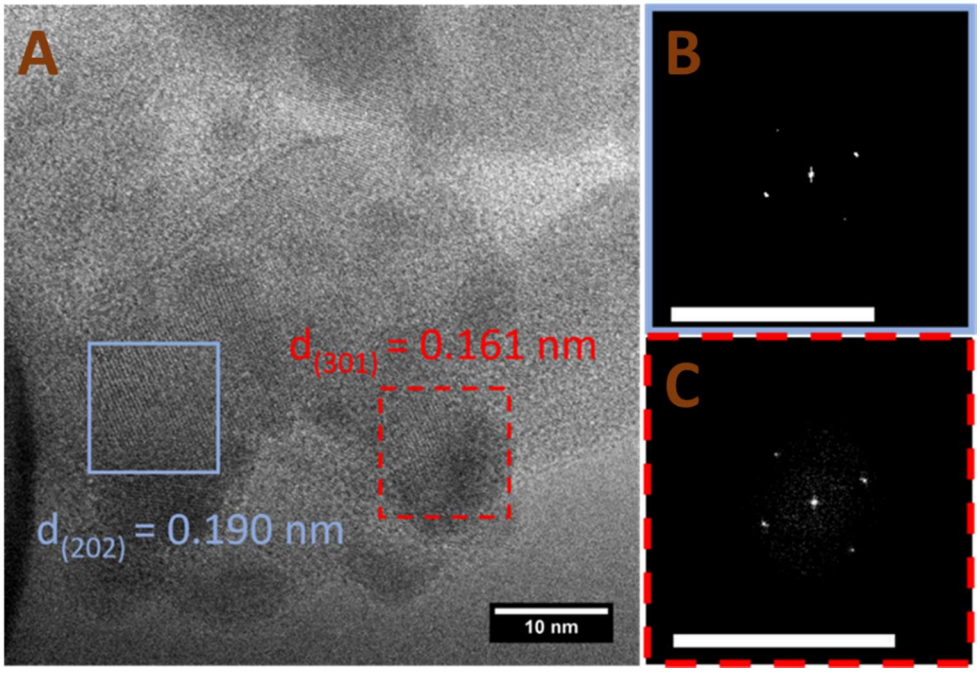

Figure 3-3. High resolution TEM (A) and FFT (B-C) images from different areas of the Ag_3VO_4 specimen. Different crystal planes are marked by red dashed (301) and blue solid (202) lines in A, respectively. Scale bars in B-C correspond to 5 nm^{-1}.

(FFT) patterns (Figure 3-3B-C) showed (301) and (202) crystal planes with 0.161 and 0.190 nm d-spacing, respectively.[48,49] These results underline that the electrodeposited Ag_3VO_4 was highly crystalline and had a monoclinic structure.

Significantly, XRD data on the as-prepared film (Figure 3-4) supported the TEM data in that the synthesized film was crystalline (***even without thermal anneal***) in phase pure α-Ag_3VO_4 form. In other words, the films were crystalline even though the electrodeposition was performed at room temperature. Non-optimal film morphology (amorphous nature) and contamination with side products are perennial Achilles heels of the electrosynthesis approach.[31,37-41] Clearly, the present study demonstrates that these handicaps are not always problematic and good crystallinity can be obtained even under mild process conditions.

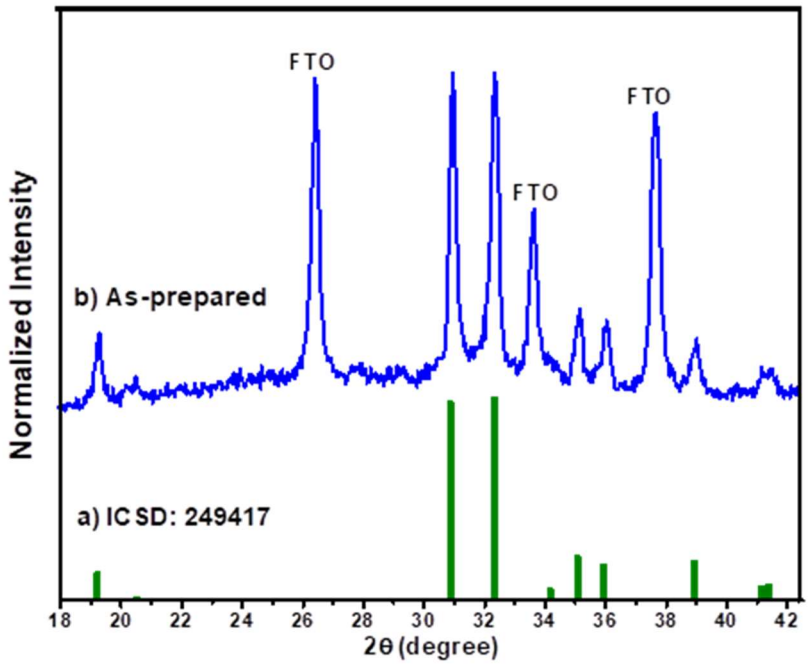

Figure 3-4. XRD patterns for (a) reference α-Ag_3VO_4 and (b) electrodeposited sample.

The as-prepared silver vanadate samples were analyzed by laser Raman spectroscopy to investigate the degree of structural order–disorder, as well as to confirm phase purity. Figure 3-5 shows laser Raman spectra of α-Ag_3VO_4 synthesized under optimal conditions, a $Ag_4V_2O_7$ containing specimen, and a Ag_xVO_y sample, corresponding to a non-stoichiometric composition.

Two B_{2g} Raman-active modes at 810 and 830 cm^{-1} correspond to the vibration of the distorted tetrahedral [VO_4] cluster, derived from the symmetric-stretching.[50] The Raman spectra of $Ag_4V_2O_7$ characterized by one single band at about 870 cm^{-1} typical of tetrahedral and 5-fold coordinated vanadates. Additionally, the active vibration bands at higher Raman shifts (around 900, and 950 cm^{-1})[51] correlate well with octahedrally coordinated vanadate species. These data further confirm our conclusions from the XRD data on the phase purity of the electrodeposited α-Ag_3VO_4 films.

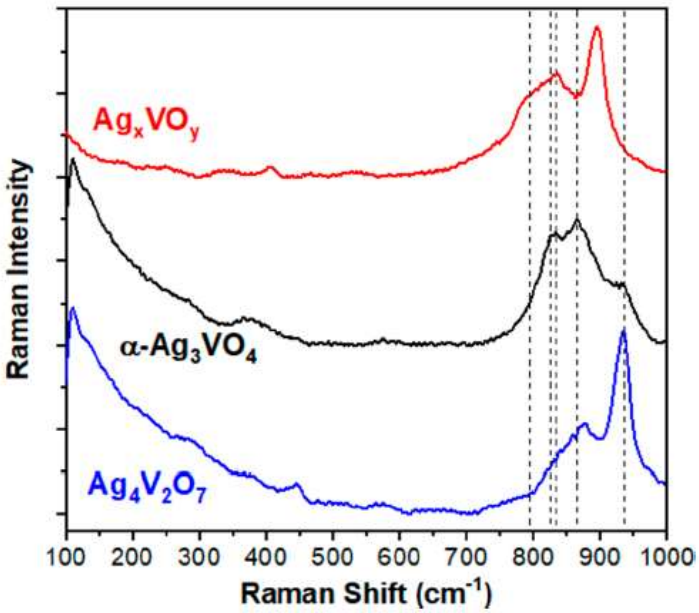

Figure 3-5. Laser Raman spectra of as-prepared silver vanadate samples (α-Ag_3VO_4, $Ag_4V_2O_7$, and Ag_xVO_y). The Raman-active modes are indicated by the dashed lines.

The as-prepared α-Ag_3VO_4 film was annealed at four different temperatures (150, 200, 250, and 300 °C) for 1 h to map the effect of anneal temperature on crystallinity and thermal stability of the as-prepared sample. The XRD results (Figure B-S5) showed that the crystalline phase of the as-prepared sample after anneal at 150 °C and 200 °C was not altered, and the film remained in the α-Ag_3VO_4 form. On the other hand, the XRD pattern of the annealed sample at 250 °C showed that the α-Ag_3VO_4 peaks had disappeared. Further increasing the anneal temperature to 300 °C

completely decomposed the α-Ag_3VO_4 film to $Ag_4V_2O_7$ and Ag (Figure B-S5). The morphological and elemental EDX maps of the annealed sample at 350 ºC (Figures B-S6 and B-S7) showed that uniform dispersed roughly spherical nanoparticles of as-prepared Ag_3VO_4 had transformed to roughly spherical microparicles and nanobars. The EDX elemental maps (Figures B-S8 and B-S9) showed that the roughly spherical microparticles were composed of pure silver. The nanobars were composed of $Ag_4V_2O_7$ with an Ag/V ratio: 1.92 ± 0.02.

Thermodynamic calculations for possible Ag_3VO_4 decomposition reactions (Reactions 3-8 to 3-12) showed that the decomposition of Ag_3VO_4 was endothermic in all the cases. However, the pathway forming $Ag_4V_2O_7$ and Ag (Reaction 3-8) had the lowest Gibbs free energy (ΔG^0), consistent with the above experimental observations.

$$Ag_3VO_4 \rightarrow \frac{1}{2}Ag_4V_2O_7 + Ag + \frac{1}{4}O_2 \qquad \Delta G^0 = +0.609 \text{ eV} \qquad (3\text{-}8)$$

$$Ag_3VO_4 \rightarrow AgVO_3 + 2Ag + \frac{1}{2}O_2 \qquad \Delta G^0 = +0.643 \text{ eV} \qquad (3\text{-}9)$$

$$Ag_3VO_4 \rightarrow \frac{3}{2}Ag_2O + \frac{1}{2}V_2O_5 \qquad \Delta G^0 = +0.808 \text{ eV} \qquad (3\text{-}10)$$

$$Ag_3VO_4 \rightarrow 3Ag + \frac{1}{2}V_2O_5 + \frac{3}{4}O_2 \qquad \Delta G^0 = +1.07 \text{ eV} \qquad (3\text{-}11)$$

$$Ag_3VO_4 \rightarrow 3Ag + V + 2O_2 \qquad \Delta G^0 = +8.39 \text{ eV} \qquad (3\text{-}12)$$

Standard Gibbs free energy data for the above reactions were culled from thermodynamic data compilations in the literature.[46,47]

3.3.3. Optical Behavior.

The UV/visible spectrum of an as-prepared sample (after transformation of the DRS data, Ref. 52) showed an absorption onset wavelength of ~575 nm (see Figure B-S10). Table 3-1 presents a comparison of this value with those reported in the literature for samples prepared using other synthesis methods. There is some scatter in the reported values due to the

Table 3-1. Absorption onset wavelength value for α-Ag_3VO_4 along with literature data

Absorption onset wavelength (nm)	575	567	580	560	615	560	613	560
Reference	This study	2	4	7	14	20	25	27

uncertainty in the estimation of the onset value from the spectral information (For example, note the presence of a "tail" in Figure B-S10.). This issue has been addressed by us and other authors elsewhere.[52,53] Nonetheless, a safe conclusion can be made that the onset wavelength cut-off for electrodeposited α-Ag_3VO_4 is in the range: 560-580 nm. (The two values of 613 nm and 615 nm from Refs. 25 and 14 are outliers.)

Tauc plots[51-53] were constructed from the UV/visible DRS data. Figures 3-6a and b contain these plots for direct and indirect optical transitions in the as-deposited α-Ag_3VO_4 sample; the corresponding energy band gaps were 2.58 ± 0.04 eV and 2.37 ± 0.02 eV, respectively. Table 3-2 presents a comparison of these values with those reported in the literature for samples derived from other synthesis methods. There is some scatter in the reported values of the energy band gaps (Table 3-2). Once again, this issue has been discussed by us and others elsewhere.[52,53]

Table 3-2. Energy bandgap values for α-Ag_3VO_4 (c.f., Figure 3-5) along with literature data.

Direct band gap (eV)	2.58 ± 0.04	2.58	2.37	2.05	2.10
Indirect band gap (eV)	2.37 ± 0.02	2.18	NR	NR	NR
Reference	This study	7	14	18	23

NR: Not reported

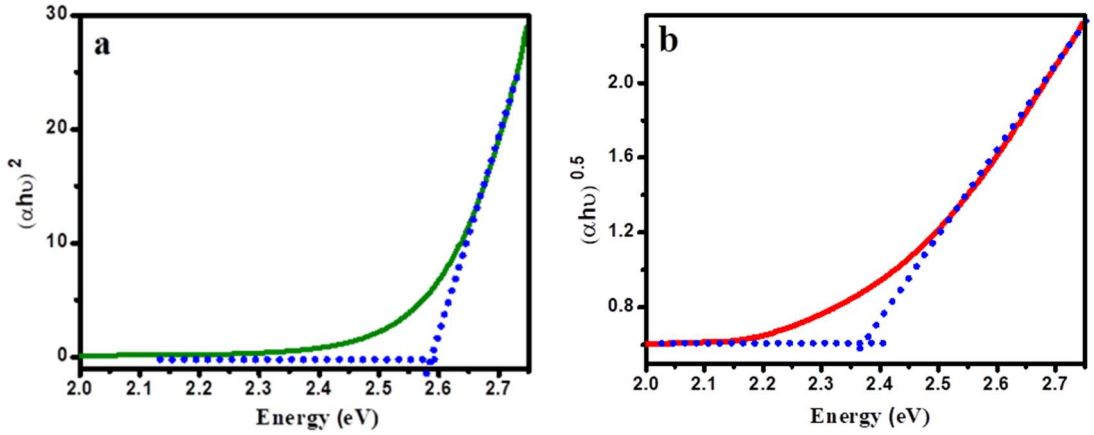

Figure 3-6. Tauc plots for α-Ag_3VO_4 film on FTO. Frames (a) and (b) contain the plots analyzed for direct and indirect optical transitions respectively.

3.3.4. Electronic Band Structure of α-Ag_3VO_4.

Ambient-pressure UV photoelectron spectroscopy (AP-UPS)[54] was used to map the valence band maximum (VBM) in α-Ag_3VO_4. Figure 3-7a contains the data; the VBM is located at the intercept of the plot. The value of VBM is -4.82 ± 0.03 eV on the vacuum energy scale. Surface photovoltage spectroscopy (SPS) was deployed to measure the (surface) band gap of as-prepared α-Ag_3VO_4. Figure 3-7b contains the data; from the intercept of

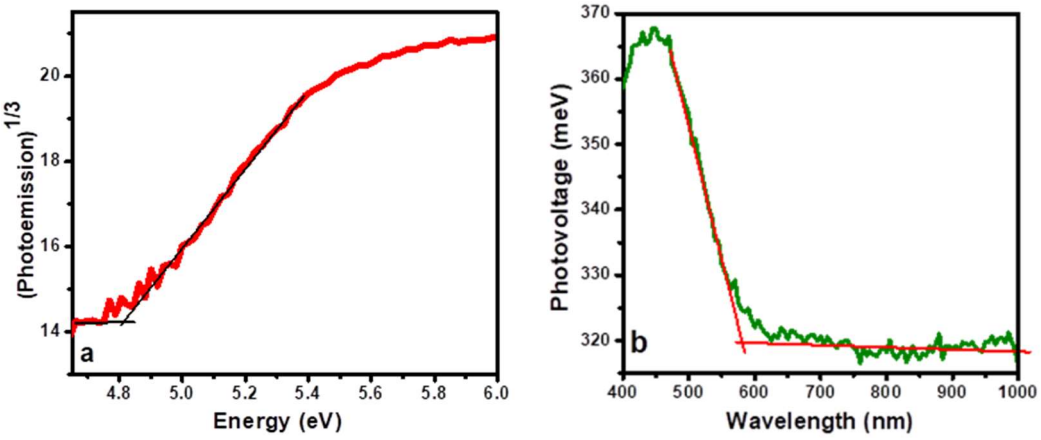

Figure 3-7. (a) Ambient-pressure UV photoelectron spectroscopy (AP-UPS) data-derived plot and (b) Surface photovoltage spectroscopy (SPS) data-derived plot for as-prepared α-Ag_3VO_4.

this spectrum, the band gap was measured as: 2.16 ± 0.03 eV. Note that the measured photovoltage onset wavelength (~620 nm) is higher than the measured absorbance onset wavelength (~575 nm, see above) by the DRS method. This difference possibly originates from the variant sensitivity of SPS and DRS to the surface properties. Specifically, sub-band gap energy levels become important on the semiconductor surface and SPS is more sensitive to the surface properties than DRS.[55] The net result is that the measured photovoltage onset wavelength (~620 nm) is higher than the absorption onset wavelength (~575 nm).

The positive photovoltage polarity at energies higher than band gap (Figure 3-7b) is diagnostic of *p*-type semiconductor behavior for α-Ag_3VO_4.[55] This is in good agreement with the theoretical results.[28] The Fermi level (E_F) of α-Ag_3VO_4 was measured by using Kelvin-probe spectroscopy. Figure B-S11 contains the resultant contact potential difference data; from these, the measured E_F value translates to -4.61 ± 0.01 eV on the vacuum energy scale. Using the obtained VBM, E_F, and the surface band gap values, the surface band structure of α-Ag_3VO_4 was constructed (Scheme 2). The purple dashed line in Scheme 2 shows that the Fermi level is located 0.21 eV above the valence

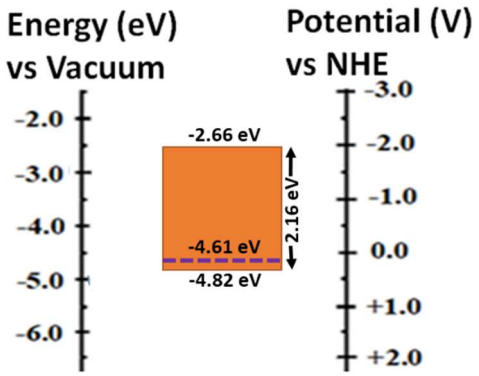

Scheme 2. Surface energy band positions for as-prepared α-Ag_3VO_4 constructed from AP-UPS, Kelvin probe microscopy, and SPS data. Purple dashed line shows the Fermi level position.

band, as expected for moderately doped *p-type* semiconductors. The valence band position is not favorable for water photooxidation since it lies above the thermodynamic threshold value of +1.23

V (vs. NHE). On the other hand, the conduction band minimum (CBM) is thermodynamically favorable for hydrogen evolution (HER) and oxygen reduction reactions. Significantly, the CBM lies at considerable overpotentials above the HER threshold of 0 V (vs. NHE).

3.3.5. Electrochemical and Photoelectrochemical (PEC) Behavior of α-Ag_3VO_4. Many practical applications of α-Ag_3VO_4 would demand knowledge of the charge transfer efficacy of its surface. This can be done using a quasi-reversible redox probe. Therefore, dark, polarization experiments were conducted using the probe redox couple, $Fe(CN)_6^{3-/4-}$. Figure 3-8a contains the data; for comparison, Pt and FTO electrodes were also included in these experiments. The results show that the valence band holes (majority carriers) in the *p*-Ag_3VO_4 semiconductor electrode oxidized $Fe(CN)_6^{4-}$ species on application of positive overpotentials (forward bias regime). The *anodic* polarity of the dark current flow in the forward bias regime also diagnoses the film to behave as a *p-type* semiconductor[55] in conformity with the discussion earlier on this aspect.

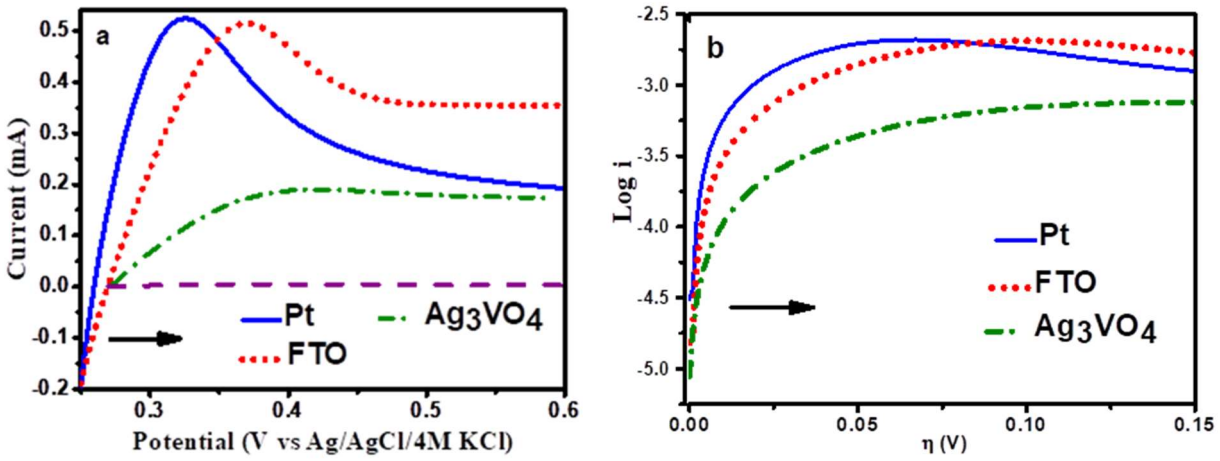

Figure 3-8. (a) Forward-bias current-potential polarization curves in the dark for the oxidation of $Fe(CN)_6^{4-}$ species in 50 mM $K_4Fe(CN)_6$, 50 mM $K_3Fe(CN)_6$, and 0.5 M KNO_3. Purple dashed line shows anodic polarization of Ag_3VO_4 in 0.5 M KNO_3 without redox species. (b) Tafel plots constructed from anodic polarization data.

The kinetics of majority carrier charge transfer in the dark can be assessed by converting the polarization curve (i vs. E) to a Tafel plot (log i vs. E).[56] Such Tafel plots for Pt, FTO, and Ag_3VO_4 are shown in Figure 3-8b (log i vs η). Figures 3-8a and b show that Pt, FTO, and Ag_3VO_4 reached the mass transfer limited peaks or plateau for overpotentials (η) less than 118 mV. Therefore, Tafel analyses were not optimal for these three electrodes under the present experimental conditions. In addition, no clear linear behavior was observed in the kinetically controlled charge transfer regime at higher overpotentials (Figure 3-8b). Therefore, instead of the Tafel plot, an alternative equation proposed by other authors (Equation 3-13)[56,57] was deployed:

$$log\left(\frac{i}{e^{f\eta}-1}\right) = log\, i_0 - \frac{\alpha F}{2.3\,RT}\eta \qquad (3\text{-}13)$$

$$i_0 = FAk^oC^* \qquad (3\text{-}14)$$

In Equations 3-13 and 3-14, $f = F/RT$, i_0 is the exchange current, k^o is the standard heterogeneous rate constant, A is the electrode area, C^* is the redox concentration, and the symbols R and T have their usual significance.

The constructed plots for the three electrodes using Equation 3-13 and the polarization data are shown in Figure 3-9 for Pt, FTO, and Ag_3VO_4 respectively. Unlike the Tafel plots in Figure 3-8b, these plots were considerably more linear and the i_0 parameter could be extracted easily from the intercept of the linear part of the plot for overpotentials in the range from 10 mV to 40 mV (see dashed vertical lines in Figure 3-9). The corresponding k^o value could be calculated using Equation 3-14. The calculated standard rate constant (k^o in cm/s) for Pt, FTO, and Ag_3VO_4 were 3.44×10^{-4}, 1.72×10^{-4}, and 5.84×10^{-5} respectively. This trend in relative charge transfer efficacy can be rationalized based on surface density of states (SDOS) arguments.[56]

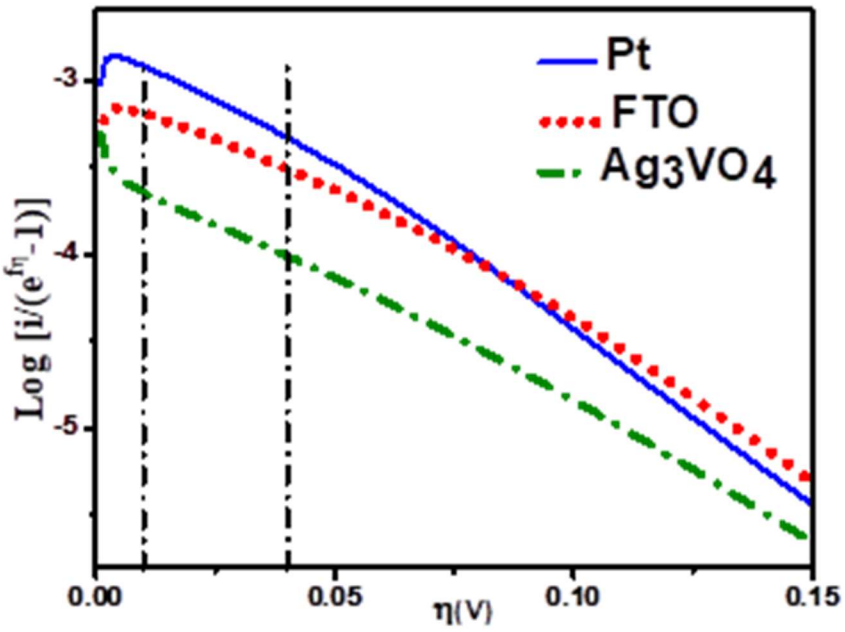

Figure 3-9. Log $\left[\frac{i}{e^{f\eta}-1}\right]$ *vs.*η plots from anodic polarization data.

The surface density of states (SDOS) is a crucial factor in dictating the kinetics of charge transfer, both for metal and semiconductor electrodes.[56] In general, the SDOS follows the trend: metal > degenerately doped semiconductor > nominally doped semiconductor. Thus, in the present case, Pt is a metal, FTO a degenerately doped semiconductor, and α-Ag_3VO_4 is a nominally doped semiconductor. Consistent with this, the above derived standard rate constants for the oxidation of $Fe(CN)_6^{4-}$ redox species were ordered thus: Pt > FTO > α-Ag_3VO_4. This order is entirely consistent with the corresponding SDOS trend.

To probe the electrochemical stability of α-Ag_3VO_4 in the dark (again, an important prerequisite for many practical device applications), cyclic voltammetry experiments were performed in aqueous and non-aqueous solutions; Figure 3-10a contains the data. In aqueous 0.2 M sodium sulfate, the as-prepared α-Ag_3VO_4 electrode showed a cathodic wave on scanning negatively from the open circuit potential; an anodic wave was seen on the return scan.

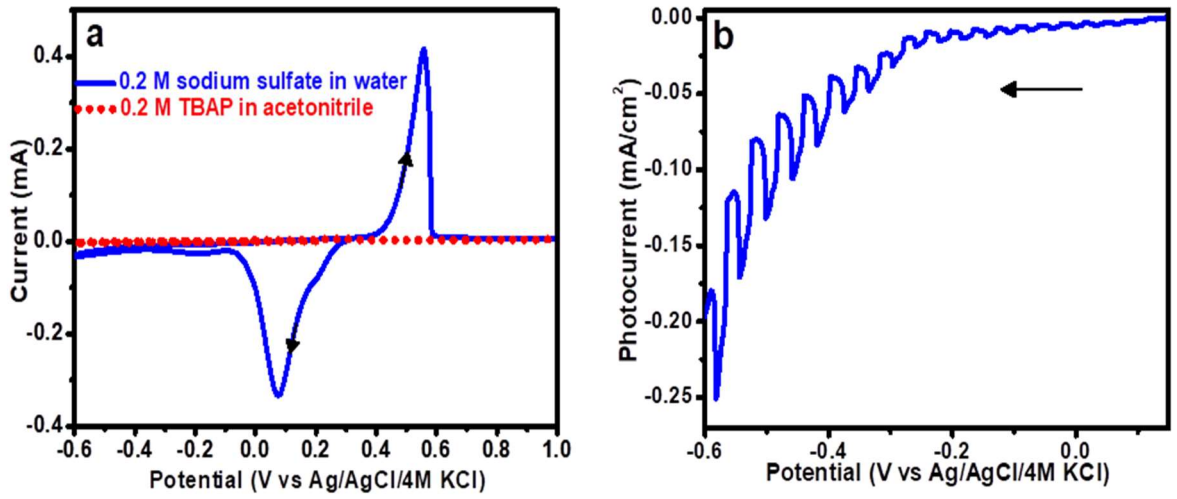

Figure 3-10. (a) Cyclic voltammograms of as-prepared Ag_3VO_4 film in 0.2 M sodium sulfate in water (—) and 0.2 M tetrabutylammonium perchlorate in acetonitrile (---), 5 mV/s potential scan rate. (b) Linear sweep photovoltammogram for α-Ag_3VO_4 in dioxygen-purged 0.2 M tetrabutylammonium perchlorate in acetonitrile, 1 mV/s potential scan rate.

These reduction and oxidation waves were not observed in the non-aqueous medium. The cathodic wave in aqueous electrolyte is diagnostic of (cathodic) corrosion of α-Ag_3VO_4 in the presence of water.

Therefore, an as-prepared α-Ag_3VO_4 sample was electrochemically reduced in aqueous medium to probe the elemental composition and crystalline structure of the product on the film surface after cathodic corrosion. Figures B-S12 and B-S13 contain the results of EDX and XRD analyses respectively after cathodic corrosion; these confirm the presence of elemental silver on the film surface. Therefore, the anodic wave in Figure 3-10a may be assigned to oxidative stripping of silver and generation of Ag^+ species. The cathodic corrosion reaction is given as follows:

$$Ag_3VO_{4(s)} + H_2O_{(l)} + 3e^- \rightarrow 3Ag_{(s)} + VO_3^-{}_{(aq)} + 2OH^-_{(aq)} \quad E^0 = +0.195 \text{ V vs NHE} \qquad (3\text{-}15)$$

The standard potential for the above reaction was calculated from thermodynamic data culled from the literature on standard Gibbs free energies of formation.[46,47]

Given the electrochemical stability of α-Ag_3VO_4 in a non-aqueous electrolyte (Figure 3-10a), photoelectrochemical (PEC) experiments were conducted using dioxygen as an electron acceptor in a non-aqueous electrolyte. Figure 3-10b contains the corresponding photovoltammetry[55] data for as-prepared α-Ag_3VO_4. In a photovoltammetry experiment, both the dark current (electrochemical features) and the photocurrents are generated in a single scan.[55] Note that these experiments were conducted in the *reverse-bias* regime unlike in the (forward-bias) kinetics experiments in Figure 3-8a. Thus, the photocurrents are generated by minority carriers which are electrons for a *p*-type semiconductor.[55] Consistent with this notion, the photocurrent polarity is cathodic in the traces in Figure 3-10b in line with the *p*-type semiconductor behavior of α-Ag_3VO_4 (see above).

Unfortunately, there was significant dark current flow on applying negative overpotentials in Figure 3-10b, suggesting that the α-Ag_3VO_4 film-electrolyte junction was "leaky". The dark current is attributed to the reduction of (adventitious) dioxygen in the electrolyte. A parallel possibility is that the residual traces of water in acetonitrile could participate in the corrosion reaction (Reaction 3-15) ***under photoirradiation but not in the dark*** in the experimental potential window. The PEC reduction reaction (photocorrosion counterpart of Reaction 3-15) presumably occurs at less negative overpotentials than those required to drive this reaction on a pure conductive electrode.[55] This notion is entirely reasonable within the PEC conceptual framework.[55]

While the above data demonstrate that α-Ag_3VO_4 has good stability in the dark in an optimized (non-aqueous) electrolyte, considerable improvement in the quality of the Ag_3VO_4/electrolyte junction would be needed under irradiation even in the same electrolyte (see below). These data

point the need for further studies on the possible use of this *p-type* semiconductor for practical device applications.

3.4. CONCLUSIONS

This first report on α-Ag_3VO_4 underlines the immense potential of electrosynthesis as a film preparation strategy that is environmentally benign, time-efficient, and scalable. Crystalline, phase pure and stoichiometric α-Ag_3VO_4 films could be obtained even without post-deposition thermal anneal. The present data acquired from a wide array of experimental techniques and thermodynamics/kinetics analyses showed that practical applicability in electrochemical/photoelectrochemical scenarios would require further optimization of junction quality to suppress minority carrier flow ***in the dark***. Approaches revolving around chemical modification of an electrodeposited α-Ag_3VO_4 film surface and/or multi-layered electrodeposited configurations could prove to be profitable avenues worthy of further pursuit. The many multilayered examples involving α-Ag_3VO_4 as one component in previous studies (using other synthesis approaches)[9-27] indeed bolster this notion.

3.5. REFERENCES

(1) Galante, M. T.; Sotelo, P.; Hossain, M. K.; Vali, A.; Raamann, A.; Longo, C.; Macaluso, R. T.; Rajeshwar, K. Silver Oxide-Based Semiconductors for Solar Fuels Production and Environmental Remediation: A Solid-State Chemistry Approach. *ChemElectroChem* **2019**, *6*, 87–96.

(2) Vali, A.; Sarker, H. P.; Jee, H-W.; Kormányos, A.; Firouzan, F.; Myung, N.; Paeng, K-J.; Huda, M. N.; Janáky, C.; Rajeshwar, K. Electrodeposition of Silver Vanadate Films: A Tale of Two Polymorphs. *ChemPhysChem* **2019**, *20,* 2635–2646.

(3) Huang, C-M.; Pan, G-T.; Li, Y-C. M.; Li, M-H.; Yang, T. C-K. Crystalline Phases and Photocatalytic Activities of Hydrothermal Synthesis Ag_3VO_4 and $Ag_4V_2O_7$ under Visible Light Irradiation. *Appl. Catal. A* **2009**, *358*, 164–172.

(4) Hu, X.; Hu, C. Preparation and Visible-Light Photocatalytic Activity of Ag_3VO_4 Powders. *J. Solid State Chem.* **2007**, *180*, 725–732.

(5) Belver, C.; Adán, C.; Rodríguez, S. G.; García, M. F. Photocatalytic Behavior of Silver Vanadates: Microemulsion Synthesis and Post-Reaction Characterization. *Chem. Eng. J.* **2013**, *224*, 24–31.

(6) Huang, C-M.; Cheng, K-W.; Pan, G-T.; Chang, W-S.; Yang, T. C-K. CTAB-Assisted Hydrothermal Synthesis of Silver Vanadates and Their Photocatalytic Characterization. *Chem. Eng. Sci.* **2010**, *65*, 148–152.

(7) Chemelewski, W. D.; Mabayoje, O.; Mullins, C. B. SILAR Growth of Ag_3VO_4 and Characterization for Photoelectrochemical Water Oxidation. *J. Phys. Chem. C* **2015**, *119*, 26803–26808.

(8) Pan, G-T.; Lai, M-H.; Juang, R-C.; Chung, T-W.; Yang, T. C-K. Preparation of Visible-Light-Driven Silver Vanadates by a Microwave-Assisted Hydrothermal Method for the Photodegradation of Volatile Organic Vapors. *Ind. Eng. Chem. Res.* **2011**, *50*, 2807–2814.

(9) Wang, G.; Ren, Y.; Zhou, G. J.; Wang, J. P.; Cheng, H. F.; Wang, Z. Y.; Zhan, J.; Huang, B. B.; Jiang, M. H. Synthesis of Highly Efficient Visible Light $Ag@Ag_3VO_4$ Plasmonic Photocatalysts. *Surf. Coat. Technol*. **2013**, *228*, S283–S286.

(10) Zhang, J.; Ma, Z. Flower-Like Ag_3VO_4/BiOBr n-p Heterojunction Photocatalysts with Enhanced Visible-Light-Driven Catalytic Activity. *Mol. Catal*. **2017**, *436*, 190–198.

(11) Rana, R.; Meng, X.; Zhang, Z. Facile Preparation of Novel Graphene Oxide-Modified $Ag_2O/Ag_3VO_4/AgVO_3$ Composites with High Photocatalytic Activities under Visible Light Irradiation. *Appl. Catal. B* **2016**, *196*, 1–15.

(12) Golzad-Nonakaran, B.; Habibi-Yangjeh, A. Photosensitization of ZnO with Ag_3VO_4 and AgI Nanoparticles: Novel Ternary Visible-Light-Driven Photocatalysts with Highly Enhanced Activity. *Adv. Powder Tech.* **2016**, *27*, 1427–1437.

(13) Zhang, J.; Ma, Z. Ag_3VO_4/AgI Composites for Photocatalytic Degradation of Dyes and Tetracycline Hydrochloride under Visible Light. *Mater. Lett.* **2018**, *216*, 216–219.

(14) Gao, L.; Li, Z.; Liu, J. Facile Synthesis of Ag_3VO_4/β-$AgVO_3$ Nanowires with Efficient Visible-Light Photocatalytic Activity. *RSC Adv.* **2017**, *7*, 27515–27521.

(15) Jonjana, S.; Phuruangrat, A.; Thongtem, S.; Wiranwetchayan, O.; Thongtem, T. Preparation and Characterization of Ag_3VO_4/Bi_2MoO_6 Nanocomposites with Highly Visible-Light-Induced Photocatalytic Properties. *Mater. Lett.* **2016**, *180*, 93–96.

(16) Nualkaew, P.; Phuruangrat, A.; Dumrongrojthanath, P.; Thongtem, S.; Thongtem, T. Synthesis of Ag_3VO_4 Nanoparticles Loaded on Bi_2MoO_6 Nanoplates as Heterostructure Visible

Light Driven Photocatalyst by Sonochemical Method. *J. Ceram. Soc. Jpn*. **2016**, *124*, 1157–1160.

(17) Wang, P.; Tang, H.; Ao, Y.; Wang, C.; Hou, J.; Qian, J.; Li, Y. In-Situ Growth of Ag_3VO_4 Nanoparticles onto BiOCl Nanosheet to Form a Heterojunction Photocatalyst with Enhanced Performance under Visible Light Irradiation. *J. Alloys Compd.* **2016**, *688*, 1–7.

(18) Zhang, L.; He, Y.; Ye, P.; Qin, W.; Wu, Y.; Wu, T. Enhanced Photodegradation Activity of Rhodamine B by Co_3O_4/Ag_3VO_4 under Visible Light Irradiation. *Mater. Sci. Eng. B* **2013**, *178*, 45–52.

(19) Zhang, L.; He, Y.; Ye, P.; Wu, Y.; Wu, T. Enhanced Photodegradation Activity of Rhodamine B by $MgFe_2O_4/Ag_3VO_4$ under Visible Light Irradiation. *Catal. Commun.* **2013**, *30*, 14–18.

(20) Wang, J.; Ruan, H.; Li, W.; Li, D.; Hu, Y.; Chen, J.; Shao, Y.; Zheng, Y. Highly Efficient Oxidation of Gaseous Benzene on Novel Ag_3VO_4/TiO_2 Nanocomposite Photocatalysts under Visible and Simulated Solar Light Irradiation. *J. Phys. Chem. C* **2012**, *116*, 13935–13943.

(21) Yan, M.; Wu, Y.; Zhu, F.; Hua, Y.; Shi, W. The Fabrication of a Novel Ag_3VO_4/WO_3 Heterojunction with Enhanced Visible Light Efficiency in the Photocatalytic Degradation of TC. *Phys. Chem. Chem. Phys.* **2016**, *18*, 3308–3315.

(22) Zhang, L.; He, Y.; Ye, P.; Wu, Y.; Wu, T. Visible Light Photocatalytic Activities of $ZnFe_2O_4$ Loaded by Ag_3VO_4 Heterojunction Composites. *J. Alloys Compd.* **2013**, *549*, 105–113.

(23) Kiantazh, F.; Habibi-Yangjeh, A. Ag_3VO_4/ZnO Nanocomposites with an n–n Heterojunction as Novel Visible-Light-Driven Photocatalysts with Highly Enhanced Activity. *Mater. Sci. Semicon. Proc.* **2015**, *39*, 671–679.

(24) Xie, Y.; Dai, Y.; Yuan, X.; Jiang, L.; Zhou, L.; Wu, Z.; Zhang, J.; Wang, H.; Xiong, T. Insight on the Plasmonic Z-Scheme Mechanism Underlying the Highly Efficient Photocatalytic Activity of Silver Molybdate/Silver Vanadate Composite in Rhodamine B Degradation. *J. Colloid. Interf. Sci*. **2018**, *530*, 493–504.

(25) Ren, C.; Fan, J.; Liu, S.; Li, W.; Wang, F.; Li, H.; Liu, X.; Chang, Z. One-Step Hydrothermal Synthesis of Novel Ag_3VO_4/ $Ag_4V_2O_7$ Composites for Enhancing Visible-Light Photocatalytic Performance. *RSC Adv*. **2016**, *6*, 95156–95164.

(26) Yan, M.; Wu, Y.; Yan, Y.; Yan, X.; Zhu, F.; Hua, Y.; Shi, W. Synthesis and Characterization of Novel $BiVO_4/Ag_3VO_4$ Heterojunction with Enhanced Visible-Light-Driven Photocatalytic Degradation of Dyes. *ACS Sustainable Chem. Eng*. **2016**, *4,* 757–766.

(27) Padervand, M. Visible-Light Photoactive Ag–AgBr/α-Ag_3VO_4 Nanostructures Prepared in a Water-Soluble Ionic Liquid for Degradation of Wastewater. *Appl. Nanosci*. **2016**, *6*, 1119–1126.

(28) Trimarchi, G.; Peng, H.; Im, J.; Freeman, A. J.; Cloet, V.; Raw, A.; Poeppelmeier, K. R.; Biswas, K.; Lany, S.; Zunger, A. Using Design Principles to Systematically Plan the Synthesis of

Hole-Conducting Transparent Oxides: Cu_3VO_4 and Ag_3VO_4 as a Case Study. *Phys. Rev. B* **2011**, *84*, 165116, 1–14.

(29) Cloet, V.; Raw, A.; Poeppelmeier, K. R.; Trimarchi, G.; Peng, H.; Im, J.; Freeman, A. J.; Perry, N. H.; Mason, T. O.; Zakutayev, A.; Ndione, P. F.; Ginley, D. S.; Perkins, J. D. Structural, Optical, and Transport Properties of α- and β-Ag_3VO_4. *Chem. Mater*. **2012**, *24*, 3346−3354.

(30) Hirono, T.; Yamada, T.; Nishi, T. Photochromic Silver Complex Oxide Thin Films Synthesized by Anodic Oxidation. *J. Appl. Phys*. **1986**, *59*, 948–950.

(31) Rajeshwar, K. Electrosynthesized Thin Films of Group II-VI Compound Semiconductors, Alloys and Superstructures. *Adv. Mater*. **1992**, *4*, 23–29.

(32) Schlesinger, T. E.; Rajeshwar, K.; de Tacconi, N. R. Electrodeposition of Semiconductors. In *Modern Electroplating*; Schlesinger, M., Paunovic, M., Eds.; Springer: New York, 2010; Chapter 14, pp 383–411.

(33) Rajeshwar, K.; de Tacconi, N. R.; Chenthamarakshan, C. R. Semiconductor-Based Composites: Preparation, Properties, and Performance. *Chem. Mater*. **2001**, *13*, 2765–2782.

(34) Janáky, C.; Rajeshwar, K. The Role of (Photo)Electrochemistry in the Rational Design of Hybrid Conducting Polymer/Semiconductor Assemblies: From Fundamental Concepts to Practical Applications. *Prog. Poly. Sci.* **2015**, *43*, 96–135.

(35) Janáky, C.; Kescenovity, E.; Rajeshwar, K. Electrodeposition of Inorganic Oxide/Nanocarbon Composites: Opportunities and Challenges. *ChemElectroChem* **2016**, *3*, 181–192.

(36) For example: Pourbaix, M. *Atlas of Electrochemical Equilibria in Aqueous Solutions* (translated from the French by Franklin, J. A.); Pergamon Press: New York, 1974.

(37) Myung, N.; Ham, S.; Choi, B.; de Tacconi, N. R.; Rajeshwar, K. Electrosynthesis of Cadmium Sulfide on Sulfur or Thiol-Modified Polycrystalline Gold Electrode. *J. Electroanal. Chem.* **2005**, *574*, 367–373.

(38) Ham, S.; Choi, B.; Myung, N.; de Tacconi, N. R.; Chenthamarakshan, C. R.; Rajeshwar, K.; Son, Y. Electrodeposition of CdTe Thin Films on Te-Modified Polycrystalline Gold Substrates. *J. Electroanal. Chem*. **2007**, *601*, 77–82.

(39) Myung, N.; Ham, S.; Choi, S.; Chae, Y.; Kim, W-G.; Jeon, Y. J.; Paeng, K-J.; Chanmanee, W.; de Tacconi, N. R.; Rajeshwar, K. Tailoring Interfaces for Electrochemical Synthesis of Semiconductor Films: $BiVO_4$, Bi_2O_3, or Composites. *J. Phys. Chem. C* **2011**, *115*, 7793–7800.

(40) Jee, H-W.; Paeng, K-J.; Myung, N.; Rajeshwar, K. Electrodeposition of Cobalt Selenide Thin Films: An Electrochemical Quartz Crystal Microgravimetry Study. *J. Electrochem. Soc.* **2017**, *165*, D1–D5.

(41) Jee, H-W.; Paeng, K-J.; Myung, N.; Rajeshwar, K. Electrochemical Deposition of Metal-Organic Framework and Subsequent Conversion to Cobalt Selenide. *ACS Appl. Electronic Mater.* **2020**, *2*, 1358-1364.

(42) Briton, H. T. S.; Robinson, R. A. Physicochemical Studies of Complex Acids. Part IV. The Vanadates of Silver. *J. Chem. Soc.* **1930**, *0*, 2328–2343.

(43) Ham, S.; Jeon, S.; Park, M.; Choi, S.; Paeng, K-J.; Myung, N.; Rajeshwar, K. Electrodeposition and Stripping Analysis of Bismuth Selenide Thin Films Using Combined Electrochemical Quartz Crystal Microgravimetry and Stripping Voltammetry. *J. Electroanal. Chem.* **2010**, *638*, 195–203.

(44) Deakin, M. R.; Buttry, D. A. Electrochemical Applications of the Quartz Crystal Microbalance. *Anal. Chem*. **1989,** *61*, 1147A–1154A.

(45) Buttry, D. A. Applications of the Quartz Crystal Microbalance to Electrochemistry. In *Electroanalyitcal Chemistry: A Series of Advances;* Bard, A. J., Ed.; Marcel Dekker: New York, 1991; Vol. 17.

(46) Baes, C. F.; Messmer, R. E. *The Hydrolysis of Cations*; John Wiley & Sons: New York, 1976; Chapter 10, pp 197–210.

(47) Zhutaeva, G. V.; Shumilova, N. A.; Israel, Y. Silver and Vanadium. In *Standard Potentials in Aqueous Solution;* Bard, A. J., Parsons, R., Jordan, J., Eds.; Marcel Dekker: New York, 1985; Chapter 11, pp 295–296, Chapter 17, pp 508–513.

(48) Zheng, J.; Calvillo, L.; Valero-Vidal, C.; Marega, C.; Sekar, P.; Shuang, S.; Girardi, L.; Agnoli, S.; Rizzi, G. A.; Granozzi., G. Ag-Vanadates/GO Nanocomposites by Aerosol-Assisted Spray Pyrolysis: Preparation and Structural and Electrochemical Characterization of a Versatile Material. *ACS Omega* **2017**, *2*, 2792−2802.

(49) de Oliveira, R. C.; Gracia, L.; Assis, M.; Siu Li, M.; Andres, J.; Longo, E.; Cavalcante, L. S. Disclosing the Electronic Structure and Optical Properties of $Ag_4V_2O_7$ Crystals: Experimental and Theoretical Insights. CrystEngComm **2016**, *18*, 6483–6491.

(50) Zhang, J.; Ma, Z. Ag_3VO_4/$BiOIO_3$ Heterojunction with Enhanced Visible-Light-Driven Catalytic Activity. *J. Taiwan Inst. Chem. E.* **2018**, *88*, 177–185.

(51) Murphy, A. B. Band-Gap Determination from Diffuse Reflectance Measurements of Semiconductor Films, and Application to Photoelectrochemical Water-Splitting. *Sol. Energy Mater Sol. Cells* **2007**, *91*, 1326–1337.

(52) Roy, D.; Samu, G.; Hossain, M.; Janáky, C.; Rajeshwar, K. On the Measured Optical Bandgap Values of Inorganic Oxide Semiconductors for Solar Fuels Generation. *Catal. Today* **2018**, *300*, 136-144.

(53) Viezbicke, B. D.; Patel, S.; Davis, B.E.; Birnie, D. P. Evaluation of the Tauc Method for Optical Absorption Edge Determination: ZnO Thin Films as a Model System. *Phys. Status Solidi B* **2015**, *252*, 1700-1710.

(54) Baikie, I. D.; Grain, A. C.; Sutherland, J.; Law, J. Ambient Pressure Photoemission Spectroscopy of Metal Surfaces. *Appl. Surf. Sci.* **2014**, *323*, 45–53.

(55) Rajeshwar, K. Semiconductor Electrodes and Photoelectrochemistry. In *Encyclopedia of Electrochemistry;* Licht, S., Ed.; Wiley-VCH: Weinheim, 2001; Chapter 1, pp 3–53.

(56) Bard, A. J.; Faulkner, L. R. *Electrochemical Methods: Fundamentals and Applications;* John Wiley & Sons: New York, 2001; Chapter 3, pp 100–104, 125, Chapter 18, pp 152–153.

(57) Allen, P. A.; Hickling, A. Electrochemistry of Sulphur. Part 1. Overpotential in the Discharge of the Sulphide Ion. *Trans. Faraday Soc.* **1957**, *53*, 1626–1635.

CHAPTER 4

CMBINING ELECTROLYSIS WITH THERMOLYSIS: A SAFE/SCALABLE ROUTE TO MULTINARY OXIDE SEMICONDUCTOR FILMS

Used with permission from A. Vali, H-W. Jee, N. Myung, K-J. Paeng, K. Rajeshwar, *ChemElectroChem.* **2021**, *8*, 1251-1258.

ABSTRACT

Adding a thermolysis step to electrosynthesis (as in "electrothermosynthesis") considerably enhances the scope of electrochemical film deposition and affords multinary compositions previously inaccessible to this otherwise versatile and mild synthetic approach. Copper pyrovanadate (β-$Cu_2V_2O_7$), a member of the Cu-V-O family of ternary oxide semiconductors of considerable interest to the solar fuels community, is shown herein to be an exemplar of this approach. The generality of the hybrid approach is finally discussed for a variety of ternary metal oxides.

4.1. INTRODUCTION

The solid-state chemistry and lithium ion battery communities have taught us that adding one or more cationic elements to a binary compound architecture considerably enhances the performance and properties of the parent chemical framework. Examples of this paradigm may be found in the ternary and quaternary metal chalcogenide compositions (e.g., $CuInSe_2$, $CuInGaSe_2$) that have

been developed for photovoltaic solar cell applications.[1] Similarly, the Cu-V-O family of ternary compounds have shown enhanced stability (relative to the copper oxide parent) and have also furnished unique opportunities for developing composition-property relationships in a photoelectrochemical (PEC) solar fuels context.[2-6] In general, multinary compound semiconductors are important in a variety of practical device applications beyond those identified above. However, films of these compounds have been mostly synthesized so far by ultrahigh vacuum based techniques (e.g., sputtering). Unfortunately, solar device applications in particular require large active areas, and therefore, such techniques are not attractive from scalability, cost, and safety perspectives.

On the other hand, electrosynthetic procedures have many advantages.[7-12] They are solution-based, inexpensive, and scalable. Complex, integrated structures and doped or alloyed films can be easily built up by simple switching of the bath chemistry and/or by incorporating a flow mode of operation.[7-12] Therefore, it is not surprising that electrodeposition has emerged as a viable semiconductor film synthesis candidate.

In this paper, we show that the scope of electrosynthesis can be considerably enhanced by incorporating a thermolysis step. This approach was initially developed for multinary chalcogenide films.[1] For example, for the synthesis of $CuInX_2$ (X = S, Se), a copper-indium alloy film is first electrosynthesized.[1] In the subsequent, thermolysis step, this film is reacted with H_2X gas for ultimate conversion to $CuInX_2$.[1] However, H_2X is noxious and therefore, poses severe safety/scalability issues. On the other hand, the hybrid, "electrothermodeposition" (ETD) variant, is shown herein to be particularly safe and scalable in the case of multinary oxide semiconductors where the thermolysis step only involves an inert and non-toxic gas such as dioxygen (O_2).

We further show that β-$Cu_2V_2O_7$ is a particularly good example of the ETD approach. The Cu-V-O compound family has generated intense interest from the PEC solar fuel community.[3-6,13-21] Combining V_2O_5 and CuO in different stoichiometries generates a series of ternary copper(II) vanadates (CuV_2O_6, $Cu_2V_2O_7$, $Cu_3V_2O_8$, $Cu_{11}V_6O_{26}$, and $Cu_5V_2O_{10}$)[3-6,13-21] with significantly higher stability in a water splitting environment relative to their binary oxide (CuO and V_2O_5) constituents. Notwithstanding the intrinsic advantages of electrosynthesis as noted earlier, the use of this approach for synthesizing copper vanadate films, however, has been conspicuous by its absence.

We finally discuss the present results in the light of available data on a range of other ternary compounds to illustrate the generality and versatility of the ETD paradigm. For the specific case of β-$Cu_2V_2O_7$, we utilized a two-stage electrosynthesis step (Figure 4-1) to first generate an amorphous $CuVO_3$ layer. The second thermolysis step of this film in air, served to both crystallize and oxidize the initial film, to the targeted β-$Cu_2V_2O_7$ phase.

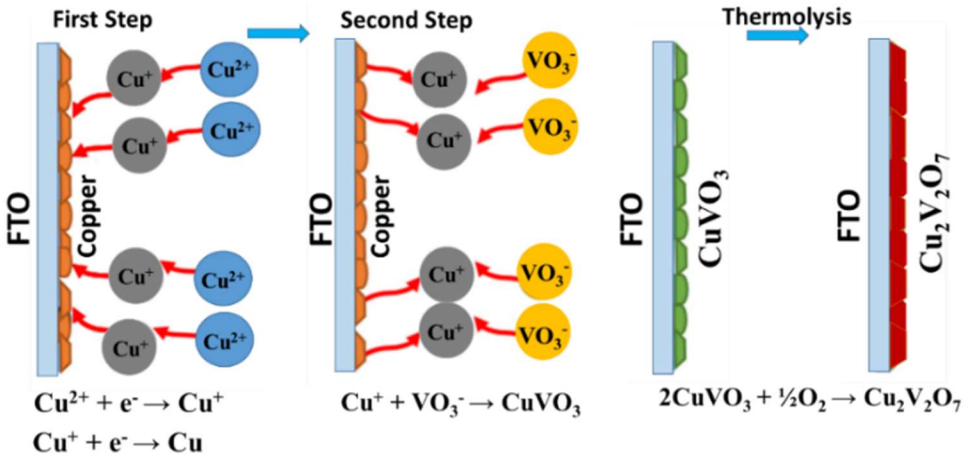

Figure 4-1. Schematic diagram of the hybrid ETD approach to form β-$Cu_2V_2O_7$ thin film on a fluorine doped tin oxide (FTO) support.

4.2. RESULTS AND DISCUSSION

4.2.1. The First Electrosynthesis Step

Copper thin film was first electrodeposited by reduction of Cu^{2+} in a non-aqueous medium, dimethyl sulfoxide (DMSO) solution, to eliminate side electrochemical reactions such as hydrogen and water reduction reactions in the presence of water.[12] Also, using a non-aqueous solvent helps to prepare a smooth thin film of copper.[22] In addition, the electrodeposition solution was purged by nitrogen to quench the oxygen reduction reaction (ORR). ORR helps to drive Cu_2O formation reaction even at room temperature.[23] Figure C-S1 shows a pair of cyclic voltammograms on FTO in in the presence and absence of copper nitrate. Two reduction waves were seen during forward (reduction) scan. The first reduction wave in the range of 0 to -0.2 V was assigned to the following reaction:[23,24]

$$Cu^{2+} + e^- \rightarrow Cu^+ \qquad (4\text{-}1)$$

The second reduction wave was attributed to the reduction of Cu^+ to elemental copper according to the following reaction:[23,24]

$$Cu^+ + e^- \rightarrow Cu \qquad (4\text{-}2)$$

The anodic copper stripping in DMSO solution on the return scan showed two anodic waves. These two anodic waves can be attributed to a two-step stripping sequence, Eqns. 4-3 and 4-4, respectively.[23,24]

$$Cu \rightarrow Cu^+ + e^- \qquad (4\text{-}3)$$

$$Cu^+ \rightarrow Cu^{2+} + e^- \qquad (4\text{-}4)$$

The observed cross-over of the forward and reverse scans in the cyclic voltammogram at ~ -0.23 V (Figure C-S1) is a signature for thermodynamically stable copper nuclei formation and growth of elemental copper on the substrate.[25,26]

As in our previous studies,[24,27,28] the combination of voltammetry and electrochemical quartz crystal nanogravimetry (EQCN), proved to be useful for gleaning mechanistic insights. Both the voltammetry (current *vs.* potential) and corresponding EQCN (frequency change *vs.* potential) plots for the electrodeposition of copper are shown in Figure 4-2. The EQCN data showed that over the first reduction wave (+0.3 to -0.23 V), the cathodic current increased with more negative potential while the frequency remained constant. This diagnosed that no deposition or mass gain

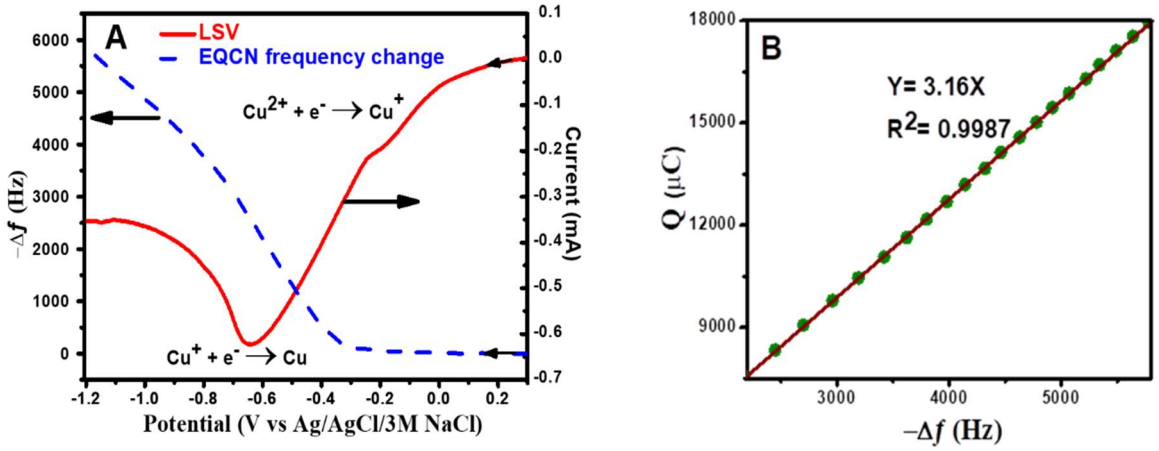

Figure 4-2. (A) Linear sweep voltammogram (—) and the corresponding EQCN frequency change (---) for the electrodeposition of copper on Pt at 25 mV/s potential scan rate. (B) Charge-frequency change plot derived from the EQCN-voltammetry data.

occurred in this potential window. Therefore, Reaction 4-1 (reduction of Cu^{2+} to soluble Cu^{+}) was dominant in this wave. The frequency decreased along the second reduction wave (potentials lower than -0.3 V) and the increased mass could be attributed to copper electrodeposition (Reaction 4-2). The number of transferred electrons for an electrochemical deposition reaction can be determined by plotting Q *vs.* $-\Delta f$ and applying Sauerbrey equation:[27-30]

$$Q = -\left(\frac{nFk}{M}\right)\Delta f \qquad (4\text{-}5)$$

Q is the transferred charge, F is the Faraday constant, Δf is the frequency change, k is the Sauerbrey constant,[27-30] n is the number of transferred electrons, and M is the molar mass of the deposited compound. The number of transferred electrons (n) can be estimated from the slope of the linear part of charge-frequency change plot (Figure 4-2B). The estimated n value was 1.93, close to the expected stoichiometry value for the following reduction reaction:

$$Cu^{2+} + 2e^- \rightarrow Cu \qquad (4\text{-}6)$$

Both the energy-dispersive X-ray (EDX) and X-ray diffraction (XRD) patterns of the copper thin film on FTO (Figures C-S2 and C-S3) confirmed the presence of pure elemental copper on the substrate. Note that a preferred orientation of the (111) plane was observed, consistent with reported XRD data for copper thin films.[31,32]

4.2.2. The Second Electrosynthesis Step

In the second step (see Figure 4-1), copper stripping in the presence of 0.04 M NH_4VO_3 revealed only one anodic wave (Figure 4-3A), while in DMSO solution (in the ***absence*** of vanadate ions) two anodic waves were seen (see Figure C-S1). Therefore, copper was only oxidized to Cu^+ in the presence of vanadate ions. Furthermore, the oxidation wave was accompanied by frequency decrease in the presence of VO_3^- ions (Figure 4-3A). These results are consistent with Cu^+ ions participating in a precipitation reaction with VO_3^- ions (dominant vanadate species at pH 7.0)[33] to form a green $CuVO_3$ film, according to the following reaction:

$$Cu^+ + VO_3^- \rightarrow CuVO_3 \qquad (4\text{-}7)$$

The electron stoichiometry (n) estimated from the slope of the linear part of charge-frequency change plot (Figure 4-3B) was 0.86 which was reasonably close to the expected stoichiometry value for the following reduction reaction:

$$Cu + VO_3^- \rightarrow CuVO_3 + e^- \qquad (4\text{-}8)$$

The slight delay in the frequency change onset in comparison to the anodic current onset is reminiscent of the trend previously observed for $AgVO_3$ and Ag_3VO_4[34,35] and suggests a nucleation/growth mechanism underlying it.

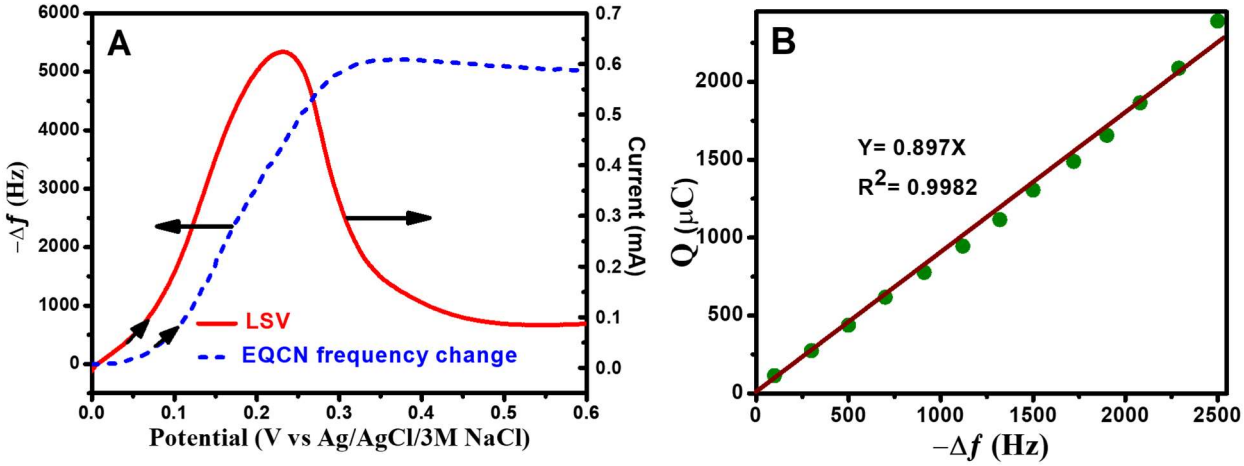

Figure 4-3. (A) Linear sweep voltammogram (—) and the corresponding EQCN frequency change (---) for the electrodeposition of copper vanadate ($CuVO_3$) on Pt at 15 mV/s potential scan rate. (B) Charge *vs.* frequency change plot constructed from the EQCN-voltammetry data.

For further characterization of the initially prepared film, a potentiodynamic synthesis protocol was deployed to enhance film adhesion to the FTO substrate and to control the film thickness. The potential was scanned from -0.20 to -1.20 V at 25 mV/s scan rate for several cycles (4, 8, 10, 12, and 14 cycles) to achieve the required copper template film thickness; the rest time between cycles was 30 s. The film after the second electrosynthesis step was XRD-silent (Figure 4-4b) suggesting that it was amorphous; EDX data (not shown) were consistent with a 1:1 Cu:V stoichiometry as expected for $CuVO_3$. Figure C-S4 (frames A-C) shows photographs of the $CuVO_3$

film for three values of the thickness.; the film had a green hue (see above) and darkened as it got thicker.

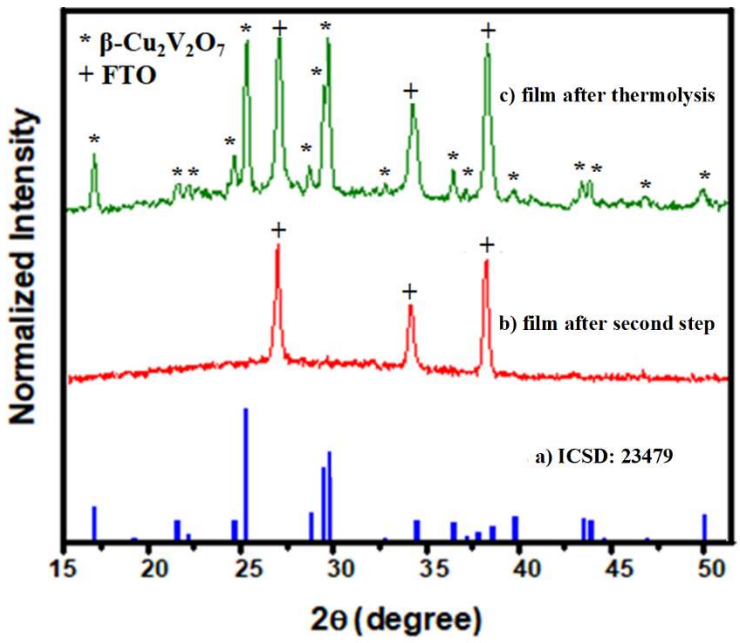

Figure 4-4. XRD patterns of (a) reference β-$Cu_2V_2O_7$ (b) film after the second electrosynthesis step and (c) sample after the final thermolysis step in air.

4.2.3. The Third Thermolysis Step

The third and final step in the ETD sequence consists of thermolysis (c.f., Figure 4-1). Thus, the prepared $CuVO_3$ thin film was thermally oxidized at 450 ºC for 1 h in air to form β-$Cu_2V_2O_7$ film (Figure 4-1). Thermal oxidation of the as-prepared film (Reaction 4-9) was accompanied by a color change from green to burnt orange.

$$2CuVO_3 + ½O_2 \rightarrow Cu_2V_2O_7 \qquad (4\text{-}9)$$

Photographs of the β-$Cu_2V_2O_7$ thin films with different thicknesses are shown in Figure C-S4, frames D-F. The initially green $CuVO_3$ phase was converted to a burnt orange β-$Cu_2V_2O_7$ by the final ETD step. It is worth noting that this color change was observed only above 300 ºC,

rationalizing the above choice of the thermolysis temperature. However, the crystallinity of the sample was poor at 300 °C. On another hand, the beta phase is transferred to alpha phase above 500 °C.[3] Therefore, a temperature of 450 °C was chosen as a compromise to obtain a phase pure β-$Cu_2V_2O_7$ film.

XRD data (Figure 4-4c) confirmed formation of the targeted β-$Cu_2V_2O_7$ film in crystalline form. Clearly, the final thermolysis step in the overall ETD sequence accomplished both the crystallization and copper oxidation functions. Thus, comparison of the SEM images for the as-prepared and annealed samples (Figure C-S5) revealed that the particle size of copper vanadate had increased as it was converted via ETD from $CuVO_3$ to β-$Cu_2V_2O_7$. An EDX scan of the β-$Cu_2V_2O_7$ film is shown in Figure C-S2, frame C. A Cu/V ratio as 0.96 ± 0.03 was estimated by averaging the compositional EDX assays from different points of the sample surface. Elemental EDX maps (not shown) revealed uniform distribution of the electrodeposited film; no elemental copper and/or vanadium rich regions could be observed.

4.2.4. Product Characterization

The phase purity of the ETD-derived β-$Cu_2V_2O_7$ film samples was probed via laser Raman spectroscopy; Figure 4-5 contain the data. The obtained Raman bands were in good agreement with those reported for polycrystalline β-$Cu_2V_2O_7$ samples synthesized by other techniques.[15,36,37] All the Raman bands could be assigned to β-$Cu_2V_2O_7$; specifically, no peaks were found for other possible compounds such as V_2O_5, CuO, α-$Cu_2V_2O_7$, and CuV_2O_6.[36,37] The bands at 910 cm^{-1} and 856 cm^{-1} were attributed to the terminal VO_3 stretching modes, while the bands at 787 cm^{-1} and 539 cm^{-1} were assigned to bridging VOV stretching modes.[36,37] The bands at 392, 285, and 252

cm^{-1} were attributed to OVO_3/VO_3 bending vibration modes.[36,37] The small peak at 350 cm^{-1} was assigned to the VO_3 bending mode.[36,37]

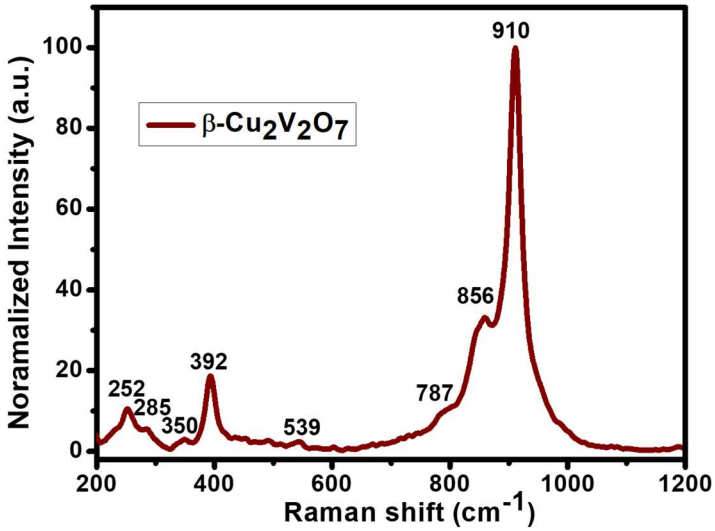

Figure 4-5. Representative laser Raman spectrum of a β-$Cu_2V_2O_7$ thin film on FTO prepared via ETD.

Figure 4-6 contains high resolution X-ray photoelectron spectroscopy (XPS) data for both the initially deposited $CuVO_3$ phase and for the thermally converted β-$Cu_2V_2O_7$ phase. Focusing on the Cu binding energy regime (Figure 4-6, frames A and D) and comparing the Cu $2p_{3/2}$ and Cu $2p_{1/2}$ peaks with binding energies for Cu species in the literature,[38] the sample from the second ETD step contained both Cu^+ (Cu $2p_{3/2}$ and Cu $2p_{1/2}$ peaks at 932.0 eV and 952.1 eV respectively) and Cu^{2+} (Cu $2p_{3/2}$ and Cu $2p_{1/2}$ peaks at 933.9 eV and 953.9 eV respectively) while the thermolytically converted ETD sample contained only Cu^{2+} as expected. The unexpected observation in Figure 4-6A indicates that the surface of $CuVO_3$ was not stable at room temperature since this sample should have only contained Cu^+ species.

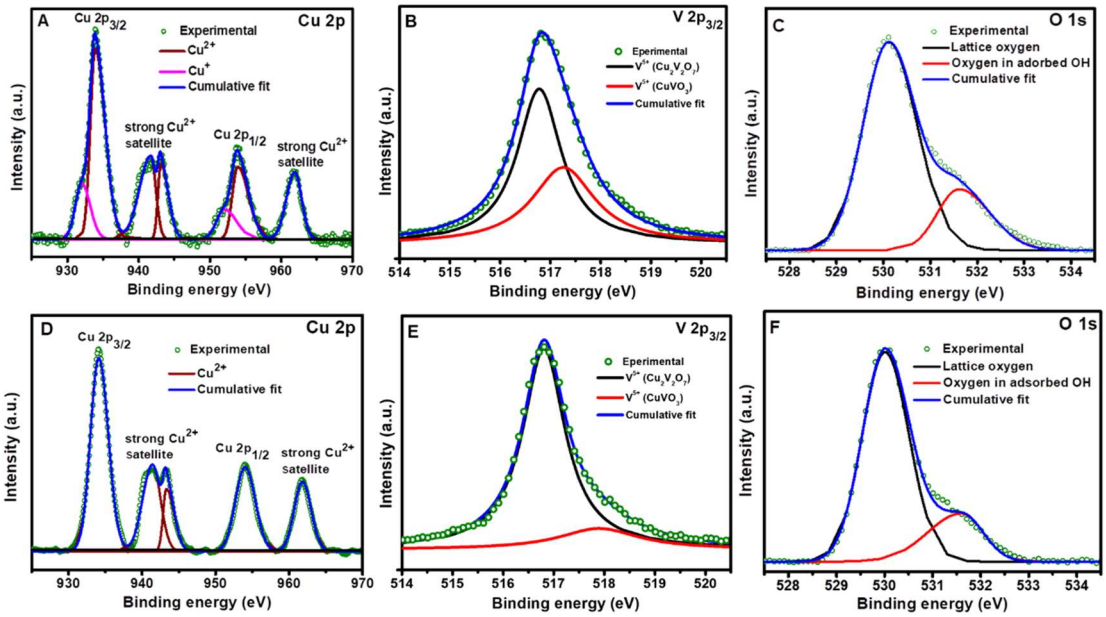

Figure 4-6. High resolution XPS data for the thin film samples from the second ($CuVO_3$) and third (β-$Cu_2V_2O_7$) steps in the ETD sequence for (A and D) Cu 2p, (B and E) V 2p, (C and F) O 1s binding energy regimes.

A comparison between the high resolution V 2p XPS scans of the copper vanadate samples from the second and third ETD steps (Figures 4-6B and E) indicated that the magnitude of the V^{5+} feature for $CuVO_3$ (517.8 eV) was significantly decreased. This corroborates the thermal oxidation of $CuVO_3$ to $Cu_2V_2O_7$ (Reaction 4-9) as explained above. Note that the presence of trace amount of $CuVO_3$ in the sample from the third ETD step is due to the decomposition of $Cu_2V_2O_7$ during cooling of the sample.[40] A dominant O 1s peak at 530.1 eV in the high resolution O 1s XPS spectra (Figures 4-6C and F) was assigned to lattice oxygen in both the copper vanadates.[15] The second O 1s peak at 531.5 eV corresponded to the oxygen in adsorbed OH^- groups in both samples.[15] Notably, the XPS data for the sample after thermolysis (Figure 4-6D) showed no signatures for Cu^+.

Other optical, structural, and electronic aspects of the ETD-derived β-$Cu_2V_2O_7$ samples will be elaborated elsewhere.[41]

The data in Figure 4-7 pertain to both the "dark" and irradiated conditions and for varying values of the film thickness. Such data offer insights into both the photocurrent generation mechanisms as well as film stability; however these aspects extend beyond the scope of the present proof-of-concept study and will be addressed elsewhere.[41]

For now, it is simply noted that these samples behave as an n-type semiconductor; Figure 4-7 contains photoelectrochemical (PEC) data in aqueous borate buffer. The data in Figure 4-7 pertain to both the "dark" and irradiated conditions and for varying values of the film thickness. Such data offer insights into both the photocurrent generation mechanisms as well as film stability; however these aspects are beyond the scope of the present proof-of-concept synthetic study and will be addressed elsewhere.[41] The highest photocurrent was collected for a 900 nm thick film (Figure 4-7). The observed decrease in the photocurrent from 900 nm to 1050 nm is attributed to increased recombination of the photogenerated electrons and holes. Since the electrons must travel a more circuitous pathway to reach the FTO/semiconductor junction for a thick film, the recombination probability is increased. Table B-S1 compiles the obtained photocurrent density value at 1.23 V vs RHE for our best-performing β-$Cu_2V_2O_7$ photoanode along with literature data. Note these data were collected in the absence of a hole scavenger. Significantly, the obtained photocurrent in this study (0.12 mA/cm^2 at 1.23 V vs RHE) was higher than samples synthesized in other studies except for the Ref. 16 case. The observed high photocurrent in Ref. 16 was attributed to a unique morphology (nanoplate) of the synthesized sample. Photoelectrochemical (PEC) experiments were also conducted in 0.2 M borate buffer (pH: 8.6) for our best-performing β-$Cu_2V_2O_7$ photoanode with and without a hole scavenger, namely, sodium formate. Figure 4-8A presents the corresponding photovoltammetry data for β-$Cu_2V_2O_7$ film on FTO. The photocurrent was significantly increased in the presence of hole scavenger, as expected. PEC water oxidation

clearly is a sluggish process relative to formate oxidation. Further, the inset Figure 4-8A shows that the photocurrent onset potential was shifted to more negative potentials in the presence of the hole scavenger. Again, this trend is easily rationalized by the fact that since electron-hole recombination rate is decreased when the interfacial electron transfer rate is enhanced. The photocurrent onset potential was +0.75 V *vs.* RHE in the presence of hole scavenger, which is very close to the values reported in the literature for samples synthesized by other techniques.[3,6,15,19] Table B-S2 compares the obtained photocurrent density value at 1.0 V vs RHE for our best-performing β-$Cu_2V_2O_7$ photoanode along with literature data. Also, these data are collected in the presence of hole scavenger. Once again, the obtained photocurrent in this study (0.40 mA/cm^2 at 1.0 V vs RHE) was higher than samples synthesized by other groups. All other studies used sodium sulfite as a hole scavenger, while sodium formate was used instead in this study. A significant amount of dark current has been reported for β-$Cu_2V_2O_7$ photoanode in the presence of sodium sulfite at potentials above 1.1 V vs RHE.[3,6,19,21] For example, note that the photovoltammogram in the presence of sodium formate (green scan, Figure 4-8A) showed negligible dark current till 1.5 V vs RHE. Therefore, all photocurrent density values in Table B-S2 were compared at 1.0 V vs RHE. The photocurrent onset at ~635 nm in the action spectrum (Figure 4-8B) was entirely consistent with the optical band gap of these samples (2.08–2.21 eV) as measured by diffuse reflectance spectroscopy.[41]

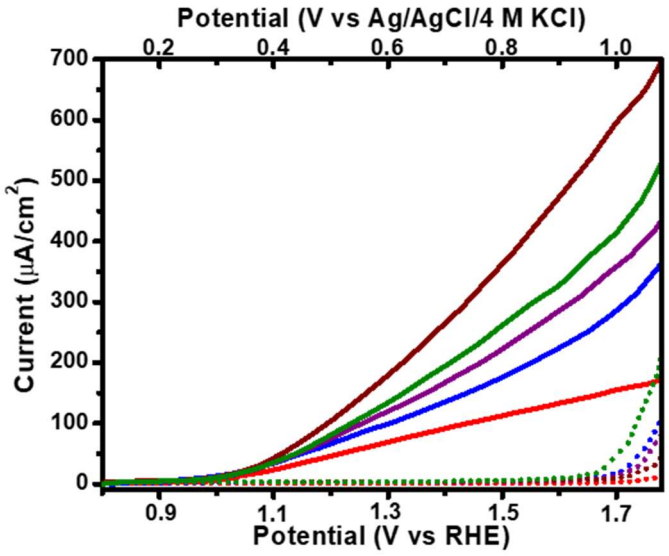

Figure 4-7. Photocurrent (–) and dark current (….) for β-$Cu_2V_2O_7$ in nitrogen-purged 0.2 M borate buffer solution (pH: 8.6) at different film thicknesses. Red: 300 nm, Blue: 600 nm, Purple: 750 nm, Brown: 900 nm, and Green: 1050 nm. The incident power was 100 mW/$cm^2$and the potential scan rate was 5 mV/s.

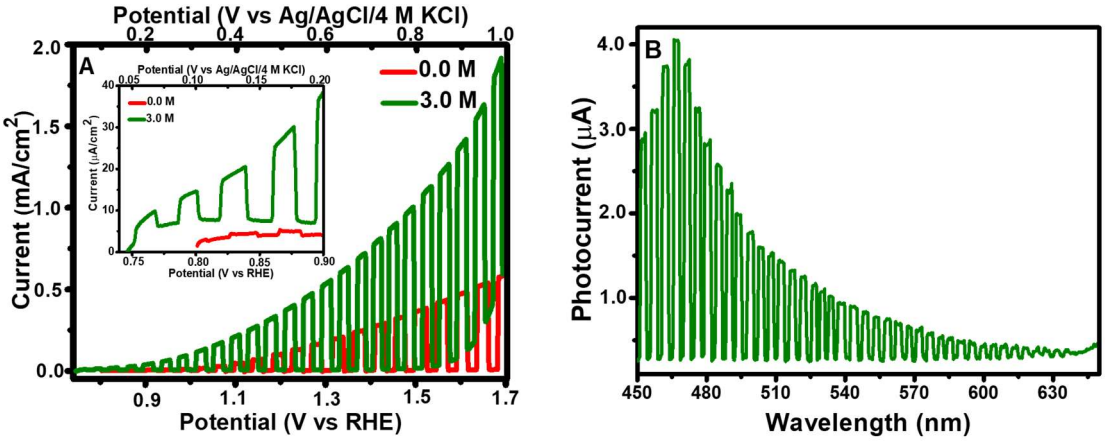

Figure 4-8. A. Photocurrent for β-$Cu_2V_2O_7$ (900 nm thickness film) in nitrogen-purged 0.2 M borate buffer solution (pH: 8.6). The potential scan rate was 5 mV/s. B. A photoaction spectrum in the same electrolyte but also containing 3.0 M sodium formate as a hole scavenger. The potential was held at 1.23 V *vs.* RHE in this case.

4. 3. GENERAL DISCUSSION

The Cu-V-O family has afforded demonstration of the power of the ETD approach. The β-$Cu_2V_2O_7$ phase of interest from a solar fuels application perspective was not directly synthesizable via conventional electrodeposition. However, by incorporating a final thermolysis step in a two-stage electrosynthesis scheme (Figure 4-1), the initially formed amorphous $CuVO_3$ precursor could be converted to a crystalline β-$Cu_2V_2O_7$ product.

A search of the literature reveals, however, other process variants of ETD that further extend its generality and scope. Table 4-1 summarizes illustrative examples of work from other laboratories. Thus, either the two binary oxide constituents or the two metal components can be electrosynthesized first followed by their thermolytic conversion to the targeted ternary oxide product (see Table 4-1).[43-48] Clearly, these tabulated examples, along with the β-$Cu_2V_2O_7$ case highlighted in this work, show that addition of a thermolysis step considerably enhances the scope of electrosynthesis.

Table 4-1. Examples illustrating variations on the ETD theme.

Ternary oxide	Electrosynthesis step	Thermolysis step	Reference
$BiVO_4$	Cathodic deposition of Bi metal from an ethylene glycol bath.	Conversion to product after soaking in $VO(acac)_2$ and thermolysis in air at 450 ºC.	43
$CuWO_4$	Codeposition of Cu_2O and WO_3 from an acidic aqueous bath.	Thermolysis at 500 ºC in air.	44
$CuWO_4$	Cathodic deposition of WO_3.	Thermolysis in air at 550 ºC in contact with copper (II) nitrate soln.	45
Bi_2WO_6	Same as above.	Same as above but with bismuth (III) nitrate solution used instead.	45
$CuFeO_2$	Cathodic codeposition of Cu and Fe from a DMSO bath.	Thermolysis at 650 ºC in argon.	46
$CuBi_2O_4$	Cathodic codeposition of Cu and Bi in 1: 2 ratio.	Thermolysis at 600 ºC in air.	47
$CuBi_2O_4$	Anodic codeposition of CuO and Bi_2O_3 at 60 ºC.	Thermolysis at 500 ºC in air.	48

4.4. CONCLUSIONS

In this study, the technologically important Cu-V-O ternary oxide system was used to demonstrate a new film synthesis approach (ETD) that powerfully combines electrosynthesis and thermosynthesis. Specifically, synthesis of an elusive compound in this system, namely: β-$Cu_2V_2O_7$, was secured via ETD. Unlike in the metal chalcogenide cases, the thermolytic metal alloy → ternary metal oxide conversion in ETD is safe and scalable. Also worth noting is that this thermolytic step may also serve to additionally impart (or improve) crystallinity in the deposited film like the thermal anneal that is routinely used as a post-deposition tool.

4.5. EXPERIMENTAL SECTION

4.5.1. Materials

Copper nitrate hemi(pentahydrate) [$Cu(NO_3)_2{\cdot}2.5H_2O$ (Alfa Aesar)] and ammonium metavanadate [NH_4VO_3 (Alfa Aesar)] were used as copper and vanadium sources, respectively. Dimethyl sulfoxide [C_2H_6OS (Sigma-Aldrich)] were used as the non-aqueous solvent. Potassium nitrate [KNO_3 (Alfa Aesar)] was used as an electrolyte for the electrodeposition of copper. Boric acid [H_3BO_3 (Alfa Aesar)] and sodium borate [($Na_2B_4O_7{\cdot}10\ H_2O$ (Sigma-Aldrich)] were used to prepare borate buffer solution (pH: 8.6) for the PEC characterization. Sodium formate [HCOONa (Sigma-Aldrich)] was used as a hole scavenger for photoaction spectroscopy.

4.5.2. Electrosynthesis Details

In the first electrosynthesis step (Figure 4-1), the copper thin film was cathodically deposited on a working electrode, fluorine doped tin oxide (FTO) substrate (FTO characteristics in Ref. 34 in the main text), in a single compartment, three-electrode cell setup. The counterelectrode and reference electrode were platinum foil and Ag/AgCl/4M KCl, respectively.

The electrodeposition solution contained 40 mM $Cu(NO_3)_2 \cdot 2.5H_2O$ as the copper source and 100 mM KNO_3 as a supporting electrolyte in dimethyl sulfoxide (DMSO). Other details are presented in the main text.

The electrodeposition of copper was carried out by passing 0.034 C/cm^2 for each cycle. We can calculate the number of moles for electrodeposited copper using Eqn. 4-6 and the passed charge for each cycle (Faraday's Law). Then, the number of moles of $Cu_2V_2O_7$ could be estimated from the formation/stripping reactions from which the mass of $Cu_2V_2O_7$ was calculated. By taking the density of $Cu_2V_2O_7$ as 3.96 g/cm^3,[49] the volume of deposited $Cu_2V_2O_7$ was calculated and divided by the working electrode area to obtain the film thickness. Each cycle increased the film thickness by ~75 nm.

In the second step in Figure 4-1, the electrodeposited copper film was anodically stripped in a 40 mM ammonium metavanadate solution (pH: 7.0) to generate Cu^+ which subsequently was precipitated with VO_3^- to form an amorphous $CuVO_3$ film on the substrate (Scheme 1). The thin film was built up by repeated scanning of the potential from +0.15 V to +0.35 V at 15 mV/s. The rest time between cycles was 15 s. When the anodic current due to oxidation of copper (stripping) ceased, the potentiodynamic sweeps were stopped.

4.5.3. Instrumentation

Details of the instruments used for X-ray diffraction (XRD), energy-dispersive X-ray (EDX), and X-ray photoelectron spectroscopy (XPS) were given elsewhere.[34,35] A Horiba Jobin Yvon (Model LabRAM ARAMIS) instrument was used to collect laser Raman spectra of the prepared copper vanadate thin films. A laser excitation wavelength of 632 nm (1.96 eV) with a 50× objective and 0.3 mW incident power were deployed for these measurements.

Details of the instrumentation for electrochemical, photoelectrochemical, and electrochemical quartz crystal nanogravimetry (EQCN) experiments may be found elsewhere.[34,35] The illumination source was a W/Xe lamp and the incident power was 100 mW/cm^2. For photoaction spectroscopy (Figure 4-7B), a Model 74125 Oriel Cornerstone 260 monochromator (1/4 m focal length) was used. The wavelengths were scanned from 645 to 450 nm. The wavelength interval was 5 nm, and both the illumination and dark periods were set at 5 s at each wavelength.

4.6. REFERENCES

(1) K. Rajeshwar, R. T. Macaluso, *Chalcogenides: Solid-State Chemistry.* In *Encyclopedia of Inorganic and Bioinorganic Chemistry*. John Wiley, New York, **2020**.
(DOI: 10.1002/9781119951438.eibc0038.pub2)

(2) K. Rajeshwar, M. K. Hossain, R. T. Macaluso, C. Janáky, A. Varga, P. J. Kulesza, *J. Electrochem. Soc.* **2018**, *165*, H3192−H3206.

(3) M. K. Hossain, P. Sotelo, H. P. Sarker, M. T. Galante, A. Kormányos, C. Longo, R. T. Macaluso, M. N. Huda, C. Janáky, K. Rajeshwar, *ACS Appl. Energy Mater*, **2019**, *4*, 2837−2847.

(4) M. K. Hossain, H. P. Sarker, P. Sotelo, U. Dang, I. R. Gutiérrez, J. Blawat, A. Vali, W. Xie, G. Oskam, M. N. Huda, R. T. Macaluso, K. Rajeshwar, *Chem. Mater.* **2020,** *32*, 6247−6255.

(5) L. Zhou, Q. Yan, J. Yu, R. J. Jones, N. Becerra-Stasiewicz, S. K. Suram, A. Shinde, D. Guevarra, J. B. Neaton, K. A. Persson, J. M. Gregoire, *Phys. Chem. Chem. Phys*. **2016**, *18*, 9349−9352.

(6) C-M. Jiang, G. Segev, L. H. Hess, G. Liu, G. Zaborski, F. M. Toma, J. K. Cooper, I. D. Sharp, *ACS Appl. Mater. Interfaces* **2018**, *10*, 10627−10633.

(7) K. Rajeshwar, *Adv. Mater*. **1992**, *4*, 23–29.

(8) T. E. Schlesinger, K. Rajeshwar, N. R. de Tacconi in *Modern Electroplating*, (Eds.: M. Schlesinger, M. Paunovic), Springer, New York, **2010**, chapter 14, pp 383–411.

(9) K. Rajeshwar, N. R. de Tacconi, Chenthamarakshan, C. R. *Chem. Mater*. **2001**, *13*, 2765–2782.

(10) C. Janáky, K. Rajeshwar, *Prog. Poly. Sci.* **2015**, *43*, 96–135.

(11) C. Janáky, E. Kescenovity, K. Rajeshwar, *ChemElectroChem* **2016**, *3*, 181–192.

(12) D. Kang, T. W. Kim, S. R. Kubota, A. C. Cardiel, H. G. Cha, K-S. Choi, *Chem. Rev*. **2015**,

115, 12839−12887.

(13) P. F. Newhouse, D. A. Boyd, A. Shinde, D. Guevarra, L. Zhou, E. Soedarmadji, G. Li, J. B. Neaton, J. M. Gregoire, *J. Mater. Chem. A* **2016**, *4*, 7483−7494.

(14) L. P. Camargo, A. C. Lucilha, G. A. B. Gomes, V. R. Liberatti, A. C. Andrello, P. R. C. da Silva, L. H. Dall'Antonia. *J. Solid State Electrochem.* **2020**, *24*, 1935–1950.

(15) A. Song, A. Chemseddine, I. Y. Ahmet, P. Bogdanoff, D. Friedrich, F. F. Abdi, S. P. Berglund, R. van de Krol, *Chem. Mater.* **2020**, *32*, 2408−2419.

(16) S. S. Kalanur, H. Seo. *Appl. Catal. B: Environ.* **2019**, *249*, 235–245.

(17) C. M. Jiang, M. Farmand, C. H. Wu, Y. S. Liu, J. Guo, W. S. Drisdell, J. K. Cooper, I. D. Sharp, *Chem. Mater*. **2017**, *29*, 3334−3345.

(18) L. Zhou, Q. Yan, A. Shinde, D. Guevarra, P. F. Newhouse, N. Becerra-Stasiewicz, S. M. Chatman, J. A. Haber, J. B. Neaton, J. M. Gregoire, *Adv. Energy Mater.* **2015**, *5*, 1–13.

(19) W. Guo, W. D. Chemelewski, O. Mabayoje, P. Xiao, Y. Zhang, C. B. Mullins, *J. Phys. Chem.*C **2015**, *119*, 27220−27227.

(20) M. W. Kim, B. Joshi, H. Yoon, T. Y. Ohm, K. Kim, S. S. Al-Deyab, S. S. Yoon, *J. Alloys Compd*. **2017**, *708*, 444−450.

(21) W. Guo, X. Lian, Y. Nie, M. Hu, L. Wu, H. Gao, T. Wang, *Mater. Lett.* **2020**, *258*, 126842.

(22) A. M. M. Ahmed, S. M. A. Haleem, M. Darewish, A. S. El Kaliea, *J. Disper. Sci. Technol.* **2012**, *33*, 898–912.

(23) G. Riveros, A. Garmendia, D. Ramirez, M. Tejos, P. Grez, H. Gomez, E. A. Dalchiele, *J. Electrochem. Soc.* **2013**, *160*, D28−D33.

(24) M. Zhou, N. Myung, X. Chen, K. Rajeshwar, *J. Electroanal. Chem.* **1995**, *398,* 5−12.

(25) L. H. Mendoza-Huizar, J. Robles, M. Palomar-Pardave, *J. Electroanal. Chem*, **2002**, *521,* 95–106.

(26) R. Greef, R. Peat, L. M. Peter, D. Pletcher, J. Robinson, *Instrumental Methods in Electrochemistry*, Ellis Horwood, Chichester, **1985**, pp 210–211.

(27) N. Myung, S. Ham, S. Choi, Y. Chae, W-G. Kim, Y. J. Jeon, K. J. Paeng, W. Chanmanee, N.R. de Tacconi, K. Rajeshwar, *J. Phys. Chem. C.* **2011**, *115*, 7793−7800.

(28) S. Ham, S. Jeon, M. Park, S. Choi, K-J. Paeng, N. Myung, K. Rajeshwar, *J. Electroanal. Chem.* **2010**, *638*, 195–203.

(29) M. R. Deakin, D. A. Buttry, *Anal. Chem.***1989,** *61*, 1147A–1154A.

(30) D. A. Buttry in *Electroanalyitcal Chemistry: A Series of Advances,* Vol. 17, (Edited by A. J. Bard), Marcel Dekker, New York, **1991**.

(31) M. Morimoto, Y. Takatsuji, R. Yamasaki, H. Hashimoto, I. Nakata, T. Sakakura, T. Haruyama, *Electrocatalysis,* **2018**, 9, 323–332.

(32) F. Cemin, D. Lundin, C. Furgeaud, A. Michel, G. Amiard, T. Minea, G. Abadias, *Sci. Rep*. **2017**, *7*, 1655.

(33) C. F. Baes, R. E. Messmer, *The Hydrolysis of Cations*, John Wiley & Sons, New York, **1976**, pp 197–210.

(34) A. Vali, P. H. Sarker, H.-W. Jee, A. Kormanyos, F. Firouzan, N. Myung, N. K.-J. Paeng, M. N. Huda, C. Janaky, K. Rajeshwar, *ChemPhysChem*, **2019**, *20*, 2635−2646.

(35) A. Vali, P. S. Toth, H-W. Jee, F. Firouzan, C. Janaky, K-J. Paeng, N. Myung, K. Rajeshwar, *J. Phys. Chem. C,* **2020**, *124*, 1980−1989.

(36) D. de Waal, C. Hutter, *Matter. Res. Bull.* **1994**, *29*, 843−849.

(37) M. Machida, T. Kawada, S. Hebishima, S. Hinokuma, S. Takeshima, *Chem. Mater.* **2012**, *24*, 557−561.

(38) M. C. Biesinger, *Surf. Interface Anal.* **2017**, *49*, 1325–1334.

(39) M. Nakamura, H. Namatame, A. Fujimori, A. Misu, S. Okatake, M. Onoda, H. Nagasawa, *J. Solid State Chem.* **1994**, *112*, 100−105.

(40) B. V. Slobodin, R. F. Samigullina, *Inorg. Mater,* **2010***, 46,* 196−200.

(41) A. Vali. H. P. Sarker, I. Rodríguez-Gutiérrez, B. Heredia, G. Oskam, M. N. Huda, K. Rajeshwar, to be published.

(42) C. Gadiyar, M. Strach, P. Schouwink, A. Loiudice, R. Buonsanti, *Chem. Sci.* **2018**, *9*, 5658−5665.

(43) D. Kang, Y. Park, J. C. Hill, K.-S. Choi, *J. Phys. Chem. Lett.* **2014**, *5*, 2994−2999.

(44) J. E. Yourey, B. M. Bartlett, *J. Mater. Chem*. **2011**, *21*, 7651−7610.

(45) J. C. Hill, K.-S. Choi, *J. Mater. Chem. A* **2013**, *1*, 5006−5014.

(46) C. G. Read, Y. Park, Y. K.-S. Choi, *J. Phys. Chem. Lett.* **2012**, *3*, 1872−1876.

(47) N. T. Hahn, V. C. Holmberg, B. A. Korgel, C. B. Mullins, *J. Phys. Chem. C* **2012**, *116*, 6459−6466.

(48) Y. Nakabayashi, M. Nishikawa, Y. Nosaka, *Electrochim. Acta* **2014**, *125*, 191−198.

(49) P. D. Robinson, J. M. Hughes, M. L. Malinconico, *Am. Mineral.* **1987**, *72*, 397−400.

CHAPTER 5

SUMMARY AND PERSPECTIVES

Desirable properties of semiconductors are optimum band gap, proper conduction and valence band edge positions, high quantum yield, good chemical and photoelectrochemical (PEC) stability, and non-toxicity of the component elements. It is difficult for a binary oxide semiconductor to satisfy all these desirable properties simultaneously. One solution is to generate ternary and quaternary oxide semiconductors from binary oxide components. Such multinary compound semiconductors have recently come under the spotlight for solar fuel generation applications.

In this research, we systematically studied the effect of adding silver or copper to V_2O_5 and probed alterations in its semiconductor behavior. For the first time, electrodeposition was used to prepare thin films of ternary silver and copper-vanadate semiconductors. From a synthetic perspective, electrodeposition is a fast, low temperature, and scalable method that can be used to prepare semiconductors directly in film form on conductive substrates. In addition, the optoelectronic parameters (e.g., photocurrent, flat band potential) of the thin film semiconductors that are prepared by electrodeposition can be measured easily, without any more processing steps.

Chapter 2 describes a two-step electrodeposition strategy to synthesize two polymorphs of silver metavanadate, α- and β-$AgVO_3$. Then, their physical, optoelectronic, electrochemical, and photoelectrochemical properties were evaluated experimentally. In addition, a (collaborative) computational study was performed to provide details of the α→ β phase transformation mechanism and band structure of the two polymorphs.

In Chapter 3, the mechanistic details of electrodeposition of a silver-rich member of the Ag-V-O family, namely, Ag_3VO_4, are provided. Subsequently, the physical, thermal,

optoelectronic, electrochemical, and photoelectrochemical properties of this semiconductor are discussed in depth. Interestingly, my results showed that the as-prepared sample at room temperature was crystalline and phase pure with a high concentration of holes. Such optimal behavior was elusive in previous studies of this compound

Chapter 4 explains the details of a hybrid electrochemical/thermolysis route, namely electrothermodeposition (ETD), for synthesizing the β-$Cu_2V_2O_7$ photoanode. In this chapter, the details of using two complementary processes, namely electrosynthesis and thermolysis, are given to prepare a multinary oxide film on the conducting substrate.

In the case of the electrodeposited $AgVO_3$ and Ag_3VO_4 samples, considerable further improvements in the quality of semiconductor/electrolyte junctions are needed to prevent their cathodic corrosion in an aqueous medium. To this end, chemical modification of electrosynthesized $AgVO_3$ and Ag_3VO_4 film surfaces may be a viable strategy for future work.

In the case of β-$Cu_2V_2O_7$, further work is needed to improve its charge separation efficiency. Several complementary strategies such as doping, nanostructuring, and co-catalyst modification can be applied to improve the low hole diffusion length and sluggish water oxidation reaction kinetics. For example, the charge separation efficiency can be increased by increasing the mobility of charge carriers of β-$Cu_2V_2O_7$ through Mo or W doping.

Combining Ag_2O with CuO possibly generates a ternary oxide, namely, $Ag_2Cu_2O_3$ (see Ag_2O-CuO line of Figure 1-2). This ternary oxide exhibits semiconducting behavior with a low band gap (2.2 eV). Adding V^{5+} to $Ag_2Cu_2O_3$ can generate a quaternary oxide, namely, $AgCuVO_4$ (see Figure 1-2). However, there is only limited information on the optoelectronic behavior, electronic band structures, thermal/electrochemical stability, and electrochemical/photo-

electrochemical attributes of these two semiconductors. Thus, further study, beyond the scope of this dissertation, is required on these aspects for $Ag_2Cu_2O_3$ and $AgCuVO_4$, in the future.

APPENDIX A

SUPPORTING INFORMATION FOR CHAPTER 2

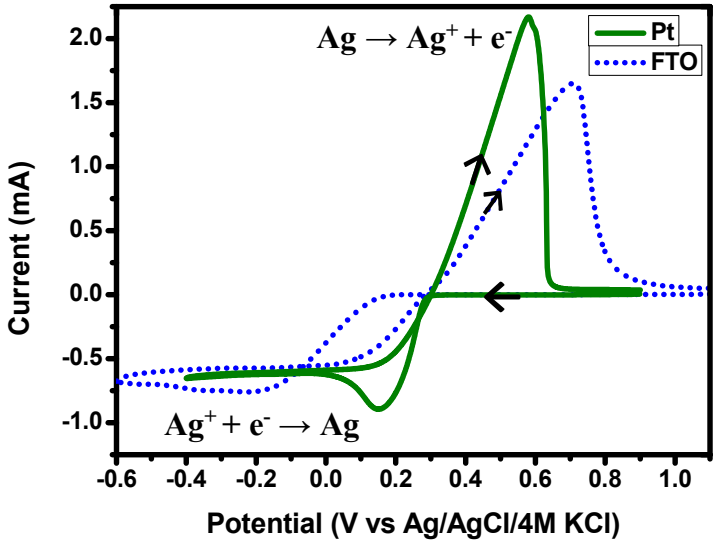

Figure A-S1. Cyclic voltammograms for 20 mM $AgNO_3$, 0.2 mM sodium dodecyl sulfate, and 200 mM tetrabutyl ammonium perchlorate in acetonitrile on Pt (—) and FTO (---) , 25 mV/s scan rate.

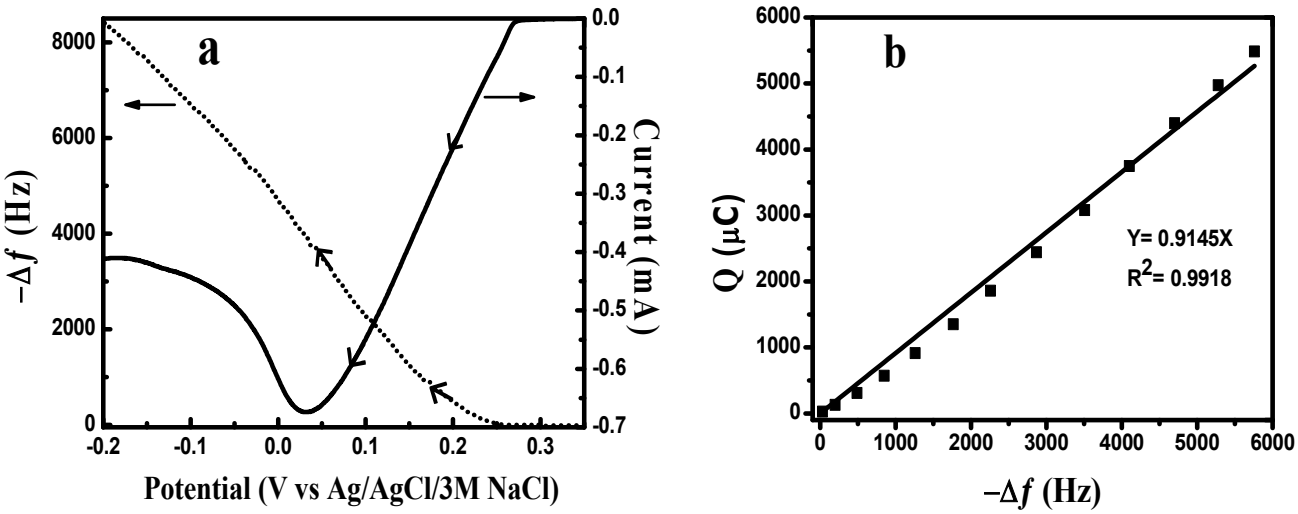

Figure A-S2. (a) Linear sweep voltammogram (—) and the corresponding EQCM frequency change (---) for the electrodeposition of silver on Pt at 25 mV/s potential scan rate. (b) Charge-frequency change plot derived from the EQCM-voltammetry data.

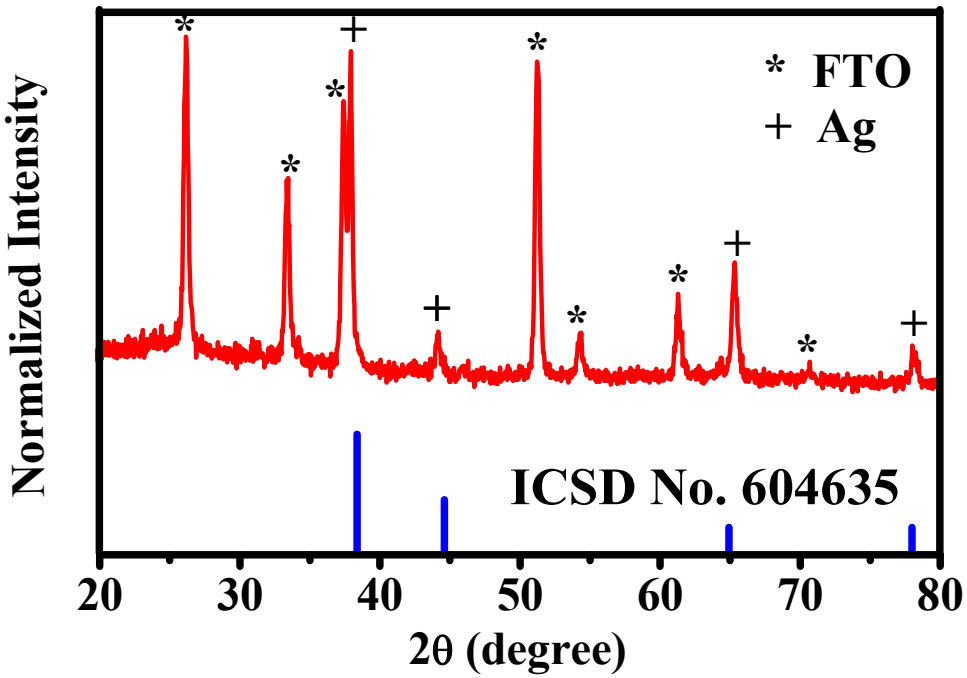

Figure A-S3. XRD patterns for the electrodeposited silver film on FTO.

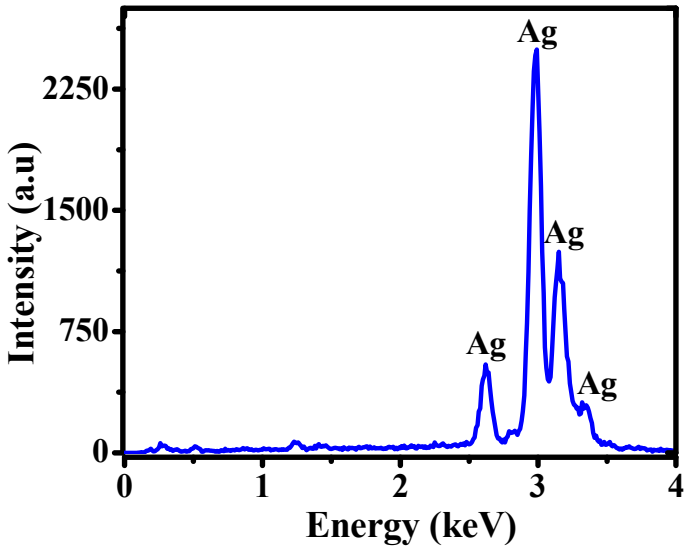

Figure A-S4. EDS scan on the above sample. Note that only the expected signals from Ag are present.

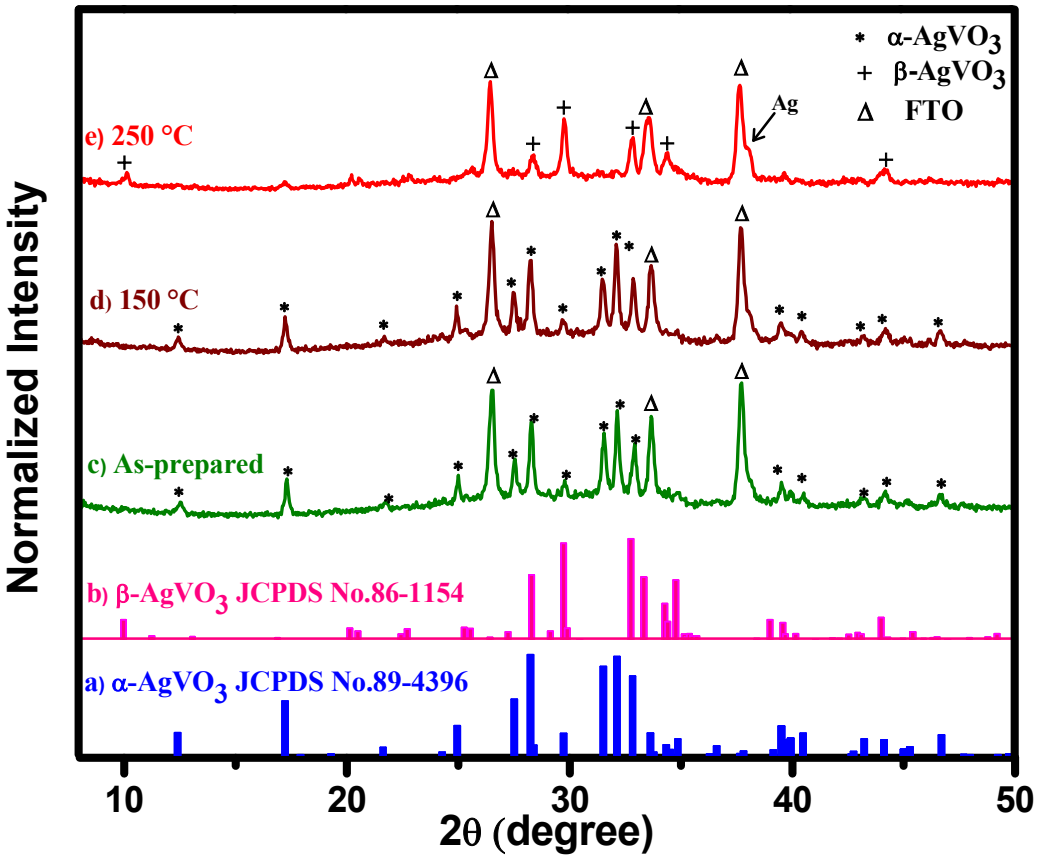

Figure A-S5. XRD patterns for a) α-$AgVO_3$, b) β-$AgVO_3$, c) As-prepared sample, d) Annealed sample at 150 ºC for 30 min, and e) Annealed sample at 250 ºC for 30 min.

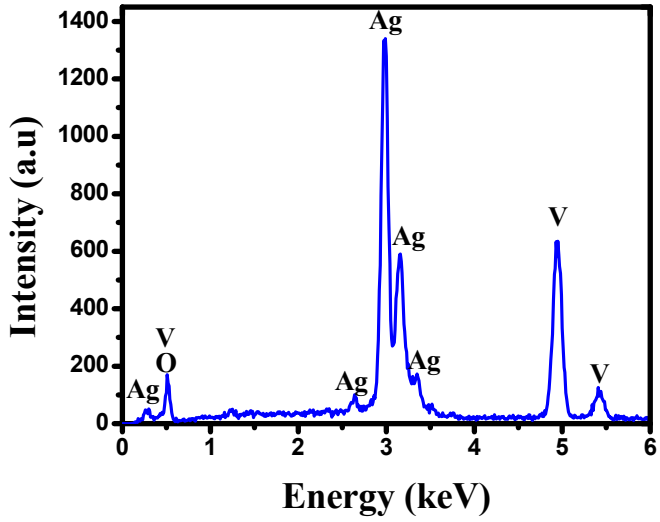

Figure A-S6. An EDS scan for as-prepared sample. The sample only shows the expected elements: Ag, V, and O.

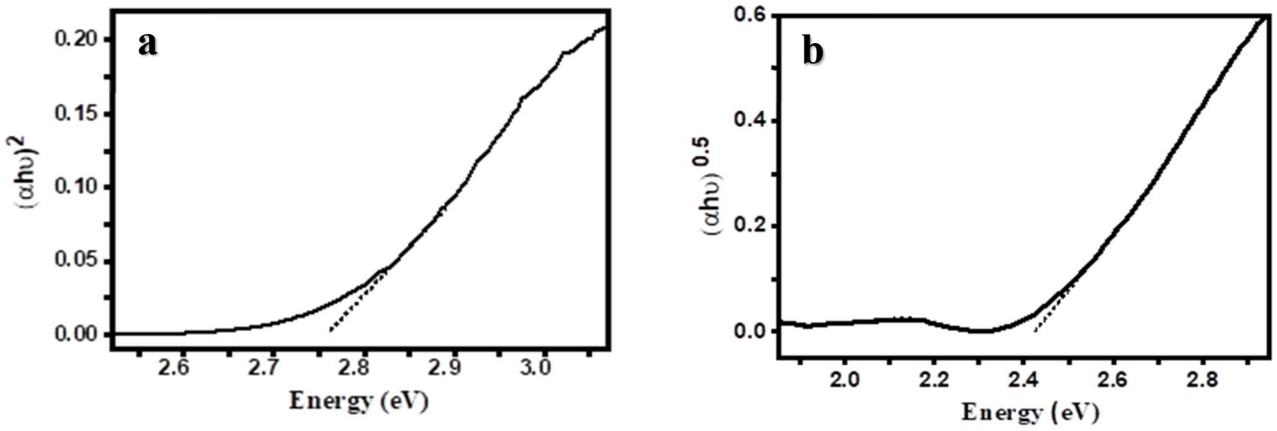

Figure A-S7. Tauc plots for an as-prepared silver vanadate film on FTO. Frames (a) and (b) contain the plots analyzed for direct and indirect optical transitions respectively.

Table A-S1. Unit cell parameters for the two $AgVO_3$ polymorphs obtained from DFT +U energy minimization in this study compared with those derived from other methods and from experimental XRD data.

	α-$AgVO_3$ (monoclinic, space group: *C2/c*)						**β-$AgVO_3$ (monoclinic, space group: *Cm*)**					
Lattice constant	**DFT+U (This study)**	**PBE[a]**	**B3LYP[a]**	**HSE06[a]**	**Exp. [b]**	**Exp. (This study)**	**DFT+U (This study)**	**PBE[a]**	**B3LYP[a]**	**HSE06[a]**	**Exp. [c]**	**Exp. (This study)**
a (Å)	10.80	11.64	11.40	11.56	10.44	10.44	18.58	17.42	17.75	17.47	18.10	18.10
b (Å)	10.50	7.37	8.18	7.27	9.90	9.90	3.61	3.54	3.55	3.54	3.58	3.58
c (Å)	5.93	6.06	5.89	5.97	5.53	5.53	8.18	8.13	8.20	8.11	8.04	8.04
α (^{0})	90.00	90.00	90.00	90.00	90.00	90.00	90.00	90.00	90.00	90.00	90.00	90.00
β (^{0})	110.84	109.43	106.38	108.25	99.69	99.69	104.86	103.48	103.51	103.65	104.44	104.44
γ (^{0})	90.00	90.00	90.00	90.00	90.00	90.00	90.00	90.00	90.00	90.00	90.00	90.00

Exp. stands for experimental data
[a] Reference 15
[b] Reference 36
[c] Reference 37

APPENDIX B

SUPPORTING INFORMATION FOR CHAPTER 3

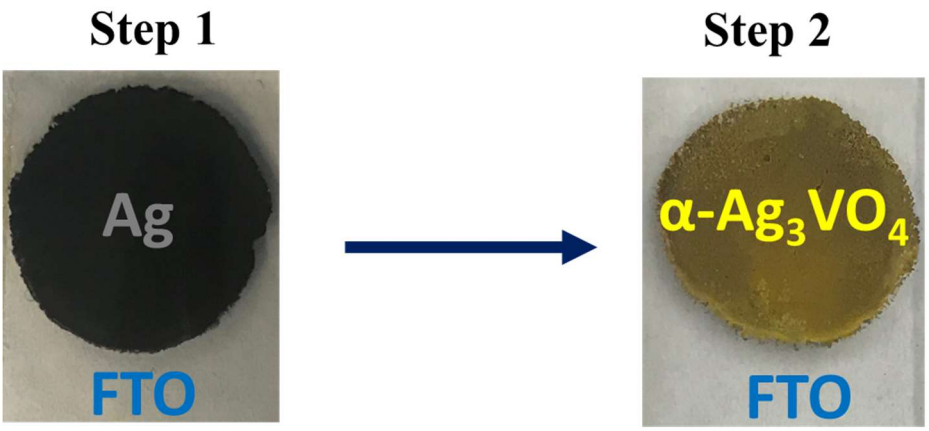

Figure B-S1. Photograph of the color change accompanying the silver → silver orthovanadate conversion in the second step (refer to text).

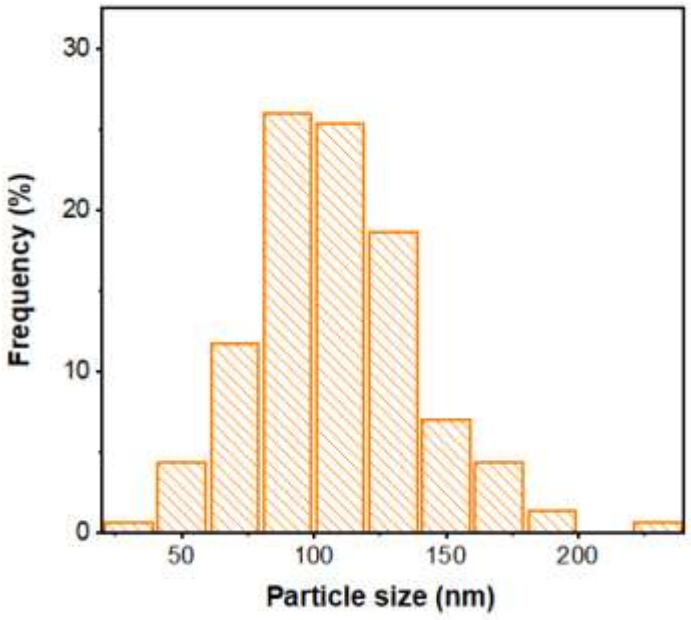

Figure B-S2. Particle size distribution in the Ag_3VO_4 sample considered in Figure 3-2B.

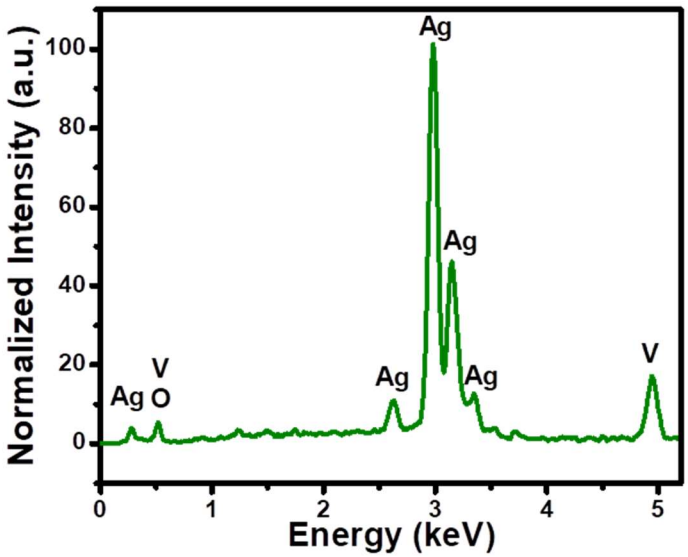

Figure B-S3. An EDX scan for an as-prepared electrodeposited sample. The sample only shows the expected elements: Ag, V, and O.

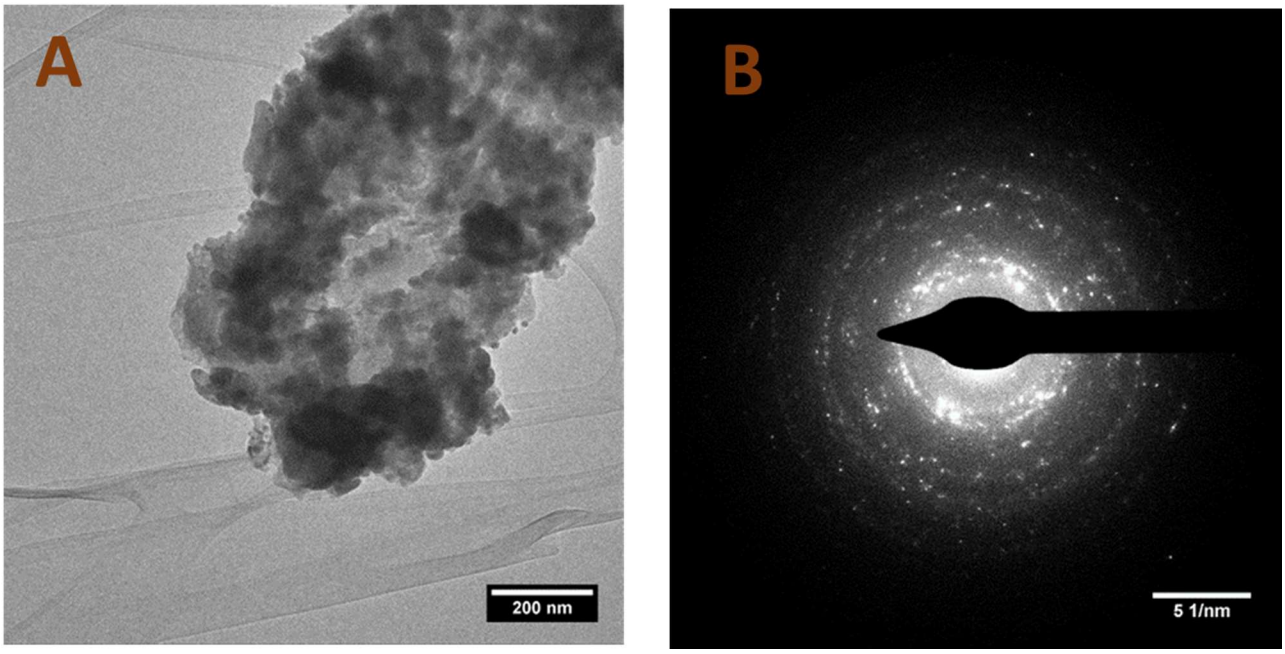

Figure B-S4. Morphological characterization of α-Ag_3VO_4 by TEM (A) and SAED (B).

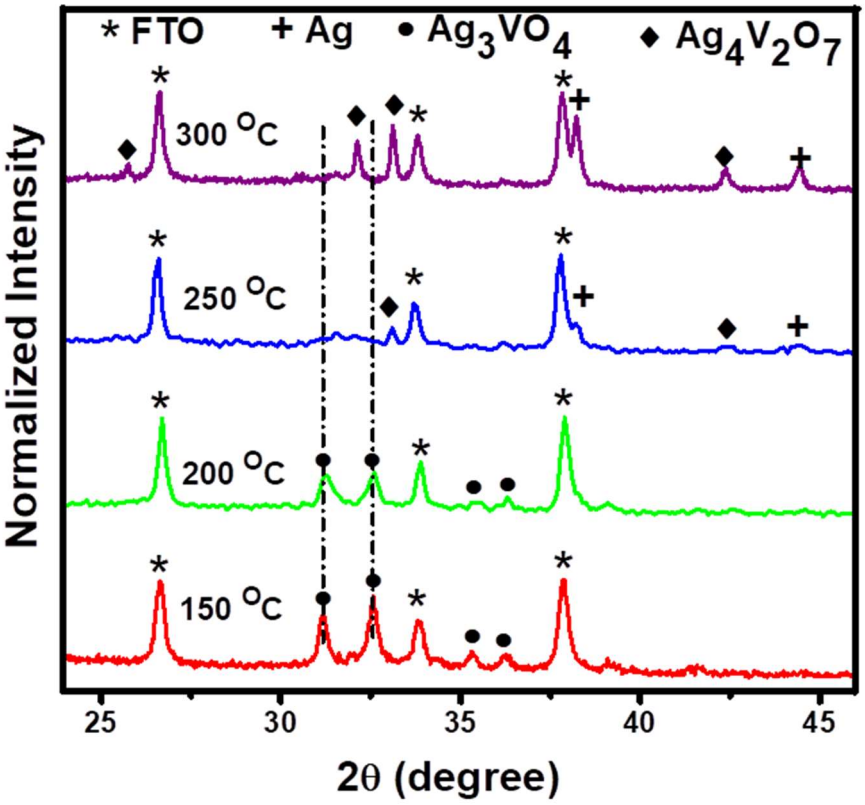

Figure B-S5. XRD patterns of α-Ag_3VO_4 at different temperatures.

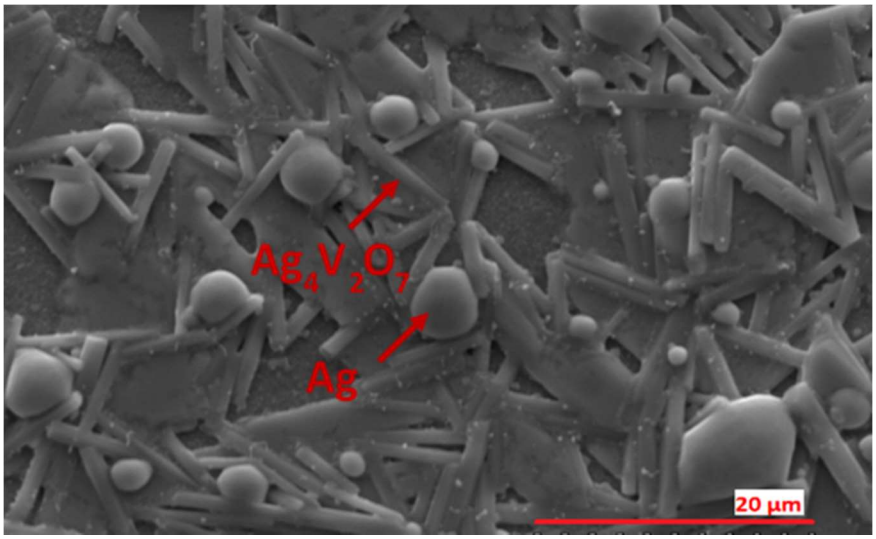

Figure B-S6. Representative scanning electron micrograph of a pre-annealed α-Ag_3VO_4 film at 350 ºC on FTO.

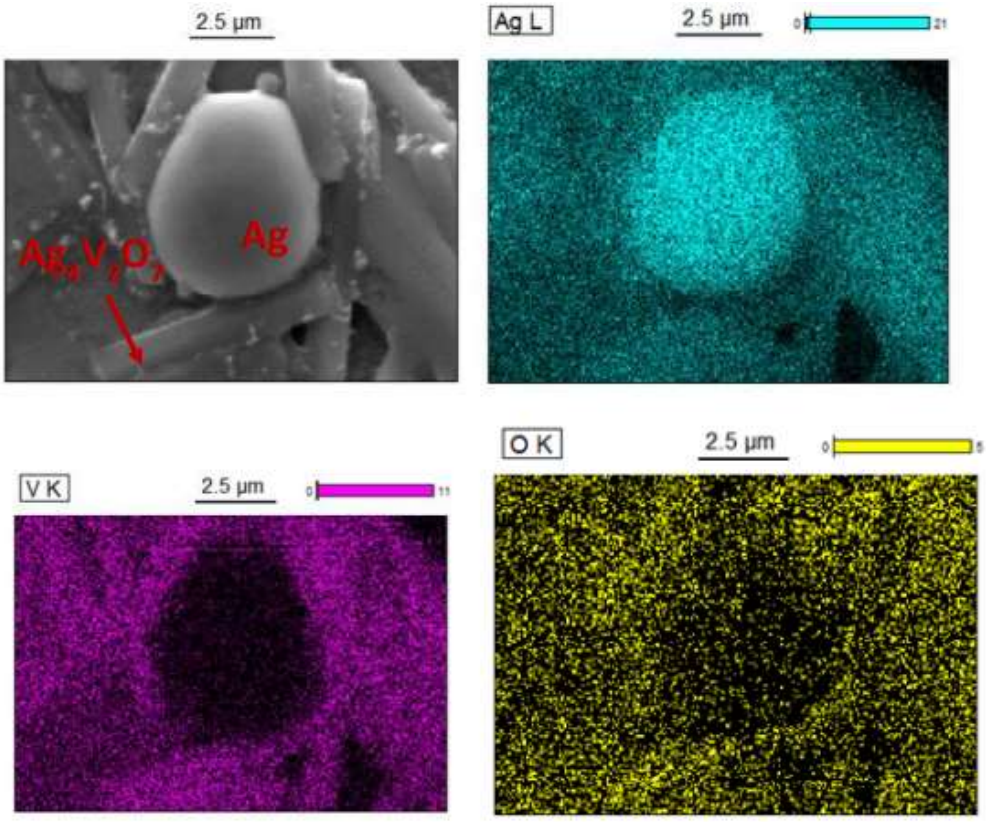

Figure B-S7. Reference scanning electron micrograph and elemental EDX maps for a pre-annealed α-Ag_3VO_4 film at 350 °C on FTO.

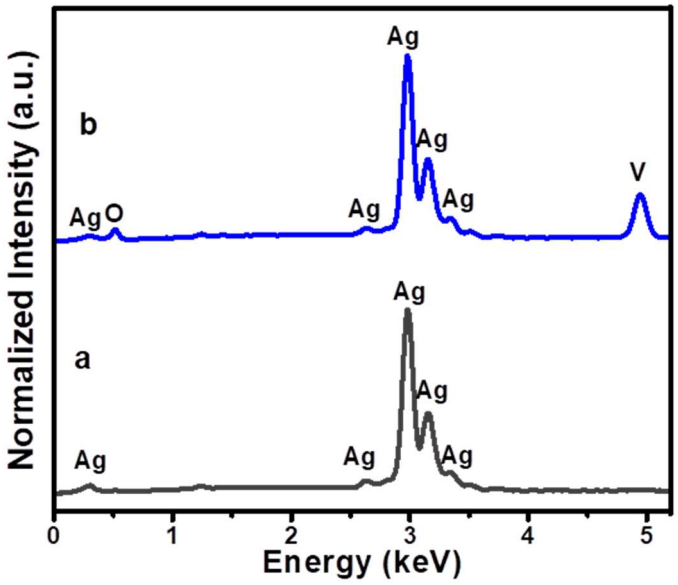

Figure B-S8. EDX scans for pre-annealed silver vanadate film at 350 °C. (a) Ag-rich zone and (b) $Ag_4V_2O_7$-rich zone. The Ag and $Ag_4V_2O_7$-rich zones are shown in Figure B-S6.

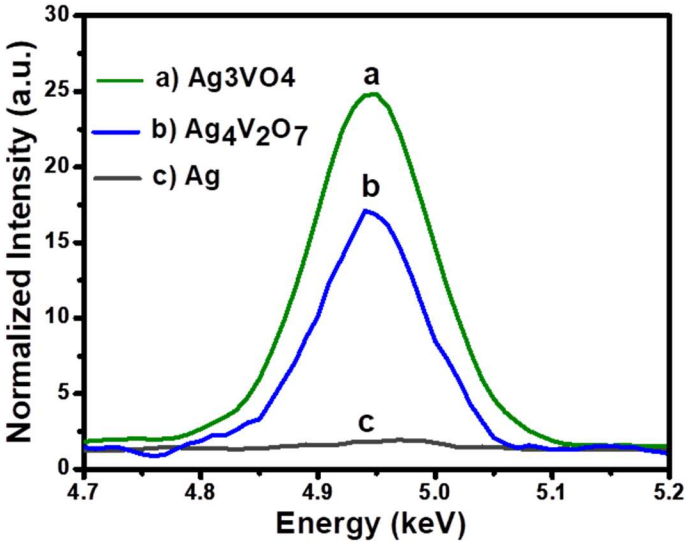

Figure B-S9. EDX scans to find the amount of vanadium in (a) as-prepared Ag_3VO_4, (b) $Ag_4V_2O_7$-rich zone and (c) Ag-rich zone for a pre-annealed silver vanadate film at 350 ºC. The Ag and $Ag_4V_2O_7$-rich zones for the pre-annealed sample are shown in Figure B-S6.

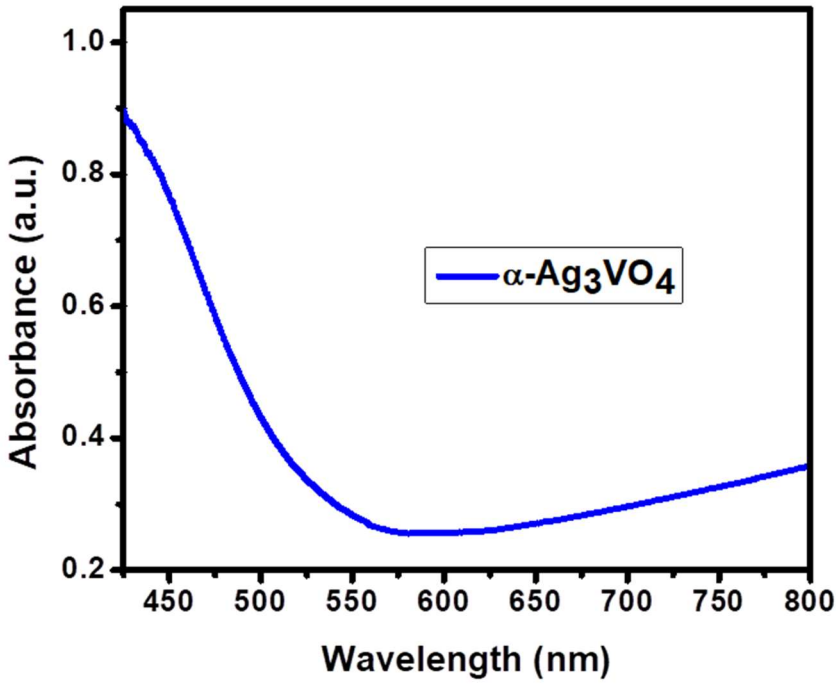

Figure B-S10. UV-visible absorption spectrum for as-prepared α-Ag_3VO_4.

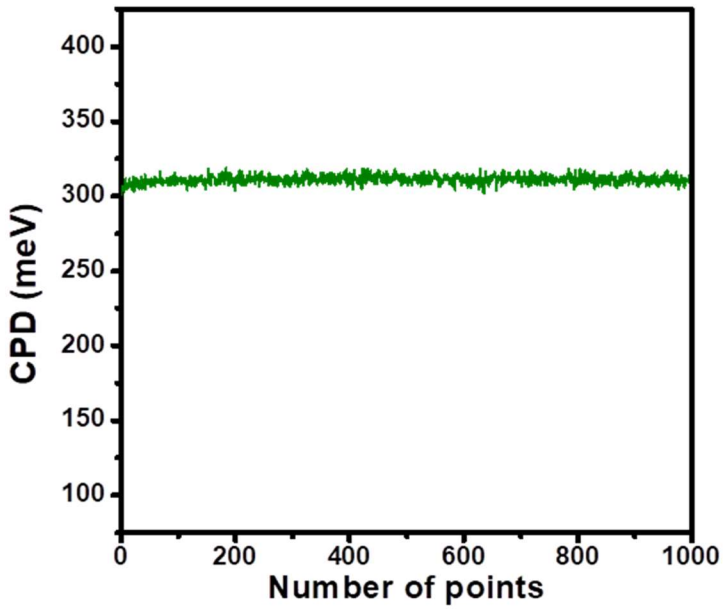

Figure B-S11. Contact potential difference (CPD) for as-prepared α-Ag_3VO_4.

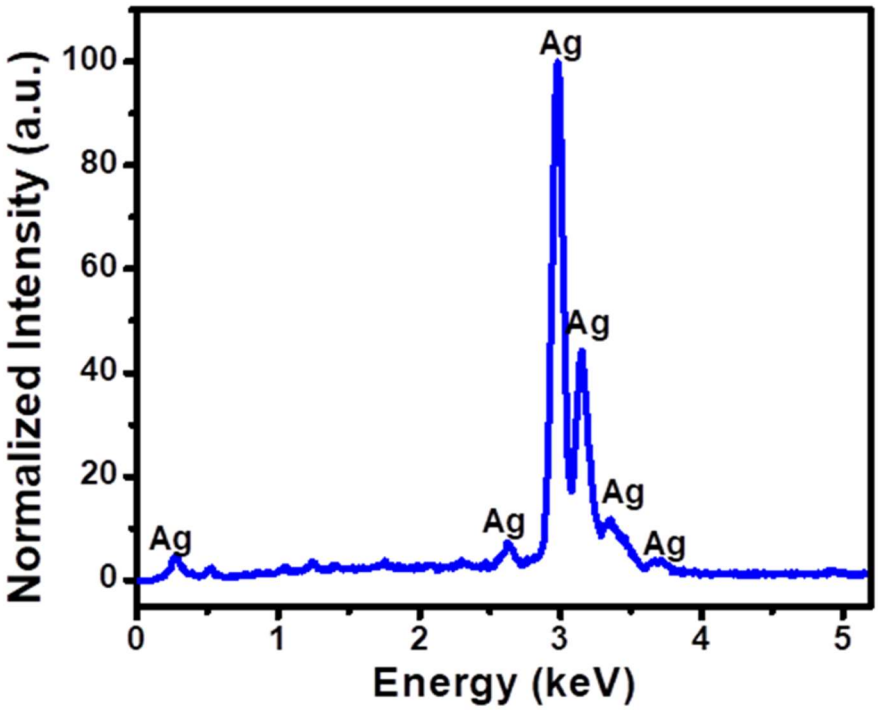

Figure B-S12. An EDX scan for the residual sample after cathodic corrosion of silver vanadate in 0.2 M sodium sulfate.

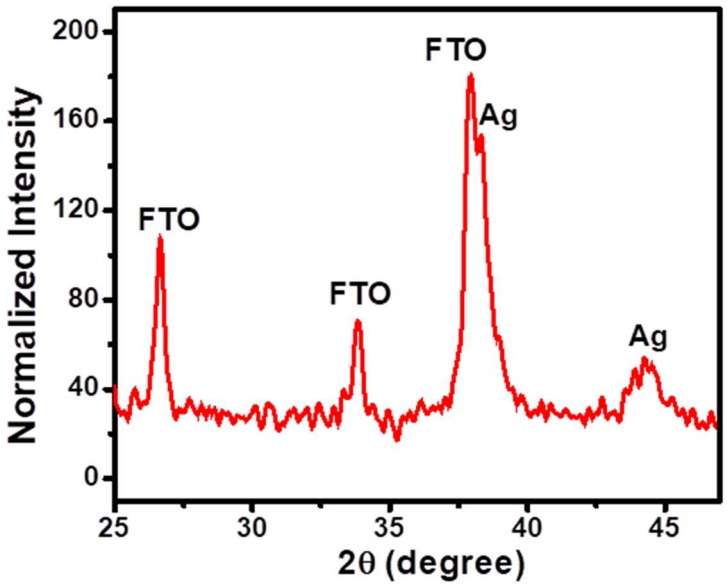

Figure B-S13. XRD pattern for the residual sample after cathodic corrosion of silver vanadate in 0.2 M sodium sulfate.

APPENDIX C

SUPPORTING INFORMATION FOR CHAPTER 4

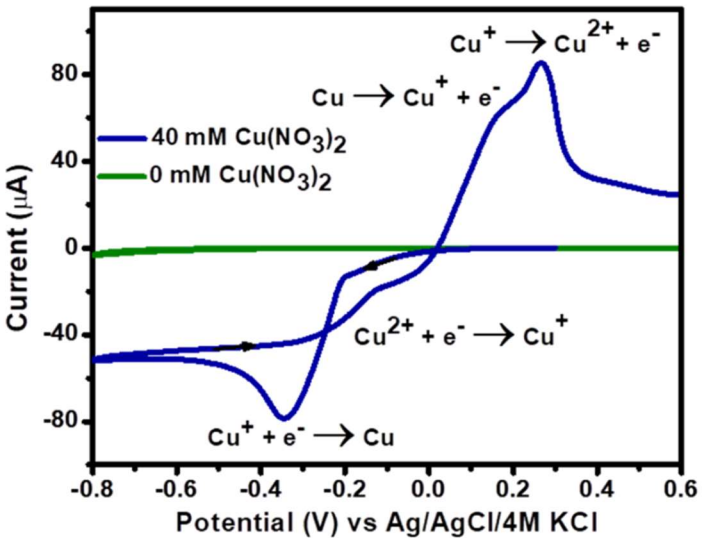

Figure C-S1. Cyclic voltammogram for FTO in 0.1 M KNO_3 and 40 mM $Cu(NO_3)_2 \cdot 2.5H_2O$ in DMSO, 10 mV/s scan rate. Cyclic voltammogram for FTO in 0.1 M KNO_3 in DMSO without $Cu(NO_3)_2 \cdot 2.5H_2O$ is shown as a blank for comparison.

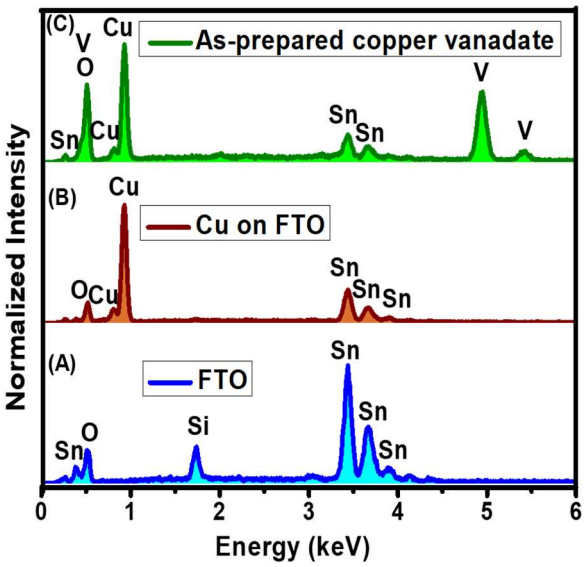

Figure C-S2. EDX scans for (A) FTO substrate (B) electrodeposited copper thin film on FTO and (C) film after the final step in the ETD sequence (c.f., Scheme 1).

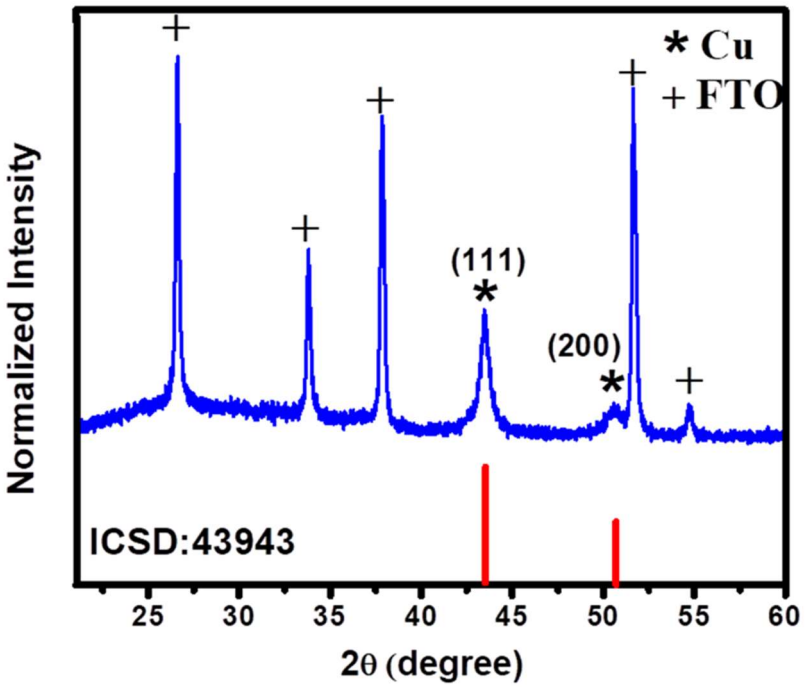

Figure C-S3. X-ray diffractogram for an electrodeposited copper thin film on FTO substrate.

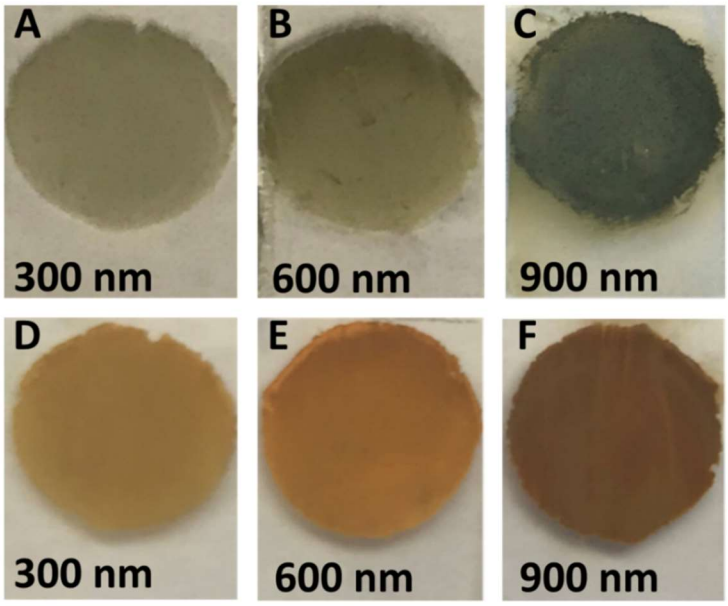

Figure C-S4. Photographs of (A-C) copper vanadate thin films after the second electrosynthesis step and (D-F) samples after the final thermolysis step in air.

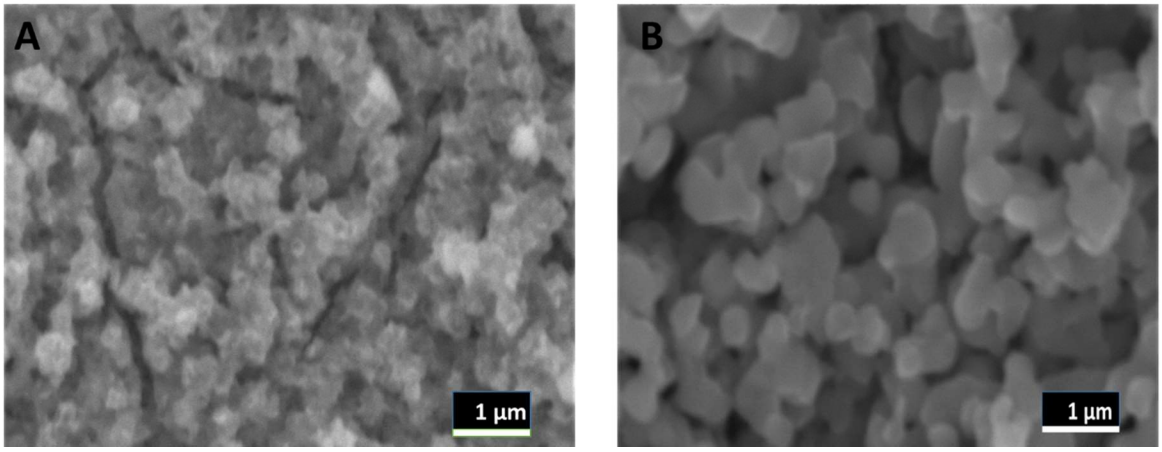

Figure C-S5. Representative scanning electron micrographs of (A) as-prepared copper vanadate and (B) β-$Cu_2V_2O_7$ film on FTO substrate.

Table B-S1. Comparison of photocurrent value at 1.23 V vs RHE for our β-$Cu_2V_2O_7$ sample with literature data. These data were collected in the absence of a hole scavenger.[a]

Synthesis method	Electrolyte and pH[b]	Morphology	Photocurrent ($mA\ cm^{-2}$)	Ref.
Solution combustion	0.1 M borate buffer, pH: 9.2	Irregular nanoparticles	0.065	(3)
Drop casting	0.1 M borate buffer, pH: 9.2	Irregular nanoparticles	0.035	(19)
Electrospraying	0.3 M potassium sulfate + 0.2 M phosphate buffer pH: 6.8	Semispherical nanoparticles	0.041	(15)
Co-sputtering	0.1 M borate buffer, pH: 9.3	Semispherical nanoparticles	0.036	(6)
Electrospraying	0.1 M borate buffer, pH: 9.2	Irregular nanoparticles	0.100	(20)
SILAR[c]	0.1 M borate buffer, pH: 9.0	Irregular nanoparticles	0.070	(21)
Hydrothermal	0.5 M sodium sulfate	Nanoplate	0.410	(16)
Electrodeposition	0.1 M borate buffer, pH: 8.6	Irregular nanoparticles	0.120	This study

[a] In most of the cases, the samples were also subjected to post-synthesis thermal anneal.
[b] The details pertain to the voltammetric measurements.
[c] SILAR = Successive Ionic Layer Adsorption and Reaction.

Table B-S2. Comparison of photocurrent value at 1.00 V vs RHE for our β-$Cu_2V_2O_7$ sample with literature data. These data were collected in the presence of a hole scavenger.[a]

Synthesis method	Electrolyte and pH[b]	Morphology	Photocurrent at 1.00 V vs RHE ($mA\ cm^{-2}$)	Ref.
Solution combustion	0.1 M borate buffer + 0.1 M sodium sulfite, pH: 9.2	Irregular nanoparticles	0.075	(3)
Drop casting	0.1 M borate buffer + 0.1 M sodium sulfite, pH: 9.2	Irregular nanoparticles	0.030	(19)
Co-sputtering	0.1 M borate buffer + 0.1 M sodium sulfite, pH: 9.3	Semispherical nanoparticles	0.030	(6)
SILAR[c]	0.1 M borate buffer + 0.1 M sodium sulfite, pH: 9.0	Irregular nanoparticles	0.050	(21)
Nanocrystal-seeded synthesis	0.1 M borate buffer + 0.1 M sodium sulfite, pH: 8.2	Irregular nanoparticles	0.230	(42)
Electrodeposition	0.1 M borate buffer + 0.1 M sodium formate, pH: 8.6	Irregular nanoparticles	0.400	This study

[a] In most of the cases, the samples were also subjected to post-synthesis thermal anneal.
[b] The details pertain to the voltammetric measurements.
[c] SILAR = Successive Ionic Layer Adsorption and Reaction.

BIOGRAPHICAL INFORMATION

Abbas Vali was born and raised in Iran. He obtained his B.Sc. in chemical engineering from the Isfahan University of Technology (IUT) and then he started to work as a process engineer in sodium chloride and carbon black industries. Then, Abbas obtained his M.Sc. in chemical engineering (nanotechnology) from the Sahand University of Tabriz (SUT). He joined Professor Rajeshwar's research group to receive his Ph.D. in chemistry from the University of Texas at Arlington (UTA). His research project focused on preparation and characterization of silver and copper vanadate semiconductors for solar energy conversion processes.